

Investigations Into Solvate forms of Naloxone using Solid-State NMR and Simulations.

Charles Mitchell-Thurston, MSc

A Thesis submitted to the department of Chemistry of University of Nottingham

For the Degree of Doctor of Philosophy

September 2023

Declaration

I confirm that Charles Mitchell-Thurston did the research detailed in this thesis, that it is the outcome of his own studies at the University of Nottingham, and that it is not being submitted concurrently for another degree.

Supervisor Signature: Jeremy Titman 28/09/2023

A handwritten signature in black ink that reads "Jeremy Titman". The signature is written in a cursive style with a large initial 'J' and 'T'.

Abstract

The aim of this work is to investigate solvate forms of a pharmaceutical compound using solid-state nuclear magnetic resonance (NMR) spectroscopy to be able to differentiate them and provide structural insight, such as the change in orientation of an aliphatic chain. This was done by a combination of two approaches, one using experimental techniques and the other using simulations. Naloxone was chosen as the model compound because of its pharmaceutical importance, as well as the fact that it possesses multiple solvate forms. For all three of the available forms of naloxone, both proton and carbon-13 NMR experiments were employed.

Using a refocused INADEQUATE experiment, and Dynamic Nuclear Polarization (DNP) allowed the carbon-13 NMR spectra of all three to be assigned. This allowed for differentiation between the available solvate forms based on their chemical shift peak positions. Symmetry-based recoupling techniques allowed for the reintroduction of the proton chemical shift anisotropy (CSA). This allowed for structural differences between the forms to be observed in experimental data. NMR analysis showed clear degradation, detected using carbon-13 analysis, of one of the samples from a purely anhydrous form to a mixed hydration form.

Comparison of experimental data with density functional theory (DFT) calculations of NMR parameters allowed for confirmation of carbon assignments as well as further insight into structural information such as the change in orientation of naloxone's aliphatic tail. Experimental data was simulated using SIMPSON and by making use of code that broadened the 1D simulations along the isotropic axis to generate 2D simulations, this allowed for the direct comparison of experimental to simulated spectra. The code, which was written in MATLAB, functions via normal distribution broadening, while also automating SIMPSON

simulations. Once 1D simulations are inserted at their isotropic values they are broadened along this axis for every anisotropic axis point.

This thesis shows the effectiveness of both DNP and recoupling techniques for analysis of diverse solvate forms of a compound. It also presents a novel way to make use of CASTEP data to produce 2D simulations of CSA recoupling experiments. These findings illustrate key structural differences between the forms and suggest similar differences could be seen in other pharmaceutical compounds.

Acknowledgements

Firstly, I would like to express my deepest gratitude to my supervisor Dr Jeremy Titman for the amazing opportunity. The last four years of thoughtful guidance have made them so impactful and memorable. Thank you for all the help, being patient with me and giving me this opportunity. I would also like to thank Dr Huw Williams who in the last 6 months has become a secondary supervisor and whose proactive nature and setting deadlines has been of tremendous importance helping me address my own shortcomings in that area. Without Jeremy and Huw, I cannot imagine myself completing a PhD.

My thanks to the University of Nottingham and the staff at the School of Chemistry in particular. I am grateful to GSK for their sponsorship and particularly in appointing Dr Tran Pham as my industry supervisor. He has been generous in sharing his knowledge and experience and his friendly encouragement has been very kind when not in meetings. I am grateful to the UKRI government body for the EPSRC ICASE studentship and the opportunity it provided.

I would also like to thank the UK High-field Solid-state NMR facility for allowing me to visit and make use of their facilities as well as Dr Trent Franks for the assistance during, Dr Subhradip Paul and Dr Paolo Cerreia Vioglio for assistance with using the DNP at the university of Nottingham, Dr Alison McLellan and Dr Marco Mais from Jeremy's research group for again helping answer my many questions, Matt Millward for sitting down with me and assisting me with the math behind the creation of the simulation code, Tristan Lawrie for helping me begin to understand Quantum Mechanics.

A huge thank you to my parents Vanessa and Dominic Green for helping me through 8 years of university, I could not have done it without you both. Thank you to all of my friends for their support. And Sarah Soo, thank you for all your support and helping answer my plethora of coding questions.

Contents

Declaration.....	i
Abstract.....	ii
Acknowledgements.....	iv
Contents.....	v
List of figures.....	x
Chapter 1: Introduction	1
1.1 Brief History of NMR	2
1.2 Modern solid-state NMR.....	3
1.3 Polymorphism and Solvates in Pharmaceutical compounds.....	4
1.4 Objectives.....	6
Chapter 2: Theory	7
2.1 Time Independent Schrödinger Equation	7
2.2 Zeeman interaction	8
2.3 Spin operators.....	9
2.4 Coherence	11
2.5 Internal and external Hamiltonian	11
2.6 Chemical Shift Interaction	12
2.7 Principal axis frame, Asymmetry and Anisotropy	14
2.8 Dipolar Coupling.....	15

2.9 J-coupling.....	16
2.10 Quadrupolar interaction.	17
2.11 Density operator	18
2.12 FIDs and pulse programs.....	22
2.13 Relaxation.....	24
2.14 Signal Sampling	25
Chapter 3: DNP theory.....	27
3.1 Instrumentation	27
3.2 Radicals and solvent.....	28
3.3 Mechanism and enhancement.....	30
3.4 Cross effect.....	31
3.5 Spin diffusion.....	33
3.6 Cross polarization.....	36
3.7 Evaluating the effect of DNP	36
Chapter 4: CSA Recoupling	40
4.1 Symmetry based recoupling principles.....	40
4.2 R and C sequences.....	42
4.3 Selection rules	43
Chapter 5: Experimental	47
5.1 DNP experiments.....	48

5.1.1 Naloxone HCl di-hydrate RI	49
5.1.2 Naloxone Freebase Monohydrate RI.....	50
5.1.3 Naloxone Freebase Anhydrous RI	50
5.1.4 Naloxone CP experiments	51
5.2 CSA based recoupling experiments.....	52
5.2.1 800 MHz Recoupling Experiments.....	52
5.2.2 1 GHz Recoupling Experiments.....	53
5.2.3 1 GHz BABA and NOESY	53
5.3 Solution NMR experiment.....	54
Chapter 6: Naloxone	55
6.1 13-Carbon analysis.	57
6.2 Solvate identity.....	69
6.3 Differentiating via hydrogen	78
6.4 Mixed hydration level affects.....	90
6.5 Conclusions.....	95
Chapter 7: Calculations	97
7.1 Geometry optimisation and Convergence	98
7.2 13-C Calculations	100
7.3 Proton calculation and simulation	102
7.4 Simulations vs experimental data	107

7.5 Conclusion	111
Chapter 8: Pantheon	113
8.1 Initial Settings for Pantheon.....	114
8.2 Simulating the spectra	117
8.3 2D Weighting.....	118
8.3.1 'ND' vs 'Gauss'	118
8.3.2 Mirrored FID	122
8.4 Post Simulation processing	125
8.4.1 Artifact Removal	125
8.4.2 DC Correction.....	126
8.5 Easy Pantheon	128
8.6 Future additions to the code.....	130
8.6.1 Expanding Pantheon.....	130
8.6.2 Obtaining CSA values from experimental data.	131
Chapter 9: Summary	134
References	137
Appendix	150
Appendix 1 – Pantheon Code.....	150
Appendix 2 – Example .in file	166
Appendix 3 – Example .cell file (naloxone HCl).....	167

Appendix 4. Refocused INADEQUATE pulse program.	172
Appendix 5 SC212 Pulse Program	177
Appendix 6 – Calculated vs experimental table.....	182
Appendix 7 – BABA pulse program	183
Appendix 8 – NOESY pulse program	187

List of figures

Figure 2-1 , the variations caused by asymmetry (η) on the CSA pattern when δ_{iso} and ζ are constant.	15
Figure 3-1, the structures of the bi-radicals TEKPol and AMUPol.	30
Figure 3-2, the energy level diagrams involved in the cross effect.	32
Figure 3-3, Spin diffusion diagram.	34
Figure 3-4, the chemical structure of Casopitant mesylate.	37
Figure 3-5, ^{13}C CP-MAS-MAS NMR spectra for Casopitant mesylate.	38
Figure 3-6, the chemical structure of Allopurinol.	38
Figure 3-7, ^{13}C CP-MAS-MAS NMR spectra for Allopurinol.	39
Figure 4-1, a representation of the symmetry numbers of the $C221$ sequence.	43
Figure 4-2, $SC221$ Spin-space selection diagram.	44
Figure 4-3, $R1623$ sequence spin-space selection diagram.	45
Figure 5-1 Graphical representation of the Refocused INADEQUATE pulse program.	49
Figure 5-2 Pulse program for the SC212 experiment.	52
Figure 6-1, Chemical structure of naloxone with carbon positions numbered.	56
Figure 6-2, The crystal structures of naloxone solvates.	57
Figure 6-3. The DNP-enhanced ^{13}C CP-MAS-MAS NMR spectra for the three naloxone forms that were available.	58
Figure 6-4, the pulse sequence and coherence transfer pathway of the refocused INADEQUATE experiment.	60
Figure 6-5, A DNP-enhanced ^{13}C ^{13}C refocused-INADEQUATE spectrum for naloxone HCl dihydrate.	61

Figure 6-6, 1D carbon cross section of naloxone HCl di-hydrate.	62
Figure 6-7, DNP enhanced 1D carbon CP of naloxone HCl di-hydrate.	63
Figure 6-8, A DNP-enhanced ^{13}C ^{13}C refocused-INADEQUATE spectrum for naloxone freebase monohydrate.	65
Figure 6-9, DNP enhanced 1D carbon CP of naloxone freebase monohydrate.	66
Figure 6-10 A DNP-enhanced ^{13}C ^{13}C refocused-INADEQUATE spectrum for naloxone freebase anhydrous.	67
Figure 6-11, DNP enhanced 1D carbon CP of naloxone freebase anhydrous.	68
Figure 6-12, 1D carbon CP of naloxone freebase monohydrate.	70
Figure 6-13, 1D carbon CP of naloxone freebase monohydrate.	72
Figure 6-14, 1D carbon CP of naloxone freebase anhydrous.	73
Figure 6-15, 1D proton of naloxone freebase anhydrous in DMSO.	74
Figure 6-16, 1D carbon CP of naloxone freebase anhydrous DNP prep vs powder.	75
Figure 6-17, 1D carbon CP of naloxone: freebase monohydrate vs freebase anhydrous.	76
Figure 6-18, 1D carbon CP of naloxone: freebase monohydrate as the neat powder and freebase anhydrous in 30 ul of 20 mM AMUPol.	77
Figure 6-19, the 1D proton NMR spectra of the three naloxone forms that were available. .	79
Figure 6-20, the 1D hydrogen spectra of the three naloxone forms, recorded at 100 kHz on 1 GHz magnet.	80
Figure 6-21, the pulse sequence design for <i>R1632</i>	81
Figure 6-22, ^1H MAS NMR isotropic-anisotropic correlation spectra, <i>R1632</i> , of naloxone forms.	81
Figure 6-23, Structural insights of naloxone Freebase monohydrate and HCl di-hydrate.	83
Figure 6-24, the pulse sequence design for <i>SC221</i>	85

Figure 6-25, ^1H MAS NMR isotropic-anisotropic correlation spectra, <i>SC221</i> , of naloxone forms.	85
Figure 6-26, Extracted cross sections from the ^1H MAS NMR isotropic-anisotropic correlation spectra shown in Figure 6-25.....	87
Figure 6-27, ^1H MAS NMR isotropic-anisotropic correlation spectra, <i>SC221</i> , of naloxone forms	88
Figure 6-28, The nutation curve of naloxone HCl di-hydrate on proton.....	89
Figure 6-29, A ^1H ^1H BABA spectrum for naloxone freebase anhydrous performed at 50 kHz on a 1 GHz magnet.....	91
Figure 6-30, A ^1H ^1H NOESY spectrum for naloxone freebase anhydrous performed at 50 kHz on a 1 GHz magnet.....	93
Figure 7-1, geometry optimisation for the three naloxone forms..	99
Figure 7-2, Graphical representation of the difference between experimental data and calculated values.....	101
Figure 7-3, naloxone Freebase Anhydrous <i>R1632</i> cross section at 9.6 ppm (red) overlaid with the CASTEP predicted values for the same proton (black).....	103
Figure 7-4, A diagram of the processes of turning 1D spectra in a 2D spectrum.....	105
Figure 7-5, the graphs linking simulated peak widths to experimental ones	106
Figure 7-6, Comparison of experimental (red) to simulated (black) of ^1H MAS NMR isotropic-anisotropic correlation spectra, <i>R1632</i> , of naloxone	107
Figure 7-7, Comparison of experimental (red) to simulated (black) of ^1H MAS NMR isotropic-anisotropic correlation spectra, <i>SC221</i> , of naloxone.....	109
Figure 8-1 The base workflow for the Pantheon code.	114

Figure 8-2, a MATLAB generated surf plot of three example protons at 0, 2.5 and 5 ppm showing the 'Gauss' approach to 2D and the baseline error.	119
Figure 8-3, a MATLAB generated surf plot of three example protons at 0, 2.5 and 5 ppm showing the 'ND' approaching to 2D.....	120
Figure 8-4. Visual representation of how the simulation broadening is built up.....	122
Figure 8-5, An overlay of all 96 mirrored FID's a) prior to weighting b) post weighting, of a simulation of naloxone freebase anhydrous data.	124
Figure 8-6, a cross section at 12 ppm of ^1H MAS NMR isotropic-anisotropic correlation spectra, SC221, of l-tyrosine HCl. MAS rate of 36 kHz. a) un-altered cross section b) cross section with artifact removal on and correctly set.	126
Figure 8-7, R1623 simulation of a single proton using ζ of 25 and η of 0.1, 800 MHz, 50 kHz spinning speed. The value of DC correction is varied while all other parameters are kept fixed.	127
Figure 8-8, the flow chart of options for 'Easy Pantheon'	129

Chapter 1: Introduction

Nuclear magnetic resonance (NMR) spectroscopy is one of the most commonly used analytical techniques. NMR is used to study everything from proteins to pharmaceutical products to materials. Commonly used for both solution- and solid-state samples, it is one of the most versatile techniques. NMR spectra obtained in solid-state and solution analysis can often be compared, depending on the experiment performed and are a measure of frequency vs. intensity. The versatility of NMR comes from its range of applications, including: the ability to perform structural analysis of a sample, perform analysis on a wide range of nuclei, investigate the dynamics and kinetics of a species, such as the folding of a protein, and the ability to generate detailed images of tissues and organs[1–3].

NMR makes use of strong magnetic fields, aligning the macroscopic spin magnetisation either parallel or anti-parallel to them. These two different orientations are separated by ΔE , the difference in energy levels, the size of which depends on the strength of the interaction between the nuclear magnetic field moment and the external magnetic field, the Zeeman interaction. What is observed in NMR is a transition between nuclear spin energy levels, and because of the small size of ΔE , these are induced and viewed via radiofrequency (rf) pulses [4]. Outside of an external magnetic field, the energy levels are degenerate. At room temperature the Boltzmann distribution suggests that there will be a slight majority of nuclei in the lower energy level, so long as the magnetogyric ratio, γ , the ratio between the angular momentum of a nucleus and its magnetic momentum which is given in units of radians per second per Tesla ($\text{rad}\cdot\text{s}^{-1}\cdot\text{T}^{-1}$), is positive. There is only a slight excess of spins in the lower energy levels which leads to NMR having low sensitivity. The rate of nuclear spin is dictated by $\omega_0 = \gamma B_0$. The Larmor frequency, ω_0 , is the frequency of precession in radians per

second and is dictated by B_0 and γ . The magnetogyric ratio is unique for each element as it depends on the values of charge and mass.

Transitions between these energy levels is induced via short rf pulses. These have sufficient energy to be able to be able to cause a transition, provided the resonance condition is met. This is that $\Delta E = h\nu$, where the difference in the two energy levels is equal to the frequency (ν) of the rf pulse multiplied by Planck's constant [4]. Importantly ΔE is influenced by the environment surrounding the nuclei. This means that a simple molecule such as ethanol, $\text{CH}_3\text{CH}_2\text{OH}$, would have three different proton peaks corresponding to the different hydrogen sites. Where these peaks are located on an NMR spectrum is dictated by their chemical shift, i.e., their environment. The same is true for the difference in the energy levels of the electrons of a radical, a key feature used in Dynamic Nuclear Polarization (DNP) as discussed later.

Spin was alluded to earlier, with nuclear spin energy levels, and has no classical equivalent, though it behaves like angular momentum. An isotope will be NMR active if it has a spin greater than 0. The value of spin is related to the number of protons and neutrons. If both are odd, then the spin will have an integer value, if one is odd and the other is even then the spin will have a half integer value, half integer spins, such as in ^{17}O having a spin of $5/2$, are less commonly investigated due to the lower sensitivity and broader signals due to quadrupolar interactions which are present when $I > 1/2$. Finally, if both the numbers of protons and neutrons are even then the spin will be 0, and so the isotope will be NMR inactive [5].

1.1 Brief History of NMR

In the 1920's the concepts of magnetic moments and nuclear spin had been established[6] Despite this it was not until 1939 that Rabi *et al.* published a paper showing that a beam of

hydrogen atoms passing through a strong, inhomogeneous magnet would be deflected slightly by the energy from rf waves when they were subjected to them at a very precise frequency [7]. This, while not too similar to the modern implementation, was the first observed instance of NMR, and led to Rabi receiving the Nobel prize in 1944. In 1946 two groups, Bloch, Hansen and Packard [8] along with Purcell, Torrey and Pound [9], a few weeks apart both published papers which gave the first NMR signals detected in a more conventional fashion. Both groups would go on to receive Nobel prizes, with Bloch and Purcell receiving theirs together in 1952. These signals were obtained by continuously sending rf waves at a sample across a large range of frequency to be able to observe all signals. This took time and was eventually replaced by modern pulsed NMR in 1950 by Erwin Hahn. Another key development came in 1966 by Ernst and Anderson and involved implementing computer assisted Fourier transforms, shortening experimental times considerably [6].

Up until this point NMR was either done on solutions or static solids with the thought being that high resolution NMR was only going to be possible in solution. In 1958 and 1959 this changed when Andrew *et al.* and Lowe decided to replicate the rapid molecular tumbling seen in solution molecules in solids [10,11]. Theoretical investigations led to the magic angle, 54.74° , leading to Magic Angle Spinning (MAS), this allowed for high resolution solid-state NMR and paved the way for the modern-day technique.

1.2 Modern solid-state NMR.

Modern solid-state NMR has progressed rapidly from its rudimentary beginnings. Where MAS speeds were originally around 7.7 kHz and employed the use of 400 MHz, 9.4 T, magnets, NMR instruments now boast magnets up to 1.2 GHz, 28.2 T with commercially available MAS probes capable of spinning at 100 kHz and faster [12–15]. An important thing to note is the

way that an NMR magnets strength is described, the MHz value is the frequency of proton in that magnet. While samples can be spun faster than ever, there is seemingly a limit to how fast. Limiting factors include the speed of sound and how the stiffness of the rotor is affected by changing temperatures. While the speed of sound problem can be somewhat circumvented by making the rotors progressively smaller, this also limits the sample volume, making low abundance isotope analysis more challenging. A 0.6 mm rotor, capable of spinning up to 136 kHz has a sample volume of only 0.4 μ l [16].

1.3 Polymorphism and Solvates in Pharmaceutical compounds.

A polymorphic compound is one that has crystallised in distinct structural arrangements. In pharmaceutical sciences it is paramount that what is theoretically synthesised matches up to reality for any synthesis involving crystallisation. This is important for a multitude of reasons including: differing solubilities of polymorphs, patent regulations and regulatory compliance. Polymorphism is a key issue in pharmaceuticals as polymorphs can be produced due to minute changes in the manufacturing of compounds [17]. This means that a single chemical has multiple possible crystal structures. Concomitant polymorphism, the simultaneous crystallization of multiple polymorphs, is a problem for the pharmaceutical industry as each can have different dissolution rates and chemical stability among other varying factors which, in turn, affect drug delivery and dosage. Properties such as solubility and bioavailability vary between polymorphs [18]. Solvates pose similar considerations to polymorphs, these are chemical compounds with varying water content, or other solvents, and possible other additions, such as salts. These can come about deliberately or as part of the synthesis and can affect the crystal packing.

Because of the different properties it is crucial to identify which polymorphs and solvates are present during preparation stages and in the final product is important. Polymorphs and solvates can be synthesised in isolation using various techniques such as specific crystallization [19]. An example of the differences between polymorphs is found in oxytetracycline where polymorph A had a 55% dissolution at 30 mins, whereas polymorph B had 95 [20].

Polymorphs can be analysed into multiple ways, but the predominant way is via X-ray Diffraction analysis (XRD). This is the process of using monochromatic X-rays to assess a crystalline structure via measuring the distances between atoms. This process can be used to obtain the crystal structure of the sample. This information is what is used later in this work, and this is what CASTEP uses to make calculations from. This crystal structure can often show whether there is a single form or multiple in a unit cell. This can be used to assess differences between known polymorphs or to see if a mixture is present.

In addition to XRD, thermal techniques like Differential Scanning Calorimetry (DSC) and Thermogravimetric Analysis (TGA) are employed. DSC measures the energy required to change the temperature of a sample, revealing thermal differences between polymorphs. TGA, on the other hand, monitors how the weight of a sample changes with temperature. Both techniques offer valuable insights into polymorphic transitions. As this work focuses on solvates a pertinent example of the uses thermal techniques could be to view the change in mass of a sample as the hydration state changes due to heating [21,22].

XRD as well as thermal techniques can provide a wellspring of information pertaining to polymorphs or solvates. XRD often goes hand in hand with ssNMR as one can be used to help

explain observable phenomena in the other.

1.4 Objectives

This work focuses on two main aspects, these parts dictate the structure of the thesis with the first area focusing on chapters 6 and 7, with the second aspect being found in chapter 7 and 8. The first is utilizing a variety of techniques to differentiate different solvates of a compound. The objective can be further divided into two parts. The first part involves demonstrating the application of DNP in pharmaceutical analysis. This is to help illustrate the use of DNP in the pharmaceutical industry by showing that it can allow for the normally unfeasible experimental times of a refocused INADEQUATE to be drastically shortened via the implementation of DNP.

The second part is implementing symmetry-based recoupling techniques to showcase their utility in identifying various solvates and determining their structural characteristics. These techniques can show links between XRD and NMR data in regards to changing hydrogen bond networks.

The second key area is the linking of simulated NMR spectra with experimental ones. To demonstrate this, it is shown how CASTEP and SIMPSON can be used in conjunction to aid in NMR analysis. This will illustrate the usefulness of the novel script documented in this work and help illustrate its usefulness in aiding in NMR analysis.

Chapter 2: Theory

The understanding of NMR involves the basic understanding of quantum mechanics. Spin is classically introduced as a vector. Spin is a fundamental degree of freedom that every particle has and comes from the elementary particles where all, bar the Higgs boson, have a spin value over zero [23]. This chapter focuses on the quantum mechanics and the acquisition side including relaxation, signal sampling and Pulse programs.

2.1 Time Independent Schrödinger Equation

The Schrödinger equation is crucial for understanding the underlying quantum effects of a nuclei. when in a magnetic field. It allows for information about energy levels and the transitions between them to be calculated. The time-independent Schrödinger equation is expressed as,

$$\hat{H}|\psi_n\rangle = E_n|\psi_n\rangle \quad (2.1)$$

where $E_n = \hbar\omega_n$ is the energy of the n th state of the system, ψ is the wave function, \hbar is Planck's constant over 2π and ω_n is the corresponding angular frequency. Here \hat{H} is the total Hamiltonian of the system that describes the nuclear spin state.

The state of a system can be described by a complex vector wave function $|\psi\rangle$ as expressed with a "ket" in Dirac notation. While its conjugate transpose $|\psi\rangle^\dagger \equiv \langle\psi|$ is expressed with a "bra".

Wave functions are considered both normalised and orthogonal (orthonormal) if the following condition is satisfied,

$$\langle \psi_a | \psi_b \rangle = \delta_{ab} \equiv \begin{cases} 1, & a = b \\ 0, & a \neq b \end{cases} \quad (2.2)$$

Where the subscript a and b simply refer to different states. This is to say that if the two states are the same, then the inner product is equal to 1, otherwise the product is zero.

Observables are represented by an operator \hat{A} . Where the observable expectation value is given by,

$$\langle \hat{A} \rangle \equiv \langle \psi | \hat{A} | \psi \rangle \quad (2.3)$$

This is to say that measuring the observable \hat{A} in the quantum system represented by $|\psi\rangle$ will give the average value of $\langle \hat{A} \rangle$.

2.2 Zeeman interaction

As mentioned, when an atomic nucleus is placed into an external magnetic field the energy levels separate. This effect is known as Zeeman splitting and is the basis for all NMR experiments. The Hamiltonian is:

$$\hat{H}_{\text{Zeeman}} = -\gamma \hat{I}_z \cdot \mathbf{B}_0 \quad (2.4)$$

where \mathbf{B}_0 is the magnitude of the magnetic field along the z axis and \hat{I}_z is the operator for the z component of the spin angular momentum. When subjected to the magnetic field the energy levels separate into $2I+1$ levels, where I is the nuclear spin. These energy levels are non-degenerate eigenstates and are labelled m .

2.3 Spin operators.

Since the $2I+1$ spin states are eigenfunctions of \hat{I}_Z the Schrodinger equation can be written as:

$$\hat{I}_Z |I, m_I\rangle = m_I \hbar |I, m_I\rangle \quad (2.5)$$

This equation states that measuring the value of \hat{I}_Z , the z component of the angular momentum, gives the current energy level, m_I , multiplied by \hbar , where $m_I \hbar$ is the energy of an individual state. This also enforces the idea that the outcome can only be integer multiples of \hbar .

If there is the term \hat{I}_Z , there must also be x and y components as well. These are \hat{I}_X and \hat{I}_Y which correspond to the x and y components of the spin angular momentum respectively.

However, these are often sandwiched together in the form of raising and lowering operators:

$$\hat{I}_+ = \hat{I}_X + i\hat{I}_Y \quad \hat{I}_- = \hat{I}_X - i\hat{I}_Y \quad (2.6)$$

These are collectively known as ladder operators [24]. The names raising and lowering come from their effect on the Zeeman eigenstates where the \hat{I}_- lowers the value of m_I by one and \hat{I}_+ increases it by 1. This can be viewed in relation to equation 2.6 as:

$$\begin{aligned} \hat{I}_+ |I, m_I\rangle &= \hbar \sqrt{I(I+1) - m_I(m_I+1)} |I, m_I+1\rangle \\ \hat{I}_- |I, m_I\rangle &= \hbar \sqrt{I(I+1) - m_I(m_I-1)} |I, m_I-1\rangle \end{aligned} \quad (2.7)$$

Operators, such as \hat{I}_Z , can also be expressed as a matrix. For spin quantum numbers the basic matrix is:

$$\hat{I}_Z = \begin{bmatrix} I & 0 & \dots & 0 \\ 0 & I-1 & \dots & 0 \\ \dots & \dots & \dots & \dots \\ 0 & 0 & \dots & -I \end{bmatrix} \quad (2.8)$$

For a spin $\frac{1}{2}$ nucleus this becomes

$$\hat{I}_Z = \begin{bmatrix} \frac{1}{2} & 0 \\ 0 & -\frac{1}{2} \end{bmatrix} \quad (2.9)$$

$$\hat{I}_+ = \begin{bmatrix} 0 & 1 \\ 0 & 0 \end{bmatrix} \quad \hat{I}_- = \begin{bmatrix} 0 & 0 \\ 1 & 0 \end{bmatrix}$$

Combining equations 2.6, 2.8 and 2.9 gives

$$\hat{I}_x = \frac{\hat{I}_- + \hat{I}_+}{2} \quad (2.10)$$

$$\hat{I}_y = \frac{\hat{I}_+ - \hat{I}_-}{2i}$$

or alternatively

$$\hat{I}_y = \begin{bmatrix} 0 & -\frac{i}{2} \\ \frac{i}{2} & 0 \end{bmatrix} \quad (2.11)$$

$$\hat{I}_x = \begin{bmatrix} 0 & \frac{1}{2} \\ \frac{1}{2} & 0 \end{bmatrix}$$

Note that the elements of the I_z matrix correspond to the populations in each energy level α or β of the two-level system for one spin $1/2$ nucleus.

2.4 Coherence

Coherence is the oscillation of spins that occurs between energy levels constructively. The generation of coherence is the basis of NMR experiments. Given two coupled spins there are 4 energy levels $\alpha\alpha$, $\alpha\beta$, $\beta\alpha$, $\beta\beta$, where $\alpha\beta$ and $\beta\alpha$ are degenerate. A single quantum transition could be any single change in state of adjacent energy levels such as $\alpha\alpha$ to $\alpha\beta$ or $\beta\alpha$ to $\beta\beta$, a change of $\alpha\beta$ to $\beta\alpha$ is a zero-quantum coherence. A transition can also occur from $\alpha\alpha$ to $\beta\beta$, this is known as double-quantum coherence.

To track changes in coherence a coherence transfer pathway is used which tracks the changing spin state of the system during the pulse program. A pathway will always start at a coherence level of 0, no matter where the pathway leads it must always be converted back to single-quantum coherence at the end for detection as double and higher quantum coherences cannot be detected. This is because they decay too rapidly and have a too high of a frequency for detection. Each pulse is only able to elicit a ± 1 change in coherence. During quadrature detection only one of the ± 1 pathways can be observed while the other is rejected, by convention this is typically the -1 coherence, allowing for the observation of $M+$, the magnetisation parallel to the z-axis. The other is removed via a quadrature detection scheme [5,25,26]. When performing 2D experiments the States method can be implemented as it allows for quadrature detection in in time domain, t_1 .

2.5 Internal and external Hamiltonian

In NMR the Hamiltonian can be decomposed into two components specific to the NMR system:

$$\hat{H} = \hat{H}_{\text{Internal}} + \hat{H}_{\text{External}} \quad (2.12)$$

Where $\hat{H}_{\text{Internal}}$ contains the terms that are only dependent on the local environment of the nucleus, such as the chemical shift, dipole-dipole coupling, J-couplings and quadrupolar interaction and $\hat{H}_{\text{External}}$ contains the ones directly affected by the NMR operator, the Zeeman interaction and its Hamiltonian, and the RF fields and their Hamiltonian. These can be easily separated by whether they are controlled externally by the operator or controlled internally by the structure of the sample [27][5].

When considering the internal Hamiltonian or $\hat{H}_{\text{Internal}}$ interactions, the secular approximation is appropriate. This states that these smaller interactions can be simply viewed as perturbations of the Zeeman interaction. NMR performed at high fields allows for the secular approximation to be used, also known as the high field approximation. The $\hat{H}_{\text{Internal}}$ are given by:

$$\hat{H}_{\text{Internal}} = \hat{H}_{\text{CS}} + \hat{H}_{\text{DD}} + \hat{H}_{\text{J}} + \hat{H}_{\text{Q}} \quad (2.13)$$

2.6 Chemical Shift Interaction

When placed into a magnetic field, the presence of electrons causes nuclei to be magnetically shielded. This arises because a current is generated in the electron cloud around a molecule and this in turn induces an electromagnetic field. Based on the local environment of atoms this induced magnetic field, B_{induced} , can either go along with the external \mathbf{B}_0 field, or against it, shielding or de-shielding the nucleus respectively. This shielding is primarily affected by electrons close to the nucleus, which means that the effect is fairly constant for a given atom. The chemical shift relates well to nearby electronegative groups which draw away electrons,

decreasing shielding and increasing the δ values for the given nuclei. In NMR δ , chemical shift, is the measure of resonance frequency of a nucleus.

$$\mathbf{B}_{\text{Local}} = \mathbf{B}_0 + \mathbf{B}_{\text{induced}} \quad (2.14)$$

In an NMR spectrum the position of the peaks is dictated by their Larmor frequency. If this were unaffected by the state of the local environment all the peaks would be seen at the same location and so provide no information, though luckily this is not the case since the $\mathbf{B}_{\text{induced}}$ slightly alters the Larmor frequency. The Hamiltonian for the chemical shielding is as follows:

$$\hat{H}_{CS} = -\gamma \hbar \hat{I} \cdot \sigma \cdot \mathbf{B}_0 \quad (2.15)$$

In the above equation σ is a second rank tensor called the chemical shielding tensor. This is a cartesian tensor represented by a 3x3 matrix.

This leads to defining the equation for $\mathbf{B}_{\text{induced}}$.

$$\mathbf{B}_{\text{induced}} = -\sigma^L \cdot \mathbf{B}_0 = - \begin{pmatrix} \sigma_{xx}^L & \sigma_{xy}^L & \sigma_{xz}^L \\ \sigma_{yx}^L & \sigma_{yy}^L & \sigma_{yz}^L \\ \sigma_{zx}^L & \sigma_{zy}^L & \sigma_{zz}^L \end{pmatrix} \cdot \begin{pmatrix} 0 \\ 0 \\ \mathbf{B}_0 \end{pmatrix} = \begin{pmatrix} \sigma_{xz}^L \mathbf{B}_0 \\ \sigma_{yz}^L \mathbf{B}_0 \\ \sigma_{zz}^L \mathbf{B}_0 \end{pmatrix} \quad (2.16)$$

It is important to note that the L specifies this is in the laboratory frame. Using the above equation, only the z component of the induced field is considered due to the secular approximation [28].

The zz component of the shielding is the only one required by the chemical shielding Hamiltonian because of the secular approximation. Since the non-zz components are so small as to be ignored, the Hamiltonian can be rewritten as:

$$\hat{H}_{CS} = -\gamma \hbar \hat{I} \cdot \sigma_{zz}^L \cdot \mathbf{B}_0 \quad (2.17)$$

2.7 Principal axis frame, Asymmetry and Anisotropy

Because this work concerns itself with the reintroduction of the chemical shift anisotropy it is important to identify its origin. Starting with a general tensor, \mathbf{R} , which like all second rank tensors involves a 3x3 matrix.

$$\begin{pmatrix} R_{xx} & R_{xy} & R_{xz} \\ R_{yx} & R_{yy} & R_{yz} \\ R_{zx} & R_{zy} & R_{zz} \end{pmatrix}$$

Tensors are often symmetric, or, if they are not, the asymmetric contributions are so similar as to have no effect on the overall NMR spectra. Because of this symmetry there are only six distinct components of a tensor, therefore it is possible to choose a reference axis in which \mathbf{R} is diagonal. Antisymmetric tensors have fewer components but cannot be diagonalised. This is the Principal Axis System (PAS). The laboratory frame can be transformed into the PAS and by using the using the XX, YY, ZZ components of the shift tensor the isotropic, anisotropic and asymmetry parameters can be defined [5].

The isotropic average of the tensor is the parameter that is observed in solution-state NMR and is described by:

$$\delta_{iso} = \frac{1}{3}(\delta_{XX} + \delta_{YY} + \delta_{ZZ}) \quad (2.18)$$

The anisotropy, ζ , and asymmetry, η , components, which are removed under MAS are defined as:

$$\zeta = \delta_{ZZ} - \delta_{iso} \quad (2.19)$$

$$\eta = (\delta_{YY} - \delta_{XX})/\zeta \quad (2.20)$$

where all the δ_{xx} etc are now in the PAS according to convention. Asymmetry is a dimensionless quality whose value falls in the range of 0 to 1.

It is important to state the convention used here for the ordering of the XX, ZZ, YY components as the Haeberlen convention where:

$$|\delta_{zz} - \delta_{iso}| \geq |\delta_{xx} - \delta_{iso}| \geq |\delta_{yy} - \delta_{iso}| \quad (2.21)$$

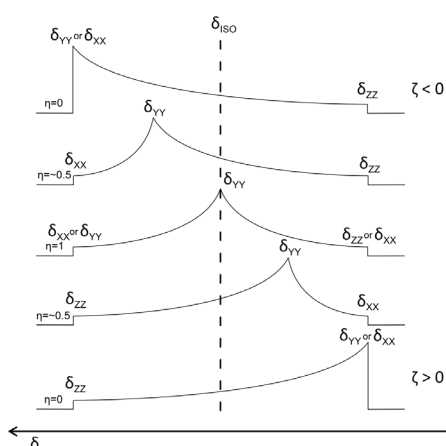


Figure 2-1 , the variations caused by asymmetry (η) on the CSA pattern when δ_{iso} and ζ are constant.

2.8 Dipolar Coupling

The interaction of two nuclear spin magnetisation through space is known as dipole-dipole or dipolar coupling. This term does not include J coupling, as that interaction is mediated via the electrons in bonds between molecules. In solution dipole coupling is averaged to zero due to the rapid tumbling of the molecule.

In the secular approximation the dipolar coupling can come in two versions, either homonuclear:

$$\hat{H}_{dd}^{homo} = -\left(\frac{\mu_0}{4\pi}\right) \frac{\gamma_I \gamma_S \hbar}{r^3} (3\cos^2\theta - 1) \left[\hat{I}_z \hat{S}_z - \frac{1}{2} (\hat{I}_x \hat{S}_x + \hat{I}_y \hat{S}_y) \right] \quad (2.22)$$

or heteronuclear:

$$\hat{H}_{dd}^{hetero} = -\left(\frac{\mu_0}{4\pi}\right)\frac{\gamma_I\gamma_S\hbar}{r^3}(3\cos^2\theta - 1)\hat{I}_z\hat{S}_z \quad (2.23)$$

where μ_0 is the permeability of free space, r is the distance between the two spins and θ is the angle between the external magnetic field and the internuclear vector. The reason for the loss of one of the bracketed terms from the homonuclear version is because this term is transverse. This term is only significant if the two spins I and S precess at or near the same resonance frequency. This happens only when I and S are the same nuclei with similar environments [28].

2.9 J-coupling

J -coupling, also known as scalar coupling or indirect coupling, is the interaction between two nucleotides mediated by electrons. It is a through-bond interaction and gives information on a molecular level about the connectivity and conformation of molecules [5]. The J -coupling Hamiltonian between two nuclear spins is given by:

$$\langle \hat{H}_J \rangle = 2\pi J_{IS} \hat{I} \cdot \hat{S} \quad (2.24)$$

The J -coupling has an anisotropic and isotropic component. The anisotropic component is so small that it can effectively be ignored, as in the Hamiltonian above. The isotropic component is the average of the diagonal elements of the J -coupling tensor and is observed in solution. However, the size of these interactions is in the 100 Hz range and so they are much smaller than the standard solid-state NMR linewidth and in general they can be ignored in solid-state NMR, but they are observed in a refocused INADEQUATE experiment.

J -coupling has been employed in solution-state NMR for years as it provides definitive identification of through-bond chemical connections. They provide an advantage over dipole-dipole coupled experiments as these cannot separate through-space close proximity

connections to directly bonded connections and are not observed in solution anyway. The INADEQUATE technique used in this thesis is one such technique. Originally a solution-state technique, it has additional pulses added to remove anti-phase contributions leading to the refocused INADEQUATE technique for solid-state NMR. This technique, when applied to an isolated J -coupled spin pair, produces a pair of in-phase correlation peaks at the double quantum frequency in the indirect dimensions between chemically bonded carbons [29].

2.10 Quadrupolar interaction.

The quadrupolar interaction arises in nuclei where the spin is greater than $\frac{1}{2}$, which is the vast majority of cases. When the spin is $\frac{1}{2}$ the electronic charge is symmetrically distributed and so has no directional dependence. This is because of the two anti-parallel dipoles experience a torque attempting to align to B_0 . Because the size of the two torques is equal and opposite the net effect is zero. If the spin is $>\frac{1}{2}$ then one of the dipoles is larger than the other, this leads to a net torque being exerted due to the charge distribution being asymmetric, this allows the electric field gradient to exert a torque on the nucleus. This, in combination with the angular momentum of the nuclei, leads to the dipole precessing around the electric field gradient [30].

The Hamiltonian for the quadrupolar interaction is as follows:

$$\hat{H}_Q = \frac{eQ}{6I(2I-1)\hbar} \mathbf{I} \cdot \mathbf{e}\mathbf{q} \cdot \mathbf{I} \quad (2.25)$$

The terms included are, e , the elementary charge, Q , the electric quadrupolar moment, I , the nuclear spin quantum number, \hbar , the reduced Planck constant and $\mathbf{e}\mathbf{q}$, the electric field gradient tensor.

2.11 Density operator

When considering the spin states in NMR across multiple spins it becomes tedious to consider each individually. Where there are only a handful of spins calculations are relatively simple, otherwise with larger number of spins averaging the spins allows for more streamlined calculations. Given a spin $\frac{1}{2}$ nuclei its wavefunction, ψ , is a composition of its two eigenstates:

$$|\psi\rangle = \begin{pmatrix} c_\alpha \\ c_\beta \end{pmatrix} \quad (2.26)$$

Where α and β represent different spin states, with β being the higher energy level spin state.

The expectation value of an operator \hat{Q} is given by:

$$\langle \hat{Q} \rangle = \langle \psi | \hat{Q} | \psi \rangle \quad (2.27)$$

$$\begin{aligned} &= (c_\alpha^* \quad c_\beta^*) \begin{pmatrix} Q_{\alpha\alpha} & Q_{\alpha\beta} \\ Q_{\beta\alpha} & Q_{\beta\beta} \end{pmatrix} \begin{pmatrix} c_\alpha \\ c_\beta \end{pmatrix} \\ &= c_\alpha c_\alpha^* Q_{\alpha\alpha} + c_\beta c_\alpha^* Q_{\beta\alpha} + c_\alpha c_\beta^* Q_{\alpha\beta} + c_\beta c_\beta^* Q_{\beta\beta} \end{aligned}$$

The above expression focuses on the quadratic products of the superposition coefficients c_α and c_β [31]. These quadratic products can be used to represent the spin state on their own by forming a matrix of the multiplication of the column and row vectors.

$$\begin{aligned} |\psi\rangle\langle\psi| &= \begin{pmatrix} c_\alpha \\ c_\beta \end{pmatrix} (c_\alpha^* \quad c_\beta^*) \\ &= \begin{pmatrix} c_\alpha c_\alpha^* & c_\alpha c_\beta^* \\ c_\beta c_\alpha^* & c_\beta c_\beta^* \end{pmatrix} \end{aligned} \quad (2.28)$$

It is worth noting that the ordering of multiplication is important as $\langle \psi | \psi \rangle = 1$ because of orthonormality. The expectation value of \hat{Q} can now be given as:

$$\langle \hat{Q} \rangle = Tr\{|\psi\rangle\langle\psi|\hat{Q}\} \quad (2.29)$$

where Tr is a trace, this is the sum of the diagonal matrix elements of an operator [31].

This can be expanded to go beyond a single spin, for n spins it takes the form:

$$\langle \hat{Q} \rangle = Tr\{|\psi_1\rangle\langle\psi_1|\hat{Q} + |\psi_2\rangle\langle\psi_2|\hat{Q} + \dots + |\psi_n\rangle\langle\psi_n|\hat{Q}\} \quad (2.30)$$

This can include all the spins in an ensemble, where the sum of all spins can be taken. An operator $\hat{\rho}$ can be defined as:

$$\hat{\rho} = N^{-1}(|\psi_1\rangle\langle\psi_1| + |\psi_2\rangle\langle\psi_2| + \dots) \quad (2.31)$$

where N is the number of spins in the ensemble. To avoid writing out all spins, this can be shortened to:

$$\hat{\rho} = \overline{|\psi\rangle\langle\psi|} \quad (2.32)$$

Where the overbar is used to represent the average over N . This new operator, $\hat{\rho}$, is the density operator, density being a misnomer as it has no relation to the actual density of the physical sample.

With $\hat{\rho}$ the expectation value of \hat{Q} can now be simplified to:

$$\langle \hat{Q} \rangle = tr(\hat{\rho}\hat{Q}) \quad (2.33)$$

An example of this could be as follows. In the context of nuclear spins within a magnetic field, the equilibrium state corresponds to a net magnetization along the z-axis. There is an excess of $M_0/2$ nuclear spins in, for example, the α state vs the β beta state. The density matrix for this equilibrium state would be written as:

$$\rho = \begin{pmatrix} M_0/2 & 0 \\ 0 & -M_0/2 \end{pmatrix} \quad (2.34)$$

Using this it is possible to work out the expected values of spin angular momentum for the operators.

$$\langle \hat{I}_z \rangle = \text{tr}(\hat{\rho} \hat{I}_z) = \text{tr} \left[\begin{pmatrix} M_0/2 & 0 \\ 0 & -M_0/2 \end{pmatrix} \begin{pmatrix} \frac{1}{2} & 0 \\ 0 & -\frac{1}{2} \end{pmatrix} \right] = M_0/2 \quad (2.35)$$

$$\langle \hat{I}_x \rangle = \text{tr} \left[\begin{pmatrix} M_0/2 & 0 \\ 0 & -M_0/2 \end{pmatrix} \begin{pmatrix} 0 & \frac{1}{2} \\ -\frac{1}{2} & 0 \end{pmatrix} \right] = \text{tr} \begin{pmatrix} 0 & 0 \\ 0 & 0 \end{pmatrix} = 0$$

In other words, the average state in this context signifies a complete alignment of the magnetization along the z-axis [5].

This equation, 2.35, does not account for the changes in state over time. The relative population of the eigenstates at thermal equilibrium is given by the Boltzmann distribution, whose density operator is.

$$\hat{\rho}_{eq} = \frac{1}{Z} e^{-h\hat{H}/kT} \quad (2.36)$$

In this equation \hat{H} is the total spin Hamiltonian and Z is the normalization factor. This Z is also known as the canonical partition function, and simply sums up the statistical probability of all possible states a system can be in. Since in the nuclear spin energies are small compared to the thermal energies, the exponential can be expanded to

$$\hat{\rho}_{eq} = \left[\hat{1} - \frac{h}{kT} \hat{H} \right] / (2I + 1) \quad (2.37)$$

In this case Z equals the total number of spin states, 2I+1. The identity operator, $\hat{1}$, represents an equal distribution of population across all the different states. However, this term can ultimately be dropped as it does not evolve under \hat{H} . The second term is related to the

population change as the energy levels lose their degeneracy. Because of this $\hat{\rho}_{eq}$ can be transformed into the reduced density operator $\hat{\rho}_{eq}'$ which gives the change in population in the density operator from a situation of equal population. By working with the secular approximation $\hat{H} \approx \hat{H}_{Zeeman}$. This all ultimately leads to:

$$\hat{\rho}_{eq}' = -\frac{\hbar}{(2I+1)kT} \hat{H} = M \hat{I}_Z \quad (2.38)$$

Where M is a constant of proportionality that is used to express the size of nuclear spin magnetization.

The time evolution of the density operator under the Schrödinger equation is given by the Liouville-von Neumann equation:

$$\dot{\hat{\rho}} = \frac{d\hat{\rho}}{dt} = -2\pi i [\hat{H}, \hat{\rho}] \quad (2.39)$$

The formal solution to this may be written as

$$\hat{\rho}(t) = \hat{U}(t, 0) \hat{\rho}(0) \hat{U}^\dagger(t, 0) \quad (2.40)$$

where $\hat{\rho}(0)$ is the density operator at thermal equilibrium and $\hat{U}(t, 0)$ is a unitary propagator, a matrix responsible for the spin dynamics from 0 to t [5]. The simulation of NMR experiments is essentially the evaluation of the Liouville-von Neumann equation of motion. This is how SIMPSON, the NMR simulation tool used in this work, functions. SIMPSON functions by breaking the total time, zero to t, into small increments of $n\Delta t$, where each section can be considered time independent, allowing for simpler calculations [32].

2.12 FIDs and pulse programs

The rf pulse has associated with it an oscillating magnetic field, directed perpendicular to B_0 , which interacts with the nuclei. This, if the resonance condition is met, leads to the nuclear magnetisation precessing around the direction of the rf field as opposed to B_0 . Once the pulse is over the nuclei begin to relax back to their original orientation. As they relax back, they give out energy in the form of rf waves. These cause a change in the voltage across a coil surrounding the sample. These changes are recorded as a function of time, leading to the collection of a free induction decay (FID). The FID is generated in the time domain and is a collection of all precession frequencies. An FID can be analysed directly though it is far more common for it to be Fourier transformed, converting the time dimension into frequency [5]. The Fourier transformation equation is given below where ξ is frequency and x is time.

$$\hat{f}(\xi) = \int_{-\infty}^{\infty} f(x)e^{-i2\pi\xi x} dx \quad (2.41)$$

A Fourier transformation, FT, occurs, in a simple sense, by multiplying the FID by varying frequency cosine waves. The FID itself is a collection of many cosine waves. If this were to be multiplied a single cosine wave that matched the frequency of one of the waves contained in the FID then the product would have only positive intensities, if the phases were aligned. This is because the oscillation will synchronise so that the signs of the frequencies are always the same, leading to the integration of the product wave, at the frequency of the tested cosine wave, to be a positive value. The further away from the matching frequency the multiplied wave gets the less aligned the signs become and so the signal becomes 0. Hence when the Fourier transformation gives a non-zero result it signified the frequency of one of the components of the FID [26].

Almost all NMR experiments have more than one pulse, this is what allows for greater complexity. NMR pulse programs typically function via a series of pulses and delays across one or more channels. Each of these channels are tuned to be able to excite a different nucleus, with the most common two being proton and carbon-13. Multi-pulse experiments also allow for multi-dimensional NMR. The multi-dimensional experiments used in this work are correlation experiments. These contain two (or more) dimensions that indicate spins which correlate with one another via couplings for example. Two-dimensional NMR experiments are made up of several different time periods. The first being the preparation time, in which a delay is used to allow the magnetisation to return to thermal equilibrium. The second is an excitation time where magnetisation is generated, in a 1D experiment this is then followed by detection. When compared to a standard 1D NMR pulse sequence there is an additional, variable, delay inserted after excitation in a 2D experiment under which the magnetization evolves. Following this is a mixing period, during which magnetization that has evolved on one spin is transferred to another prior to detection [5].

2.13 Relaxation

As mentioned, NMR functions by manipulating the spins to be able to generate signal. Performing a single set of pulses results in a low signal to noise ratio (SnR). To improve the SnR, multiple repetitions, or numbers of scans (NS), are performed. SnR increases in accordance with $NS^{1/2}$, in other words to double the SnR, a four-fold increase in the number of scans is required [25]. These scans cannot be performed continuously as NMR experiments are designed to work on a system at thermal equilibrium. The process by which the system returns to equilibrium is known as relaxation. There are two primary types of relaxation, transverse and longitudinal relaxation.

When the spins are subject to a rf pulse their net magnetisation is transferred to be perpendicular to \mathbf{B}_0 in the case of a 90° pulse. Once the pulse is over the spins begin to precess around \mathbf{B}_0 and transition from being pointed perpendicular to \mathbf{B}_0 to being aligned with it, this is often called the T_1 time. This is known as longitudinal relaxation.

The other type, transverse relaxation, comes from the fact that the spins precess around \mathbf{B}_0 at different rates. The time constant describing this stochastic dephasing is T_2 . The longer that T_2 is, the higher the resolution of the spectrum.

The rate at which relaxation occurs is dependent on the local environment of the nuclei in question. Therefore, the time between scans must be sufficient to allow a significant portion of the relaxation to take place. The amount of magnetization that returns to equilibrium can be estimated using the Bloch equations. These equations consider the T_1 and T_2 relaxation

times as phenomenological times, which can be determined through experimental measurements. They illustrate how the magnetization changes as a function of time [33].

2.14 Signal Sampling

For NMR signal detection small wire coils are located around the sample. These sense tiny, μV , levels of change in voltage. This is too low for the signals to be properly digitised, so they are first passed through an amplifier. Detection of these signals is phase sensitive and when being converted to digital data that can be stored and processed the signal must be sampled at different points to obtain values of time and intensity.

Sampling rates too short are not usually a problem outside of increased computational time. If the sampling rates are too low, then the actual signal can be lost. This is because lower frequency oscillations can fit into the same sampled points. An appropriate sampling rate of the FID can be calculated using the Nyquist frequency, f_{max} , this is the highest frequency that can be properly sampled and is given by $f_{\text{max}} = \frac{1}{2\Delta}$. In this case Δ is the sampling interval, often referred to as the dwell time, dw . The spectral width, sw , the ppm range on the spectrum, is related to the dwell time by $sw = \frac{1}{2dw}$, assuming the Redfield method which is standard across Bruker instruments.

Another important factor in signal acquisition is phase. This typically uses quadrature detection with receivers set to x, y, -x, -y, these are not located at these points but the y is a mixture of the x signal with the rf signal, the other two a simply negatives. This can compensate for miss-setting of the phase by implementing cyclically ordered phase sequences, CYCLOPS, to remove artifacts that would otherwise be present [34]. With single channel detection then it would not be possible to ascertain which way around B_0 a spin is

precessing. When a signal is detected along the x-axis, both its x and y components are detected, this allows for the recording of both the 'real' and 'imaginary' components. In simple experiments, the receiver's phase merely needs to follow the pulse's phase. Phase cycling comes into play to eliminate undesired signals, such as those produced by an X contact pulse in a cross-polarization experiment. Furthermore, phase cycling allows for coherence selection.

Chapter 3: DNP theory

Dynamic Nuclear Polarisation (DNP) is the process of signal enhancement in NMR by transfer of the larger spin polarization of an electron to the nucleus of interest. This transfer of polarisation helps combat the low sensitivity of NMR by increasing the signal acquired. The electron used is provided by a radical, this is added in a solution during sample preparation. Since the commercialisation of DNP with the advent of high-power high frequency gyrotrons, used for the microwave irradiation, the application of DNP has increased [35].

The maximum possible enhancement is found by the ratio of the gyromagnetic ratio of the examined nuclei over that of an electron. This means for proton NMR, the maximum possible enhancement is ~ 658 , though this is a theoretical value and achieving this or relatively similar in practicality is near impossible [36].

3.1 Instrumentation

Due to the mechanisms involved and their required conditions DNP requires additional apparatus from conventional NMR, the most obvious addition coming in the form of a gyrotron, or another microwave source. The gyrotron in this work operates at a frequency of 395 GHz allowing it to be used with its accompanying 600 MHz NMR magnet. Modern gyrotrons can operate continuously as high as 527 GHz for the use of DNP [37,38].

The gyrotron operates at 100 K and is cooled via cold nitrogen gas. The gyrotron functions via the cyclotron resonance mechanism to generate microwaves which are then transferred to the NMR sample. This low temperature of the gyrotron is mirrored in the low temperature of the NMR sample itself which is also around 100 K. This is because the DNP effect also benefits from being at these low temperatures due to slowing of electron relaxation at this

temperature, allowing for transitions to be more easily saturated [39,40]. However, due to the increased viscosity of nitrogen gas at about 100 K the rotor speeds are limited to 12-15 kHz for a 3.2 mm rotor, as opposed to about 25 kHz at room temperature. DNP has been performed on 0.7 mm rotors, spinning up to 65 kHz at 100 K which showed that the DNP effect increases at faster spinning speeds [41,42].

3.2 Radicals and solvent

Currently there are two types of radicals that are used for DNP: mono- and bi-radicals. Mono-radicals were the first to be employed for the use in DNP with nitroxide radicals being the most widely used [43]. Recently though it has been shown that biradicals give higher signal enhancements with DNP. In the case of the radicals used in this work there are fixed distances and orientations between the two electron g tensors as opposed to the distance and orientation between them being governed by randomly dispersed mono-radicals [44,45]. When synthesising bi-radicals the bond lengths and angles can be manipulated so that the g -tensor satisfies equation 3.2.

One factor in DNP is sample preparation and which radical/solvent to use. A reason this is more important than in other types of NMR analysis is that the sample should not form a solution in the solvent, but ideally should be 'covered' in a solution of the solvent/radical but not dissolved. This is because dissolving the sample would change its solid-state structure and so this approach would be unsuitable for pharmaceuticals or materials. In this work both aqueous and organic solvents are employed with AMUPol and TEKPol being the two radicals employed. For samples which do not dissolve in water it is common to use a mixture of glycerol/D₂O/H₂O, in combination with the radical AMUPol which dissolves in water. For

samples which are hydrophobic TCE (trichloroethylene) is often the preferred solvent and TEKPol is the radical of choice [46].

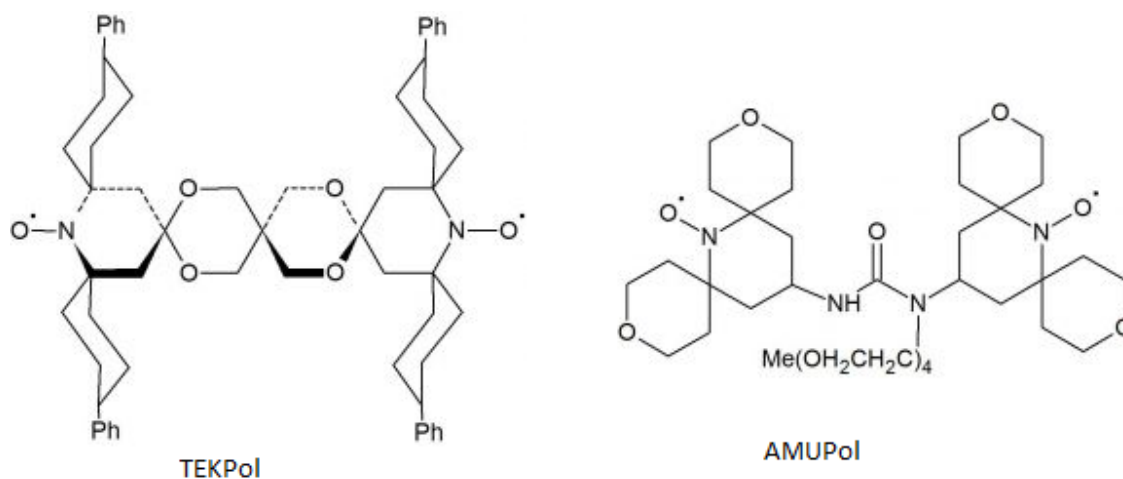


Figure 3-1, the structures of the bi-radicals TEKPol and AMUPol.

The solvent should also not crystallise at low temperatures as this can lead to separation of the radical and the sample leading to lower enhancement. Instead, it should form an amorphous glassy matrix to uniformly disperse the radical and solvent [47]. New radicals are still being developed to provide greater enhancements and ease sample preparation issues [48].

3.3 Mechanism and enhancement

There are multiple DNP mechanisms, including: the Overhauser effect[49], the solid effect[50], thermal mixing[51], and the cross effect. These mechanisms vary in the way they achieve the increased polarization, for example the solid effect involves a two-spin system, electron-nucleus, whereas the cross effect involves a three-spin system, electron-electron-nucleus. They also differ in the conditions they use, such as the type of radical and the temperature at which they perform best [43]. In the DNP experiments contained in this thesis the cross effect was the only one used.

3.4 Cross effect

The cross effect is a complex three spin process first discovered then documented in the 60's and makes use of a bi-radical [52]. For simplicity, the process will be discussed first as if it were under static conditions.

The Hamiltonian that governs the cross effect under static conditions is given below

$$\hat{H} = \omega_{0S_1}\hat{S}_{1Z} + \omega_{0S_2}\hat{S}_{2Z} - \omega_{0I}\hat{I}_Z + (A^1_{ZZ}\hat{S}_{1Z}\hat{I}_Z + A^1_{ZX}\hat{S}_{1Z}\hat{I}_X + A^1_{ZY}\hat{S}_{1Z}\hat{I}_Y + A^2_{ZZ}\hat{S}_{2Z}\hat{I}_Z + A^2_{ZX}\hat{S}_{2Z}\hat{I}_X + A^2_{ZY}\hat{S}_{2Z}\hat{I}_Y) + d(3\hat{S}_{1Z}\hat{S}_{2Z} - \vec{S}_1 \cdot \vec{S}_2) - 2J\vec{S}_1 \cdot \vec{S}_2 \quad (3.1)$$

The first two terms are the two electron Zeeman interactions, the third term being the nuclear Zeeman interaction. The fourth bracketed term represents the hyperfine interaction between the electrons and the nucleus. Note the A^1_{ZZ} component is secular and can be considered constant over time while the A^1_{ZX} and A^1_{ZY} components are not. The fifth term is the electron-electron dipole coupling and the sixth is the exchange coupling [53–55].

The cross effect occurs between the two electrons, provided by the bi-radical, and a solvent nucleus via an electron-nuclear hyperfine coupling. The key condition with the cross effect is that the difference in the effective Larmor frequency of the two electron spins must match the nuclear Zeeman frequency, as shown in the equation below.

$$\omega_{0S_1} - \omega_{0S_2} = \omega_{0I} \quad (3.2)$$

Once the equation for the cross effect (3.2) is satisfied, the cross effect can be explained in three stages. The first is the saturation of an electron transition via microwave irradiation, this can be seen in Figure 3-2 by the solid line. Because 3.2 is satisfied, the energy levels $\alpha\beta$ and $\beta\alpha$ are degenerate. This degeneracy leads to population averaging, this is stage two. The final stage is the same process that occurs in conventional NMR where there is a nuclear

transition from $\beta\alpha\alpha$ to $\beta\alpha\beta$. However, the larger population at $\beta\alpha\alpha$ than there would be based simply on the Boltzmann distribution means the signal generated is much larger.

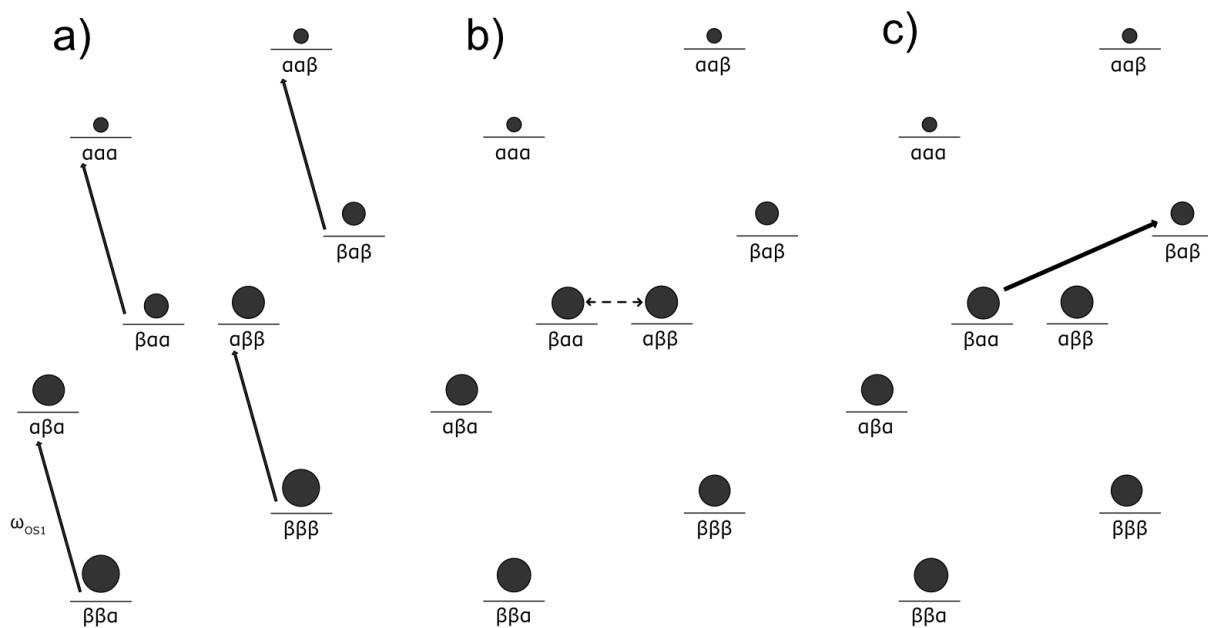


Figure 3-2, the energy level diagrams involved in the cross effect. a) the saturation of one electron transition, shown by the solid arrow. b) The degeneracy of the $\alpha\beta\beta$ and $\beta\alpha\alpha$ shown by the dashed arrow. c) the nuclear transition which gives rise to the NMR signal. The order of the spin states goes electron-electron-nucleus.

It is the ω_0^{S1} transition that is saturated to be able to provide a positive enhancement. If the ω_0^{S2} transition is saturated, then this leads to a negative enhancement. This is because it leads to an increase in the population of the higher nuclear spin state as opposed to the lower. The linewidth of the EPR spectrum increases at higher magnetic fields because of increased inhomogeneity. This is why the introduction of high power, high frequency gyrotrons has been instrumental as to counteract the increased inhomogeneity and provide sharp EPR linewidths [56].

The difference when a sample is under MAS is that there are varying matching conditions due to the spinning. Under MAS there are three key events that occur periodically and not at the same time, these are:

1. The μw (microwave) events, this is where the μw frequency is on resonance with only one of the electron spins. This leads to polarization build-up which can be transferred.
2. The CE (Cross effect) matching events, where equation 3.2 is satisfied.
3. e-e events. This is where the two electron spins have equal Larmor frequency.

The e-e events are of great importance as without them saturation would lead to the effective cancellation of the cross effect. These allow for the polarization transfer between the two electron spins and results in an overall net positive polarization enhancement. Without this there would be periods of negative and positive enhancement that cancelled [43].

3.5 Spin diffusion

The cross effect occurs between the two electrons from the bi-radical and the nucleus of a solvent molecule. This increased polarization must then be transferred to the sample to be able to achieve the increased signal generation. The solvent nucleus can transfer its polarization to an adjacent solvent nucleus via spin diffusion, a dipolar mechanism, and so this increased polarization will be transferred away from the radical and will be averaged across the solvent. The gyrotron is left on throughout the experiment so that the cross effect continues to occur. This provides a constant source of the increased polarization.

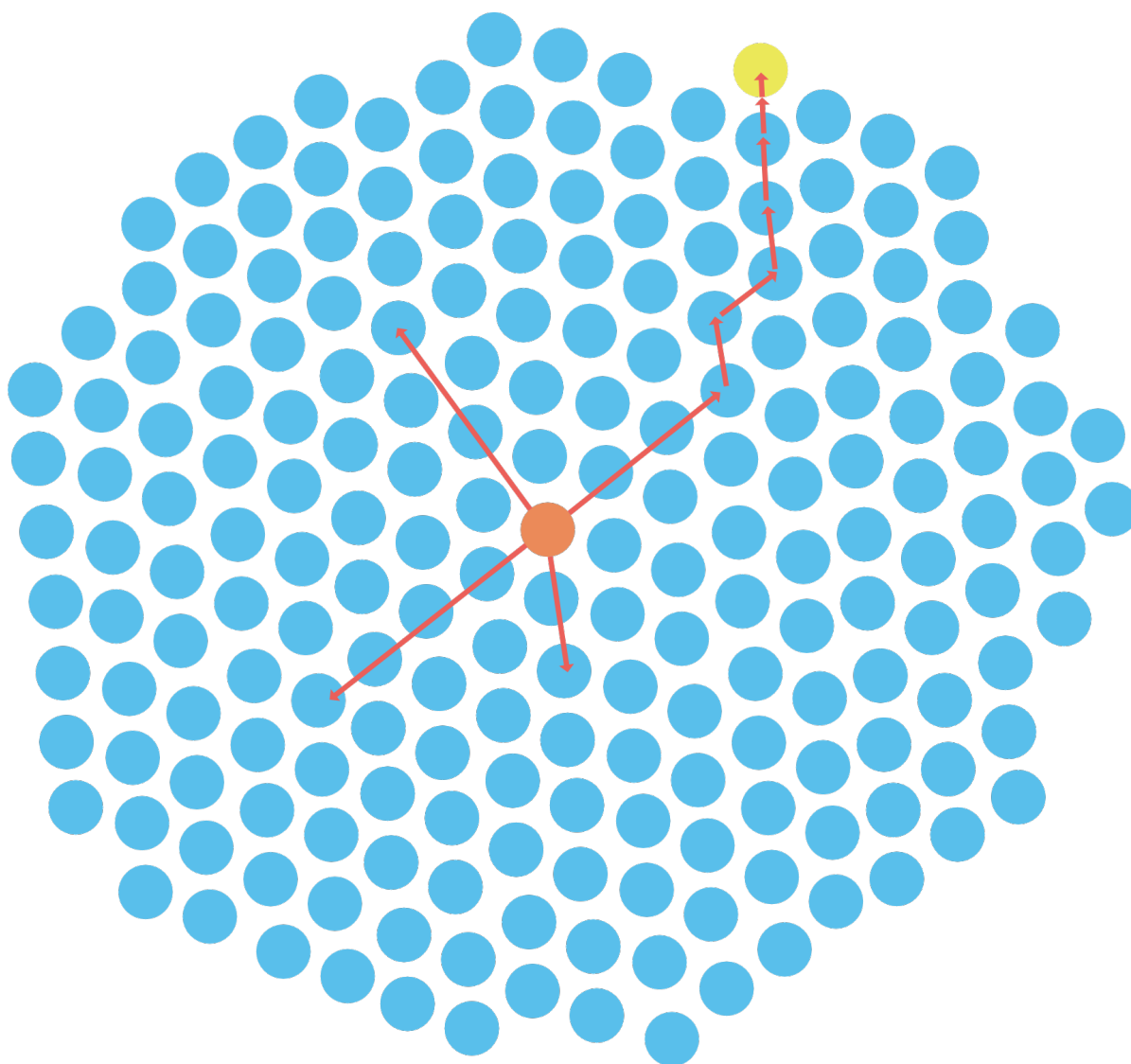


Figure 3-3, This figure represents the spin diffusion (red lines) of the increased polarization provided by the radical (orange) to the solvent (blue) and ultimately to the sample (yellow).

Because the neighbouring solvent molecules must have degenerate energy levels, so that the transfer can occur, if the analyte is too close to the radical then it will be bleached and so will not produce signal. Any solvent molecules too close to the radical will have different energy levels due to their proximity to the radical and any spin diffusion will not be efficient enough to have an effect. The term radical spin diffusion barrier is used to describe the range of the radicals bleaching effect, with anything being in the barrier being bleached.

For DNP, the concentration of the radical is important as too high a concentration and the sample will be too close to the radical, and no signal will be obtained because all the sample is bleached by the radical. Optimization of the concentration of the radical allows enough to be able to interact with the sample, without over saturation. The other key factor is the proton density of the solvent. Too large a proton density means that spin diffusion will be too great, and the sample signal will be quenched, while too small a proton density means there will be insufficient medium for the polarization to pass through [57].

After spin diffusion, cross polarization will occur to allow the transfer of this polarization to the nucleus of interest. The radical being too far from the sample also poses a problem as the increased polarization will be lost due to cumulative losses during the spin diffusion process.

Because spin diffusion is not instantaneous, a time is required for the polarization to be transferred. This can be measured using a saturation recovery experiment, this is an experiment which measures the signal generated at increasing delays between each sampling increment. This is conventionally used to measure the T1 relaxation time of a nucleus but can also be used to measure the amount of time required for the polarization to be transferred in DNP. Optimizing the length of the polarization transfer step is crucial to maximize the potential enhancement achievable in DNP. If the length of the transfer step is too short, the potential enhancement may be compromised, resulting in a lower than optimal polarization transfer.

3.6 Cross polarization

Cross polarization is the final step in indirect DNP regardless of which mechanism is used. This is the step where the increased polarization is used to give an increase in the signal. Cross polarization is used widely in solid-state NMR to transfer magnetization via dipolar coupling from nuclei with high γ to ones with low γ , the result of this is an enhancement in the low γ nucleus signal. In many cases, the high γ is ^1H and the low γ is ^{13}C . For cross polarization to occur between two nuclei a condition called the Hartmann-Hahn matching condition must be met. This involves matching the frequency of the first, abundant nucleus, typically ^1H , to the second nucleus, allowing for polarization to be transferred. Once this has been met the abundant nucleus is decoupled while the low γ one is observed [58].

3.7 Evaluating the effect of DNP

When evaluating the increase in signal obtained with DNP, the DNP enhancement, ε , is calculated by assessing the number of times greater a signal is while the microwaves are on vs the signal size when they are off [35]. The key comparison, however, is between a standard NMR spectrum and a DNP acquisition time of the same sample, one way of doing this would be by comparing the signal/noise per unit of time in a DNP experiment to the same parameters in a standard solid-state NMR experiment. An example equation of this is given below where the enhancement, ε , is the ratio of the signal to noise ratio, SnR, over the relaxation time, D_1 . This is assuming other factors such as the number of scans remain consistent.

$$\varepsilon = \frac{\text{SnR(DNP)}}{D_1(\text{DNP})} / \frac{\text{SnR(Standard)}}{D_1(\text{Standard})} \quad (3.3)$$

One way of assessing the effect of DNP is the absolute sensitivity ratio. This is a more complex comparison taking in to account more factors such as signal bleaching and the weight ratio of samples. This has problems associated with it as it requires multiple spectra to be analysed such as the neat preparation of the same sample mass as the DNP preparation, as it is a comparison of DNP to a conventional NMR equivalent, and still does not produce a value which is comparable between samples due to the temperature difference between them [59].

The enhancement that DNP provides varies significantly across compounds as well as across samples of the same compound. An example of this is comparing the enhancement of casopitant mesylate to allopurinol. After an iterative process of sample prep, varying the concentration and volume of the radical, for casopitant mesylate we were able to increase the initial enhancement of 1.1 to around 1.8. In comparison, without any optimisation, allopurinol had an enhancement of ~100 across all nuclei. This highlights how DNP sample preparation can be the hardest part of the whole process.

One consideration when comparing these two compounds is that Casopitant mesylate has methyl groups which act as magnetisation sinks leading to a lower enhancement.

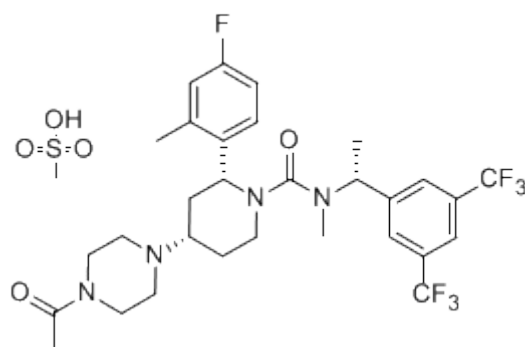


Figure 3-4, the chemical structure of Casopitant mesylate.

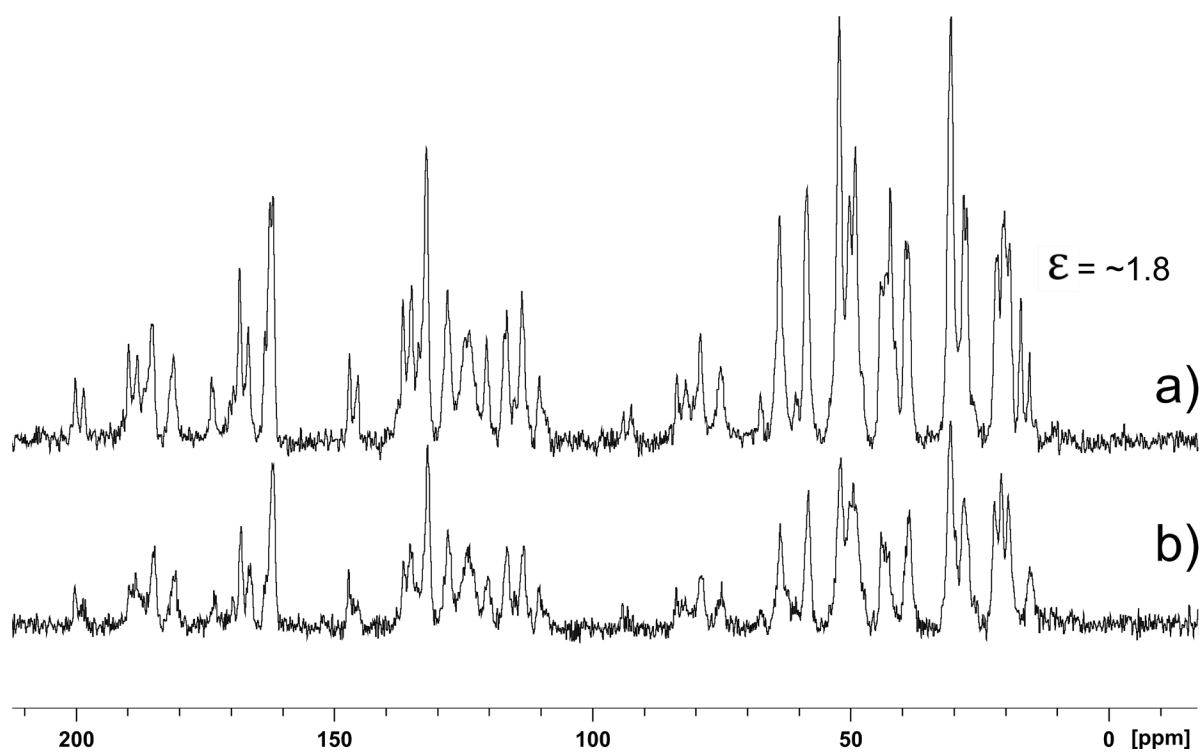


Figure 3-5, ^{13}C CP-MAS-MAS NMR spectra for Casopitant mesylate: a) DNP-enhanced with 15 μl of 60 mM TEKPol/TCE with 40 mg of sample, b) the same sample with the gyrotron off. Both were recorded on a 600.13 MHz magnet for 8 scans with a contact time of 2000 μs .

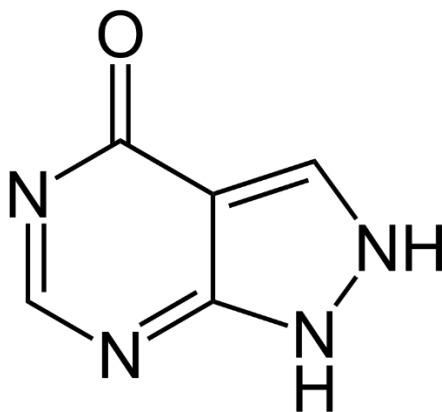


Figure 3-6, the chemical structure of Allopurinol

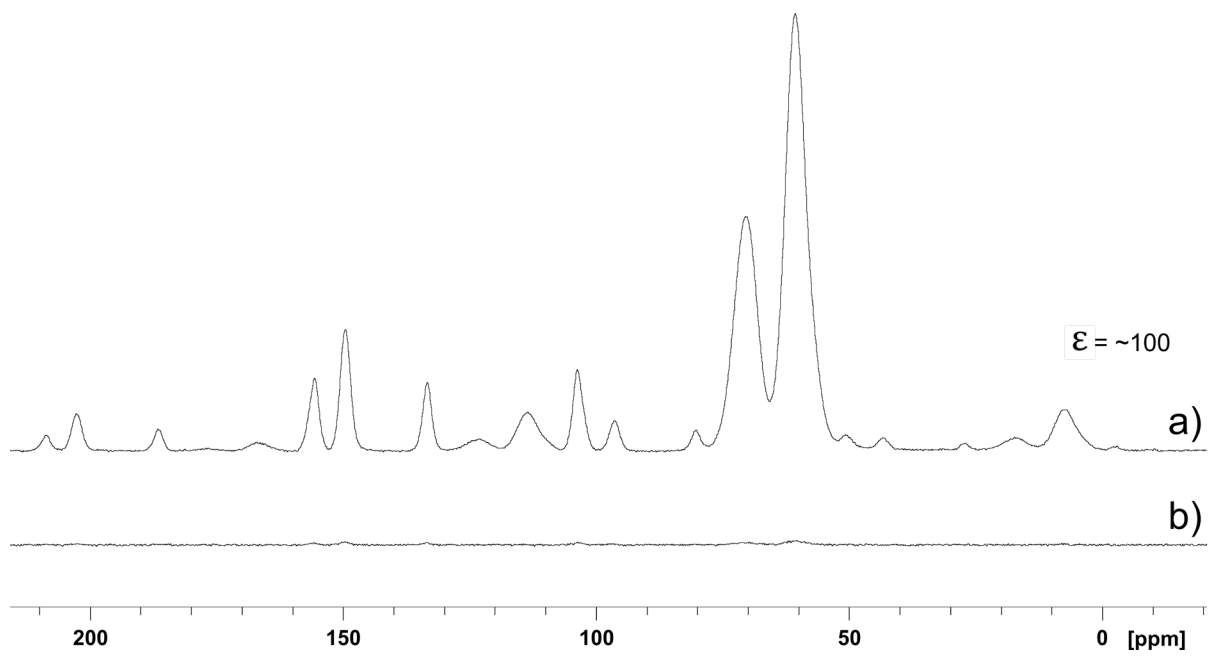


Figure 3-7, ^{13}C CP-MAS-MAS NMR spectra for Allopurinol: a) DNP-enhanced with 20 μl of 20 mM AMUPOL in glycerol/ with 40 mg of sample, b) the same sample with the gyrotron off. Both were recorded on a 600.13 MHz magnet for 8 scans with a contact time of 2000 μs .

Chapter 4: CSA Recoupling

4.1 Symmetry based recoupling principles.

During the early era of solid-state NMR two paths of progression were developed in parallel, centred around two types of methods: either MAS or pulsed methods, separate manipulation of the space and the spin parts of the nuclear spin Hamiltonian, respectively. In the 1980's this began to change, as groups started designing experiments that coupled both manipulations [60,61]. After this symmetry-based recoupling sequences started to be developed, such as HORROR and DRAMA [62,63,64]. Much of the groundwork for this thesis was laid out by Malcolm Levitt who published a paper detailing the setup of the symmetry-based recoupling sequences used in this work [65].

Interactions such as the dipole-dipole coupling, and the chemical shift anisotropy can be 'recoupled' or suppressed depending on manipulations of the spin and space components of the overall spin Hamiltonian of a nucleus. The space part is affected by rotating the molecular framework and the spin part is modulated via the application of radio frequency pulses. There is also the rotation of the magnetic field, though this is not normally considered due to the complication of rotating the rather heavy magnet. The important point about the interactions is that they all have different ranks for their spin and space parts. This allows them to be separated. Below is a table of rotational properties or 'ranks' for spin 1/2 homonuclear interactions.

<i>Interaction</i>	<i>Space rank, L</i>	<i>Spin rank, λ</i>	<i>Field rank</i>
<i>Isotropic Chemical shift</i>	0	1	1
<i>Chemical shift anisotropy</i>	2	1	1
<i>J-coupling</i>	0	0	0
<i>Dipole-dipole coupling</i>	2	2	0

Table 4-1, The spin, space and field rank for the four largest interactions in proton NMR.

Taking the example of chemical shift anisotropy, which has 2,1,1 for its space, spin and field rank, respectively. The space component is rank 2 and, as with all other rank 2 components, has the rotational symmetry of a d-orbital. This means that there would be no change in the sign of the interaction if the molecule were rotated through 180° assuming the spin and magnetic field were constant. The spin and field rank in this case are rank 1, this means they have the rotational symmetry of a p-orbital. This means, given a fixed space and field, a rotation of the spin through 180° would cause an inversion of the sign of the interaction. Interactions which have a rank 0 have the rotational symmetry of an s-orbital and so their sign is unaffected by changes in space, spin or field.

For each interaction there are multiple components that make up the overall interaction. Given an irreducible spherical tensor space rank of l there will be $2l+1$ components, ranging from $-l$ to $+l$ in m integer steps, whereas for the spin rank, λ , it is split into its spin components μ . Specific values of l , m , λ , μ can be obtained while suppressing other interactions. This can be done via manipulation of the rotor and rf rotations.

4.2 R and C sequences

There are two types of spin sequences, C and R sequences [66]. Using the notation for general C and R sequences, CN_n^v & RN_n^v , N , v and n are consistent between both types of sequences. They signify that n rotations of the rotor occur while v changes of the phase occur, within N evenly spaced intervals. Each N is made up of a series of pulses that rotate the magnetization through 360° for C sequences and 180° for R ones. Because the phase of R sequences can only rotate by 180° at a time there must be an even value for N . This means that the phase shifts by $2\pi v/N$ or $\pi v/N$ for C and R sequences respectively. The phase shifts however occur differently between the two types of sequences as in C sequences the phase rotates around whereas in R sequences it incrementally alternates. For R sequences only, each R cycle has a corresponding R' cycle which is the opposite sign version. An R sequence plays out as a series of concatenated R and R' cycles. In the sequence used in this paper there is an 'S' before the C in the sequence, $SC2_2^1$, this simply means that it is a super cycle where the sequence is run in reverse before running forwards again. This leads to a cycle of $C2_2^1 C2_2^{-1} = SC2_2^1$.

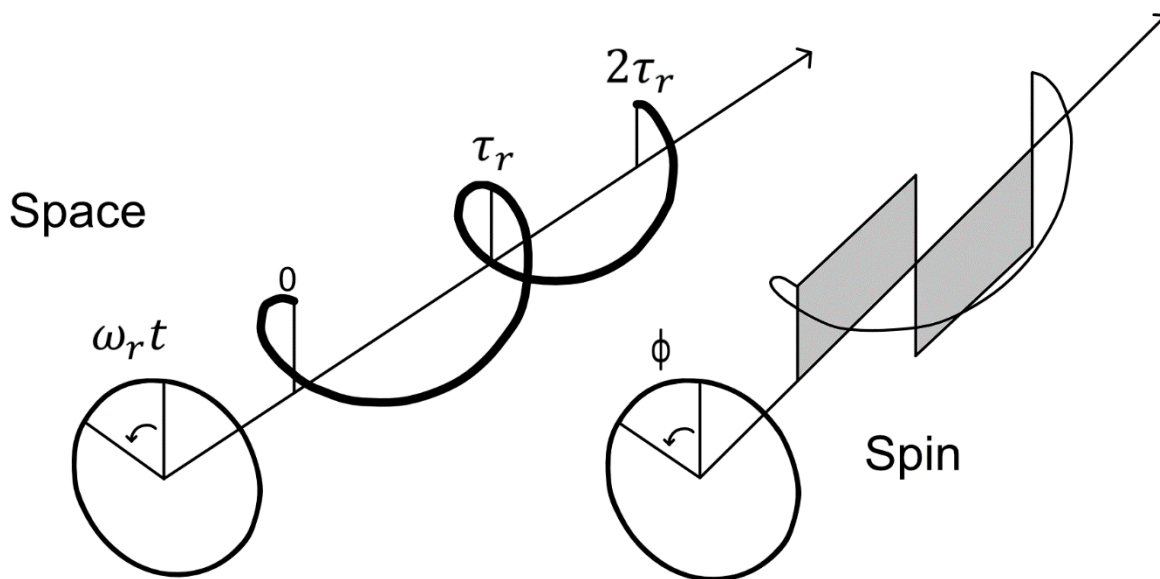


Figure 4-1, a representation of the symmetry numbers of the $C2^1$ sequence.

4.3 Selection rules

For recoupling techniques, the choice of what is recoupled, such as the CSA or dipole-dipole interaction, is based on the spin and space winding numbers of the given sequence. Selectively chosen or scaled components of one of these interactions are recoupled. The selection rules state that a component can only be recoupled if it satisfies the equation $mn - \mu\nu = ZN$, where Z is an integer. The following diagrams are visual representations of $mn - \mu\nu$ and how changing the spin and space winding numbers, n and ν , along with N allow different components to be recoupled. The 'wall,' a representation of components that are not recoupled, has a length of $N-1$ and either starts at 1 for C sequences/even rank R sequences, or starts at $-N/2$ if the rank is odd, meaning the middle of the wall passes through zero.

It is important to note that the zero component of the CSA and dipole-dipole coupling, i.e., the line that should pass through the wall at zero, is not present as this is still removed via MAS.

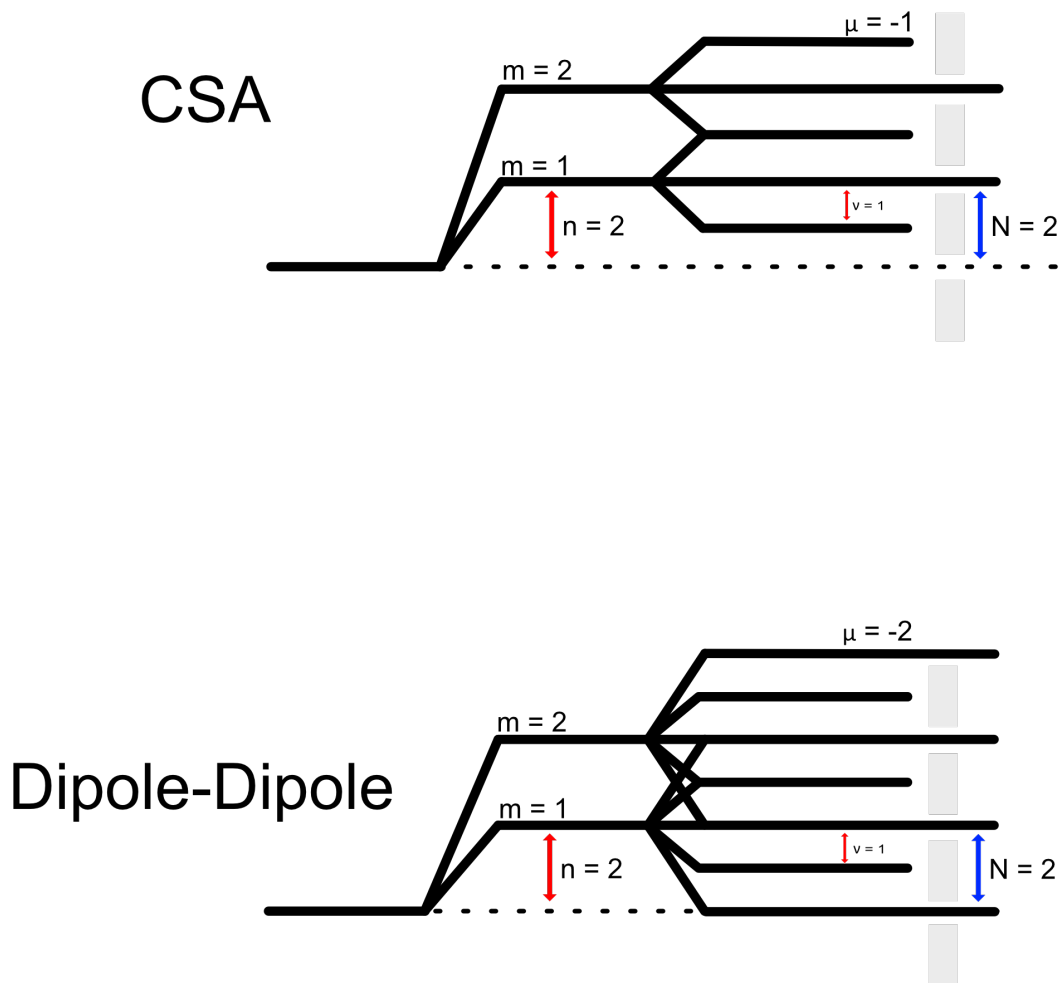


Figure 4-2, $SC2_2^1$ Spin-space selection diagram.

By checking the CSA diagram for $SC2_2^1$ using $mn-\mu\nu$ it can be seen that $(1*2) - (0*1) = 2$ and $(2*2) - (0*1) = 4$. This means that both the terms $\{l, m, \lambda, \mu\} = \{2,1,1,0\}$ and $\{2,2,1,0\}$ are symmetry allowed as both give integer multiples of N . For the dipole-dipole coupling the values allowed are $\{2,1,1,-2\}$, $\{2,1,1,0\}$, $\{2,1,1,2\}$, $\{2,2,1,2\}$, $\{2,2,1,0\}$ and $\{2,2,1,-2\}$.

The reason this is important is because the calculation of the sign of the CSA requires the reintroduction of both the $|m|=1$ and $|m|=2$ components. This poses a problem as the dipole-dipole coupling, which is also introduced, would obscure part of the CSA pattern. However, these are removed via implementation of the POST (Permutationally Offset Stabilized) sequence as described originally in 1998 for POST C7 [67,68]. It was then employed

as part of this specific sequence in 2021, the POST included pulse sequence is 90-360-540-360-90 with alternating 180 phases [69].

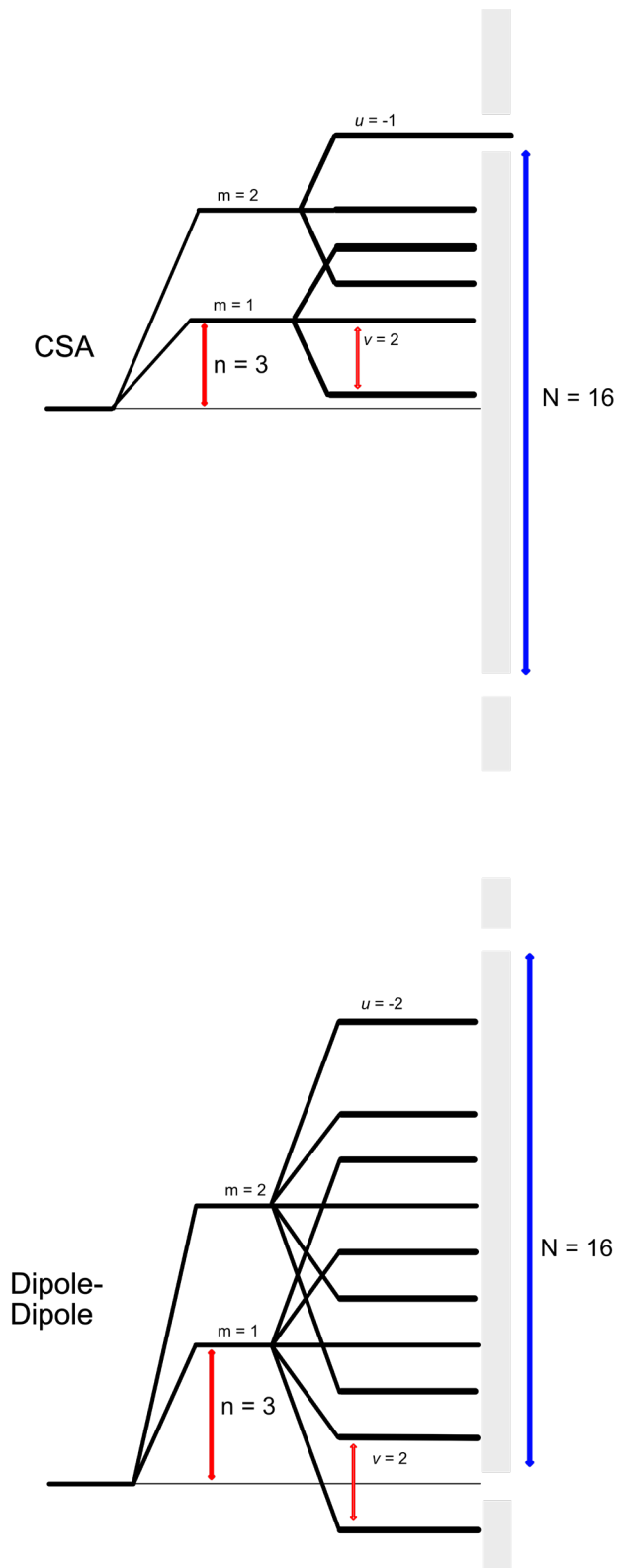


Figure 4-3, $R16_2^3$ sequence spin-space selection diagram.

The diagram above can be checked using $mn - \mu\nu$. As can be seen only one component is allowed though for the CSA, this one is the $\{2,1,1, -2\}$ and is allowed through as $(2*2) - (-2*2) = 8$ which is an integer multiple of $16/2$ and so is symmetry allowed.

For the dipole-dipole components, none are symmetry allowed as the 'wall' is too long to allow any through. Because the spin rank is even the wall does not straddle 0 and so the $\{2,0,2,0\}$ component could pass through, however as previously stated this is not present under MAS.

By checking the CSA diagram for $SC2\frac{1}{2}$ using $mn - \mu\nu$ it can be seen that $(1*2) - (0*1) = 2$ and $(2*2) - (0*1) = 4$. This means that both the terms $\{l, m, \lambda, \mu\} = \{2,1,1,0\}$ and $\{2,2,1,0\}$ are symmetry allowed as both give integer multiples of N . For the dipole-dipole coupling the values allowed are $\{2,1,1,-2\}$, $\{2,1,1,0\}$, $\{2,1,1,2\}$, $\{2,2,1,2\}$, $\{2,2,1,0\}$ and $\{2,2,1,-2\}$.

Chapter 5: Experimental

Adamantane was used as a reference with the downfield carbon set to 37.85 ppm. The DNP experiments were performed on a high performance digital AVANCE III 600.13 MHz (^1H Larmor frequency) with a 385 GHz Gyrotron. The probe was a triple resonance Ascend™ wide-bore (89 mm) using 3.2 mm rotors. During experiments the probe was cooled and maintained to 100 K using cold nitrogen gas for the duration of the experiment. A MAS rate of 10 kHz was used for all carbon experiments.

The majority of proton experiments were performed on a Bruker 800 MHz NEO 5 channel instrument using a double resonance, 1.3 mm HCN probe. All experiments were carried out at room temperature.

Where stated proton experiments were also carried out at the UK High-Field Solid-State NMR Facility using their 1 GHz standard-bore magnet, using 0.7 mm rotor. All experiments were carried out at room temperature.

The naloxone HCl di-hydrate and freebase anhydrous used in this work was obtained from Johnson Matthey. The freebase monohydrate form was synthesized from the HCl di-hydrate form as per the method used in the paper analysing naloxone by R. de Gelder [70]. The crystal structures were obtained directly from Dr. Gelder, with the exception of the HCl di-hydrate form which was acquired from the CCDC under Deposition number 1216411 [70]. For DNP sample preparation the radical mixture, either TEKPol in TCE or AMUPol in glycerol:D₂O:H₂O(60:30:10) or AMUPol in D₂O:H₂O(90:10), was added to the powder sample in 1-5 μl increments until the desired consistency, a visual resemblance to wet sand, was obtained.

Pantheon was written in MATLAB, version R2023a, available from MATLAB Inc [71]. The add-ons used were: Communications Toolbox version 8.0, curve Fitting Toolbox version 3.9, DSP System Toolbox version 9.16, Industrial Communication Toolbox version 6.2, MATLAB Coder version 5.6, MATLAB Compiler version 8.6, Natural-Order Filename Sort version 3.3.0, Signal Processing Toolbox version 9.2, Simulink version 10.7, Symbolic Math Toolbox version 9.3, WLAN Toolbox version 3.6. The SIMPSON version used 4.2.1, available at [72].

5.1 DNP experiments

Across all DNP experiments a temperature of the sample was 100 K was used. The CP program was a Bruker standard pulse program. The RI pulse program is graphically shown below with the written pulse program added in appendix 4.

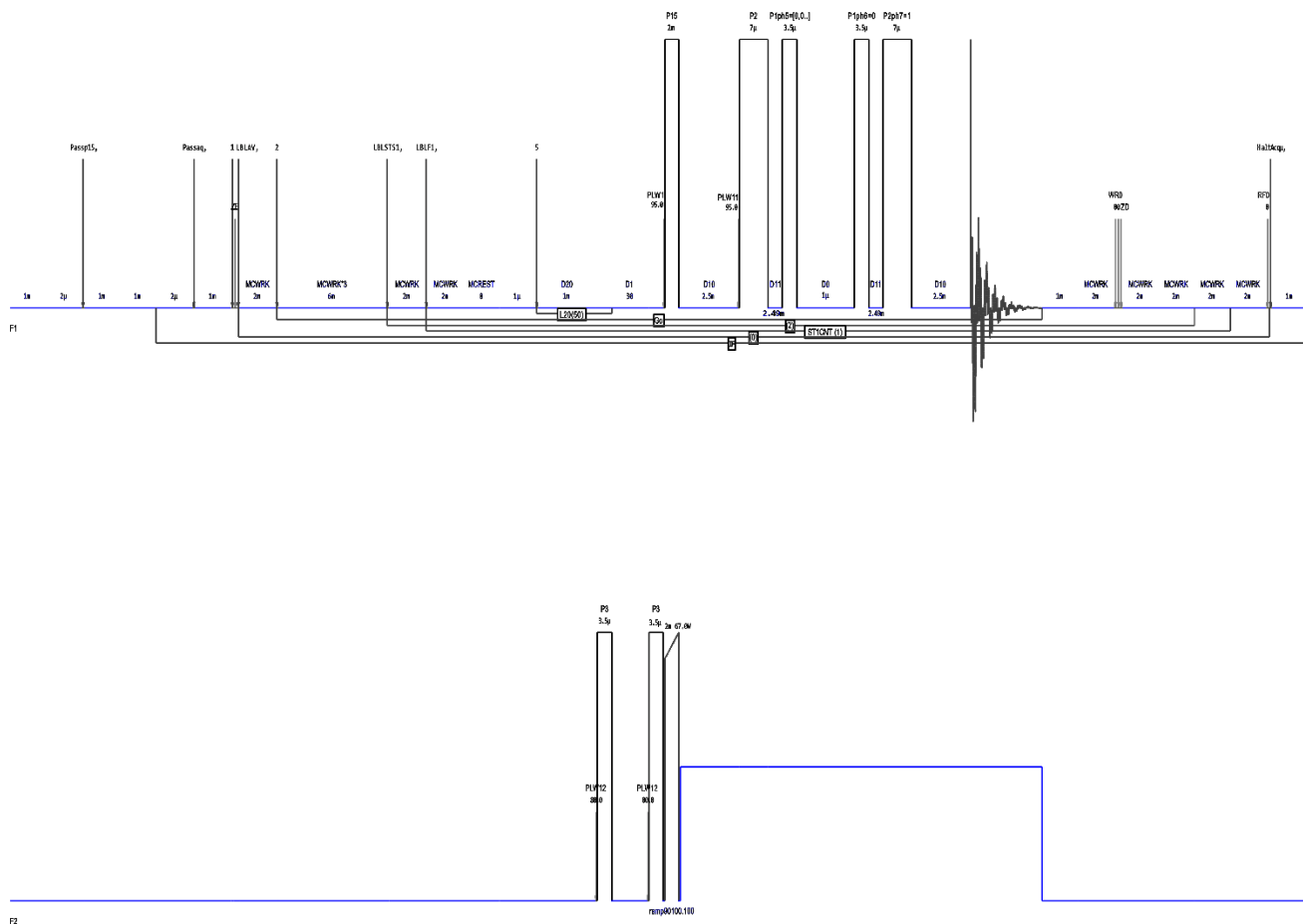


Figure 5-1 Graphical representation of the Refocused INADEQUATE (RI) pulse program.

5.1.1 Naloxone HCl di-hydrate RI

The parameters used for naloxone HCl di-hydrate RI experiment are listed here. For all experiments data were acquired with a spectral width of 424.6 and 301.1 ppm. Data was collected in 2048 points in t2 and summed from 16 scans for all 180 points in t1. Acquisition times of 0.0014 and 0.0225 s were recorded in t1 and t2. An initial relaxation delay of 15 s was calculated from a saturation recovery experiment. Contact time was calibrated and a value of 2 ms gave optimal signal intensity. The 90° pulses were calibrated by varying the pulse time at a fixed power of -18.45 dBW and selecting the maximum, leading to a 4 µs pulse

length. A mixing time of 500 ns was used. States-TPPI was used for quadrature detection. A sine square function with a sine bell shift of 2 was used for a window function in the t1 domain and an exponential function with 100 Hz broadening was used in t2.

5.1.2 Naloxone Freebase Monohydrate RI

The parameters used for naloxone freebase monohydrate RI experiment are listed here. For all experiments data were acquired with a spectral width of 424.7 and 262.9 ppm. Data was collected in 2048 points in t2 and summed from 16 scans for all 128 points in t1. Acquisition times of 0.001 and 0.026 s were recorded in t1 and t2. An initial relaxation delay of 30 s was calculated from a saturation recovery experiment. Contact time was calibrated and a value of 2 ms gave optimal signal intensity. The 90° pulses were calibrated by varying the pulse time at a fixed power of -19.03 dBW and selecting the maximum, leading to a 3.5 μs pulse length. A mixing time of 1 μs was used. States-TPPI was used for quadrature detection. No window functions were needed in the processing of this form.

5.1.3 Naloxone Freebase Anhydrous RI

The parameters used for naloxone freebase anhydrous RI experiment are listed here. For all experiments data were acquired with a spectral width of 397.6 and 276.1 ppm. Data was collected in 2048 points in t2 and summed from 512 scans for all 86 points in t1. Acquisition times 0.001 and 0.025 s were recorded in t1 and t2. An initial relaxation delay of 3.8 s was calculated from a saturation recovery experiment. Contact time was calibrated and a value of 2 ms gave optimal signal intensity. The 90° pulses were calibrated by varying the pulse time at a fixed power of -22.44 dBW and selecting the maximum, leading to a 3.6 μs pulse length.

A mixing time of 1 μs was used. States-TPPI was used for quadrature detection. An exponential function with 20 Hz broadening was used in both t_1 and t_2 .

5.1.4 Naloxone CP experiments

For the CP experiments performed on the DNP prepped samples the settings largely uniform across the samples. A spectral width of 301.2 ppm. 2048 points were collected in 4 scans. Acquisition times were ~ 0.023 s with minor variations between forms. The D_1 's were the same as per the RI. Contact time was calibrated and a value of 2 ms gave optimal signal intensity. The 90° pulse length was the same as was used in the RI. No window functions were needed in the processing of this form.

For the non-DNP prepped samples, i.e. the raw powder samples these were performed with an initial relaxation delay of 100 s. This is because these were also run on the same DNP instrument as the prepped ones and so were cooled to 100 K. This low temperature caused the relaxation times to increase from the 30 s range to over 100 s. These experiments were also increased to 8 scans due to the lack of enhancement provided by the radical.

5.2 CSA based recoupling experiments.

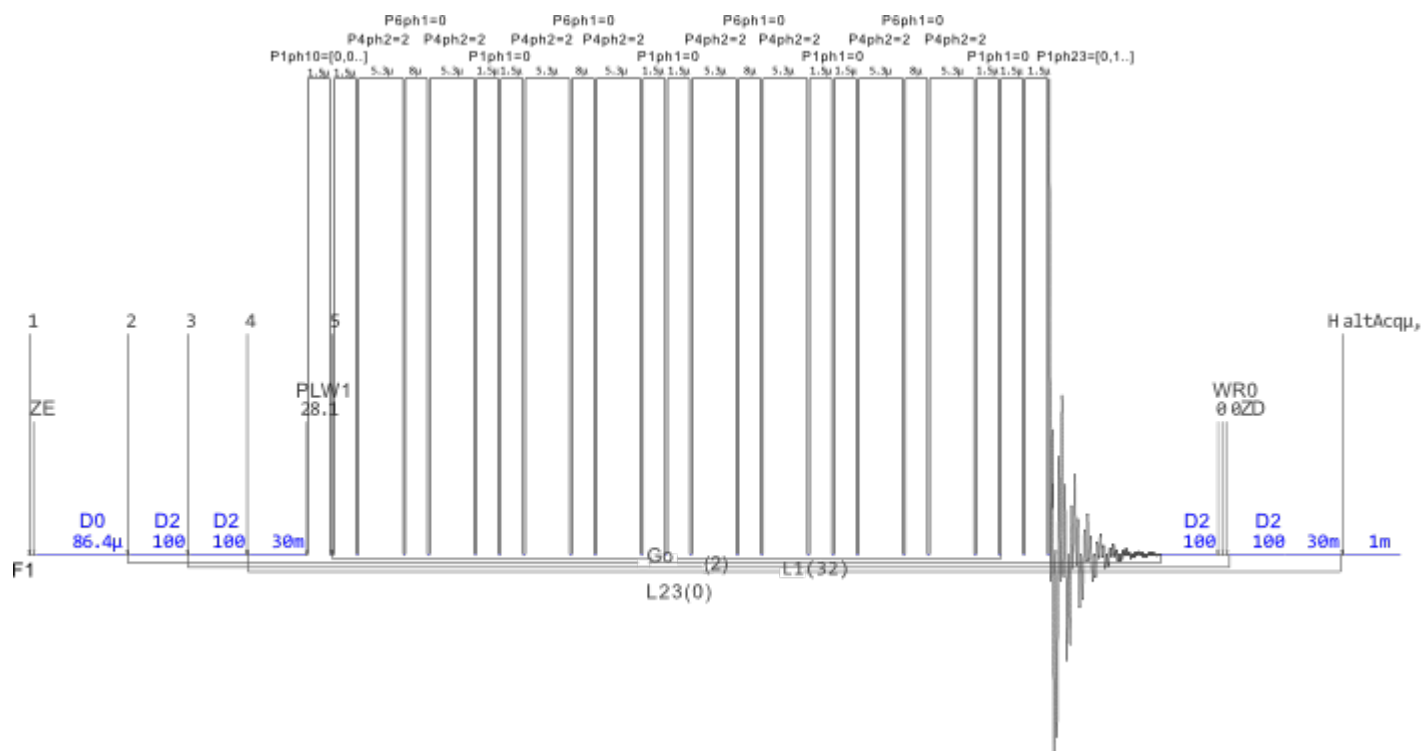


Figure 5-2 Pulse program for the SC212 experiment. The written program can be found in Appendix 5.

These experiments were obtained on two different instruments. Due to not having access to one of the forms at the time only 2 of the 3 available forms were performed on the UK High-Field Solid-State NMR Facility.

5.2.1 800 MHz Recoupling Experiments

Due to the pulse length being linked to the spinning speed in these experiments the three forms were acquired and processed under the same conditions. For all experiments data was acquired with a spectral width of 148.75 and 9.70 ppm. Data was collected in 10240 points in t_2 and summed from 8 scans for all 64 points in t_1 . Acquisition times of 0.003 and 0.043 s were recorded in t_1 and t_2 . An initial relaxation delay of 200 s was used to obtain the highest degree of relaxation between experiments without causing unfeasible experimental times. Recoupling experiments have pulse lengths linked to the spinning speed. Because these

samples were spun at 15 kHz the 90° pulse was 1.5 μ s, the 360° was 3.2 μ s and the 540° was 7 μ s. These are not direct multiples of the 90° pulse with the reasons given in chapter 6.3 with Figure 6-28 showing the nutation curve used to obtain the values. TPPI was used for quadrature detection. A sine square function with a sine bell shift of 2 was used for a window function in the t1 domain and an exponential function with 10 Hz broadening was used in t2.

5.2.2 1 GHz Recoupling Experiments

The experiments performed at the UK High-Field Solid-State NMR Facility were on a 0.7 mm probe with higher power capacity. This meant the experiments could be performed at 100 kHz. At these speeds the 90° pulse was 1.5 μ s, the 360° was 5 μ s and the 540° was 7.5 μ s. These values were calculated by multiplying the 90°. Spectral widths of 147.00 and 12.50 ppm were used. Data was collected in 10294 points in t2 and summed from 32 scans for all 64 points in t1. Acquisition times of 0.003 and 0.035 s were recorded in t1 and t2. An initial relaxation delay of 30s was calculated from a saturation recovery experiment. Quadrature detection achieved using the States method. An exponential window function was employed only in the t2 axis with a broadening of 50 Hz.

5.2.3 1 GHz BABA and NOESY

The experiments performed at the UK High-Field Solid-State NMR Facility were on a 0.7 mm probe. For both experiments the spinning speed was set to 100 kHz MAS. The 90° pulse was 1.25 μ s. Data was collected in 10294 points in t2 and summed from 4 scans for all 392 points in t1 for the NOESY. Data was collected in 10294 points in t2 and summed from 4 scans for all 196 points in t1 for the BABA. Acquisition times of 0.002 and 0.035 s were recorded in t1 and t2 for both. An initial relaxation delay of 30s was calculated from a saturation recovery

experiment. Quadrature detection achieved using the States method. A mixing time of 1 μ s was used for the NOESY experiments. An exponential window function was employed in both axis with a broadening of 75 Hz in the NOESY. In the BABA an exponential window function was employed only in the t2 axis with a broadening of 50 Hz. The pulse programs for both are given in the appendix.

5.3 Solution NMR experiment.

While assessing for impurities solution state NMR spectra was recorded. This was performed on a Bruker 400 MHz AV(III)HD system. Fitted with a 5mm BBO prodigy nitrogen cryoprobe. For sample preparation 40 mg of naloxone freebase anhydrous was dissolved in 0.6 mL of DMSO. The experiment performed was a Bruker standard zg30. Data was acquired across 65536 points from 16 scans. A spectral width of 20.55 ppm was used and a 30° pulse of 3.41 μ s. An exponential window function was employed with a broadening of 0.3 Hz.

Chapter 6: Naloxone

The main compound of this work is naloxone. Naloxone is a drug from the opioid family, sharing the majority of its chemical structure with morphine and heroin. Opium is dried latex contained in the seed capsules of the opium poppy plant. Morphine, among other alkaloids, can be found in this raw opium where it can either be extracted and used in the production of pharmaceutical products or can be prepared into 'morphine base,' which is more easily illegally smuggled [73].

Naloxone is derived from oxymorphone, an opioid analgesic [74]. Unlike morphine or heroin, naloxone is used to treat opioid depression and acute overdose [75]. In recent years the use of naloxone has increased dramatically due to the opioid crisis in America.

Naloxone can be taken into the body in three ways: intravenously, intramuscular/subcutaneously and through a nasal spray. While intravenous may have fastest onset, it may also be difficult to gain venous access in patients who perform self-intravenous injections regularly. There is a push to make easy to use treatment options and provide training for law enforcement individuals and people who are related to people at risk of an overdose. The development of reliable nasal formulations will allow for an even lower level of training and so a higher coverage of at-risk individuals. Though this requires further optimisation into the dosage and forms of naloxone used to be able to give the same result as intravenously [76].

Naloxone is found in four basic solvate forms, the free base naloxone is found in both mono- and anhydrous forms, and the hydrochloride form in both anhydrous and dihydrate forms. The hydrochloride forms are often the most used for opioid overdose treatment due to its

bioavailability. In Figure 6-1 the naloxone structure is shown. It has a 3D 'T' shape, which is present in all opioid compounds. This 'T' shape comes from the central elevated ring system.

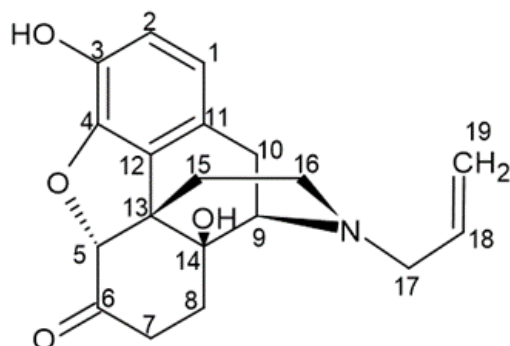


Figure 6-1, Chemical structure of naloxone with carbon positions numbered.

Naloxone poses an interesting question in NMR as to if it is possible to distinguish between different solvates of the same compound. This was investigated in three stages, investigation into the ^{13}C spectra, the ^1H spectra and finally the hydrogen CSA values of naloxone. The Crystal structures of naloxone are seen below in Figure 6-2 and are adapted from [70]. These were obtained using a Bruker AXS D8 Advance X-ray diffractometer and diffraction patterns were indexed using DICVOL91 and FIDDLE. Further details can be found in the paper.

Naloxone was chosen as the model compound as it was easily available and sees real world use. From a chemical perspective it was chosen due to its relative complexity in regards to the number of carbons while also having multiple hydrate forms. Naloxone itself has already been widely analysed due to its above mentioned uses but analysis into it can be used to show how the techniques described in this work can be used on compounds that are less understood.

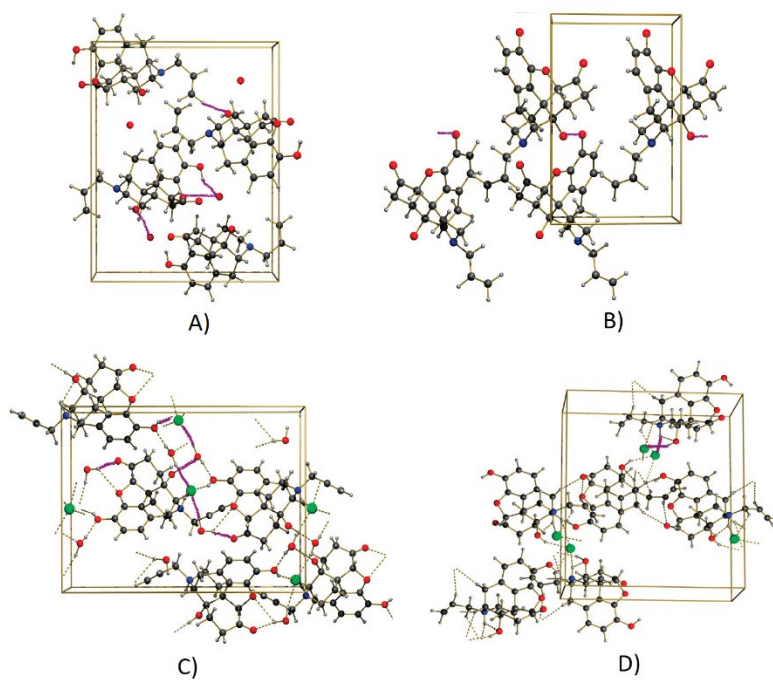


Figure 6-2, The crystal structures of naloxone: a) mono hydrate, b) anhydrous, c) hydrochloride di-hydrate, d) hydrochloride anhydrous. [70]. The purple lines indicate hydrogen bonds.

6.1 ¹³C analysis.

When beginning the analysis of naloxone, Cross-Polarisation (CP) ¹³C MAS spectra were measured. This was to see if the different packing of the forms would have any effect on the ¹³C spectra.

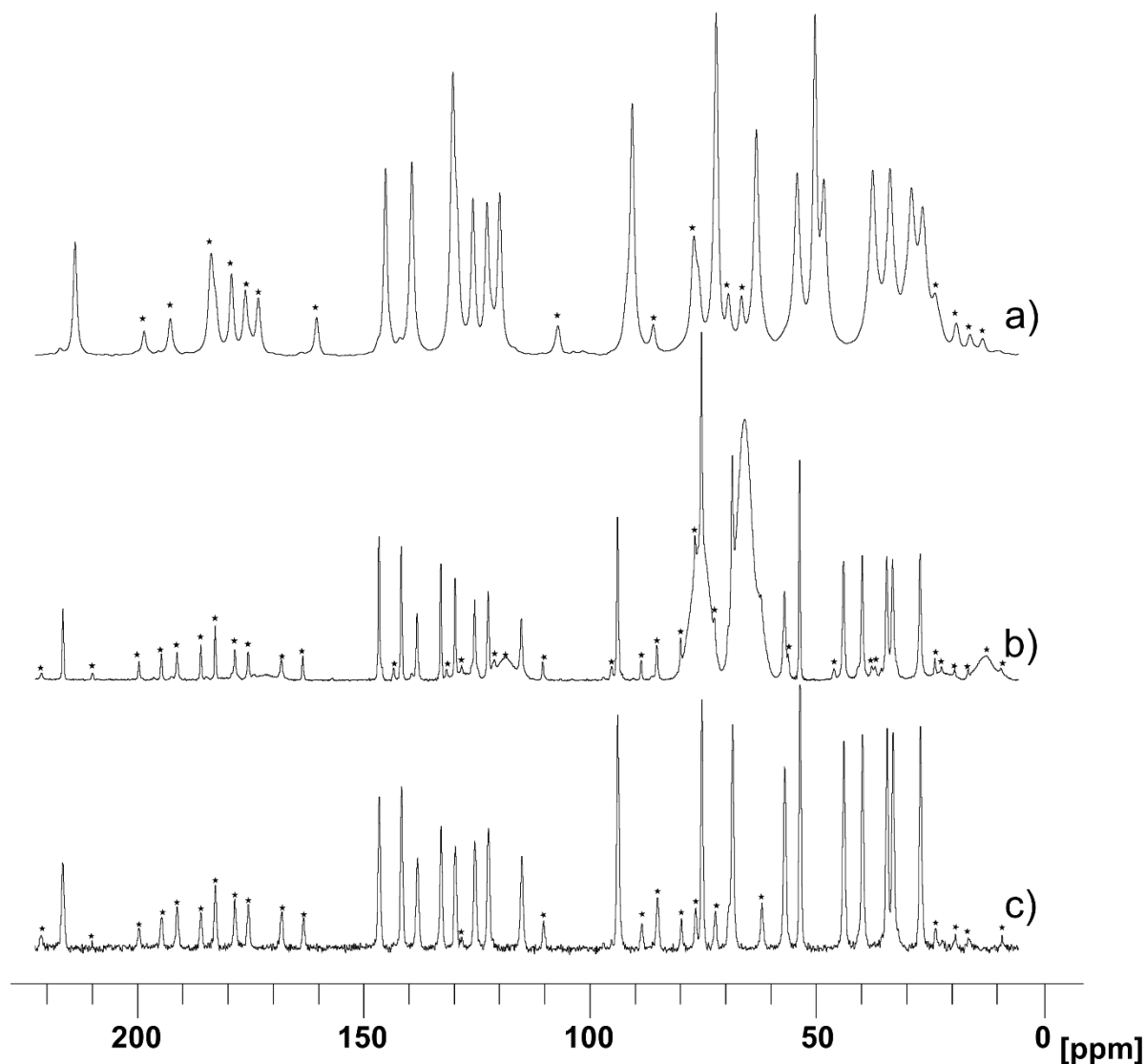


Figure 6-3. The DNP-enhanced ^{13}C CP-MAS-MAS NMR spectra for the three naloxone forms that were available. Naloxone: a) HCl dihydrate in 15 μl of 17 mM TEKPol/TCE with 40 mg of sample, b) Freebase monohydrate in 30 μl of 20 mM AMUPol in glycerol: D_2O : H_2O (60:30:10) with 40 mg of sample, c) Freebase anhydrous in 30 μl of 20 mM AMUPol in D_2O : H_2O (90:10) with 40 mg of sample. Each was recorded on a 600.13 MHz magnet for 8 scans with a contact time of 2000 μs . The ★ signifies a spinning sideband.

While in the above figure it is clear to see that there is some visual difference between the spectra, the groupings of the peaks are generally similar. The next step in the analysis was to try assign the ^{13}C peaks. To do this a refocused INADEQUATE (RI) experiment was chosen, the pulse sequence can be seen below in Figure 6-4. This sequence produces a 2D spectrum that shows direct through bond connections between carbons, i.e. carbons that are chemically

bonded to one another. This, in theory, would allow for all peaks to be assigned. While this is a powerful analytical tool it suffers from the problem of requiring two ^{13}C nuclei to be adjacent to each other. This occurs once in every 10000 due to the low natural abundance of the ^{13}C isotope. Because of this it is impractical to perform this under standard conditions since it would take multiple weeks to months. This means that either the use of isotopically labelled compounds or signal boosting methods such as DNP must be deployed. In this case the latter was chosen.

Across the three forms there was varied levels of enhancement provided by DNP. For the freebase monohydrate form an enhancement of ~ 13 was observed, ~ 26 for HCl di-hydrate and ~ 8 for freebase anhydrous. The enhancement varies across the three forms based on different radicals being implemented as well as differing levels of solubility. The three forms had measured T1 relaxation times of 1.3 – 3.5s. The D1 was universally set to 10 seconds for all carbon experiments to all for consistency across the forms.

As previously stated in its corresponding theory section, DNP provides an increase to the signal generated by use of a radical impregnated into the sample which is 'activated' by microwave irradiation. This allows for the experiment to be completed in much more practical time periods.

DNP enhancement allows for the assigning the peaks, of a standard ^{13}C experiment, via the RI experiment. This experiment allows the observation of through bond, ^{13}C - ^{13}C connections, to make an assignment of the peaks. This leads to correlations forming between directly coupled carbons.

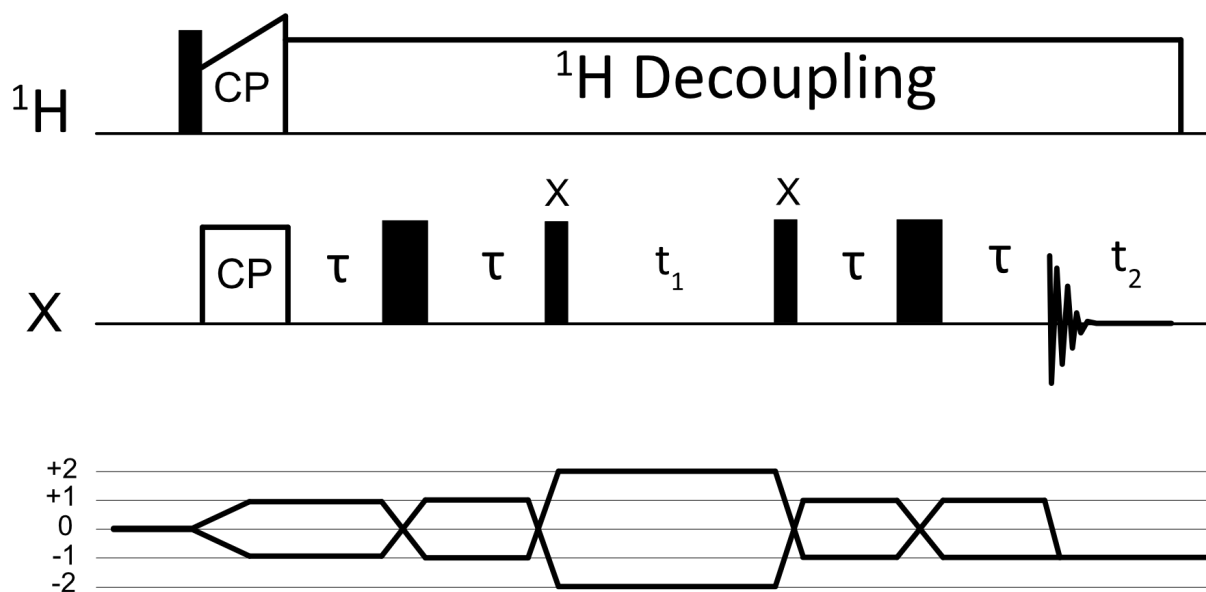


Figure 6-4, the pulse sequence and coherence transfer pathway of the refocused INADEQUATE experiment.

The refocused INADEQUATE experiment uses cross polarization to initially create transverse magnetisation. The τ - π - τ sequence generates, through J-coupling, anti-phase coherences. These are then transformed to double quantum and zero quantum coherences by the first 90° pulse. These then evolve under t_1 where appropriate phase cycling allows for the removal of the zero quantum coherences. The remaining coherences evolve under the sum of the two chemical shifts and are then converted back to anti-phase coherences and then in-phase coherences for detection [29].

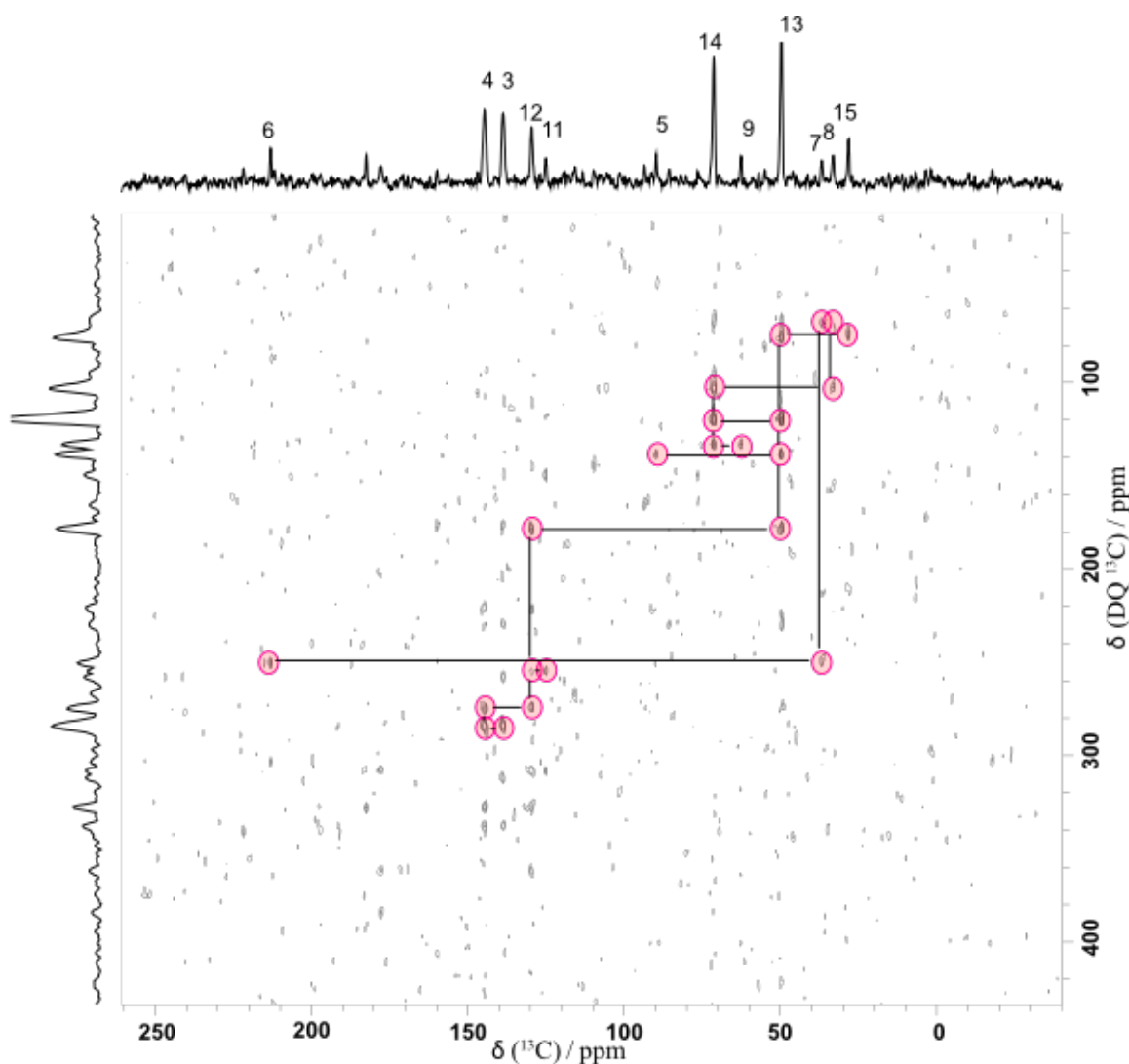


Figure 6-5, A DNP-enhanced ^{13}C ^{13}C refocused-INADEQUATE spectrum for naloxone HCl dihydrate doped with 15 mM TEKPol in 17 μl of TCE. The experiment was performed on a 600.13 MHz magnet with a spinning speed of 8.0 kHz. The spectrum was acquired in 16 scans with each being made up of 180 increments in t_1 . These increments spanned 15.6 μs giving a spectral width in f_1 of 64 kHz. The contact time was 2000 μs .

When beginning the assignment of a RI spectrum a starting point is required. In the case of naloxone, carbon 6 was chosen. It can be estimated that this carbon will have the highest ppm value based on its proximity to oxygen, and if this incorrect then it will quickly become apparent. Each correlation relates to a real carbon-carbon connection. As can be observed carbon 6 has a single correlation. The carbon it is connected to has one other correlation. The

same occurs again for the next one until 4th carbon is reached in this chain, that being carbon 14. By following this line of logic, it was possible to assign all viable peaks, this being carbons 3,4,5,6,7,8,9,11,12,13,14 and 15. The remaining peaks did not show up which leaves 6 peaks unassigned. Some of these peaks however do show up in the 1D CP and using CASTEP data a near total assignment can be made. Another thing to notice is the cluster of peaks underneath the ones used to assign carbons 3, 4, 12 and 11. These arise from spinning side bands in the indirect dimension. This shows how assignment can be difficult and a way to confirm the assignment is key.

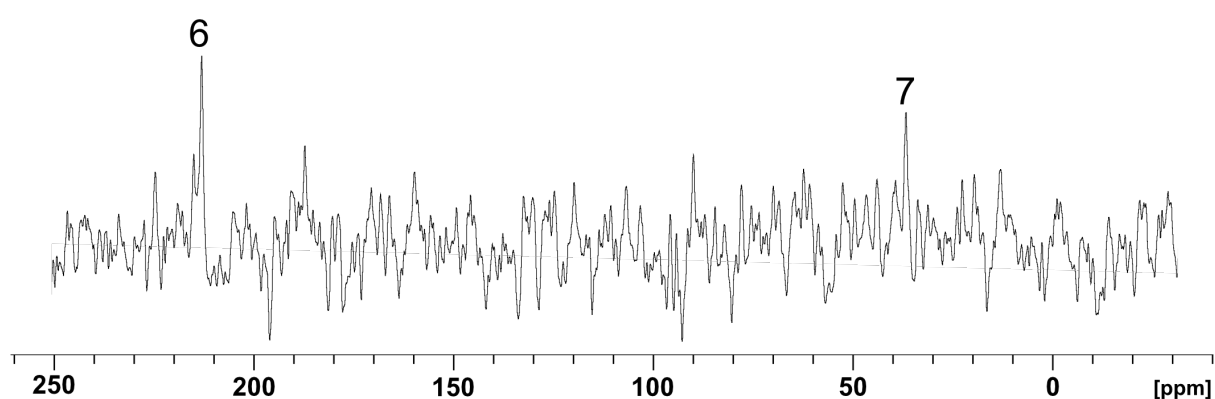


Figure 6-6, 1D carbon cross section of naloxone HCl di-hydrate in 15 ul of 17 mM TEKPol/TCE with 40 mg of sample from the spectra in figure Figure 6-5 at row 221, corresponding to 251 ppm on the F1 dimension. Recorded on a 600.13 MHz magnet for 8 scans with a contact time of 2000 μ s.

The above figure shows the correlation of the carbon 6 and 7. As can be seen there is a low signal to noise from this correlation, ~ 3 for carbon 6 and ~ 2 for carbon 7. This further illustrates what was already apparent in the full RI, that the SnR of the spectra is not ideal for assigning correlations.

Correlations can be 'confirmed' by summing the two peaks in the f2 axis, this value should then equal the location of the correlation in the f1 axis. This is because of the nature of the pulse program and how the double quantum coherences evolve. This means every peak can

be confirmed. This also aids in the initial discovery of the correlations as for one to be valid it must be evenly distributed either side of a line with the equation of $f1=2*f2$.

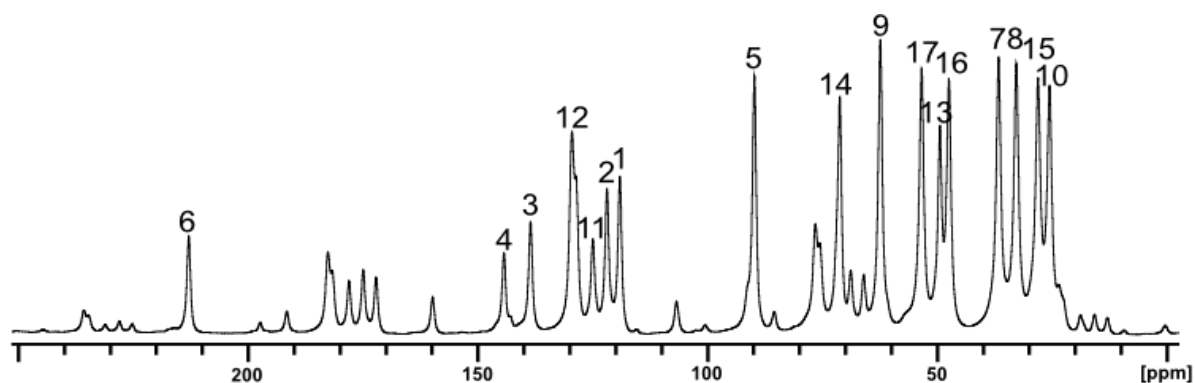


Figure 6-7, DNP enhanced 1D carbon CP of naloxone HCl di-hydrate in 15 ul of 17 mM TEKPol/TCE with 40 mg of sample with assignments made. Recorded on a 600.13 MHz magnet for 8 scans with a contact time of 2000 μ s.

As can be seen in Figure 6-7 above, peaks 1,2,10,16 and 17 can also be assigned, using CASTEP and the other solvate forms, leaving only 18 and 19 unaccounted for. One of these two can be seen as a shoulder on carbon 12 but due to the CASTEP calculations showing 18 and 19 to be so close together it is difficult to difficult say which carbon that peak is from. These two carbons can be seen in the literature at \sim 130 ppm there are three peaks but due to having insufficient resolution they have merged [70].

Below is the RI of the next form, freebase monohydrate. As can be seen there is a general similarity between this and the previously discussed HCl di-hydrate as expected. The interest in the spectra comes from the fact that carbons 15 and 8 have seemingly swapped their positions, while carbon 7 does not show in the RI, it does show in the 1D, seen in Figure 6-8.

Another point of interest is the appearance of a correlation previously not seen. This is between carbon 3 and seemingly open space. At the F2 ppm of the correlation, there is a peak at that location in the 1D carbon spectrum. Based on the structure of naloxone it is then possible to identify this as carbon 2.

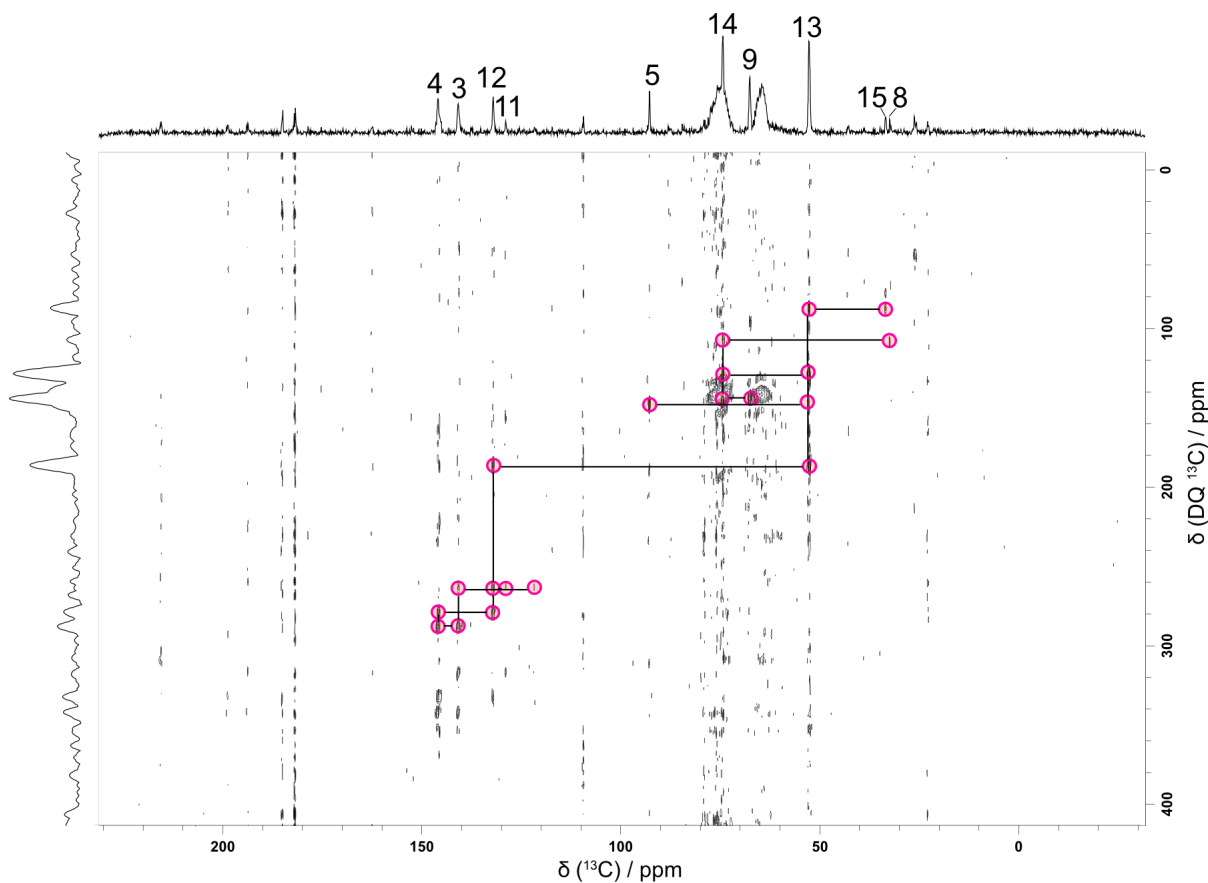


Figure 6-8, A DNP-enhanced ^{13}C ^{13}C refocused-INADEQUATE spectrum for naloxone freebase monohydrate doped in 30 μl of 20 mM AMUPol in glycerol: D_2O : H_2O (60:30:10) with 40 mg of sample. The experiment was performed on a 600.13 MHz magnet with a spinning speed of 8.0 kHz. The spectrum was acquired in 16 scans with each being made up of 180 increments in t_1 . These increments spanned 15.6 μs giving a spectral width in f_1 of 64 kHz. The contact time was 2000 μs .

The freebase monohydrate was originally run in TEKPol/TCE as this solvate form also did not dissolve completely in this preparation. It was swapped to a 60:30:10 volume mixture of glycerol, D_2O and H_2O , also known as DNP-juice, for this refocused INADEQUATE as well as the following ^{13}C spectra. This caused a shift in the ppm values which will be discussed in the solvate identity section.

One thing to note about the above RI is the greater abundance of T1 noise in this spectrum, this appears as streaks coming down the F_1 axis. The other notable factor in analysing this

form is the presence of solvent peaks. It can be seen in the RI as well as in Figure 6-9 below there are two broad peaks at 55 and 75 ppm. These two peaks both come from the glycerol used in the sample preparation.

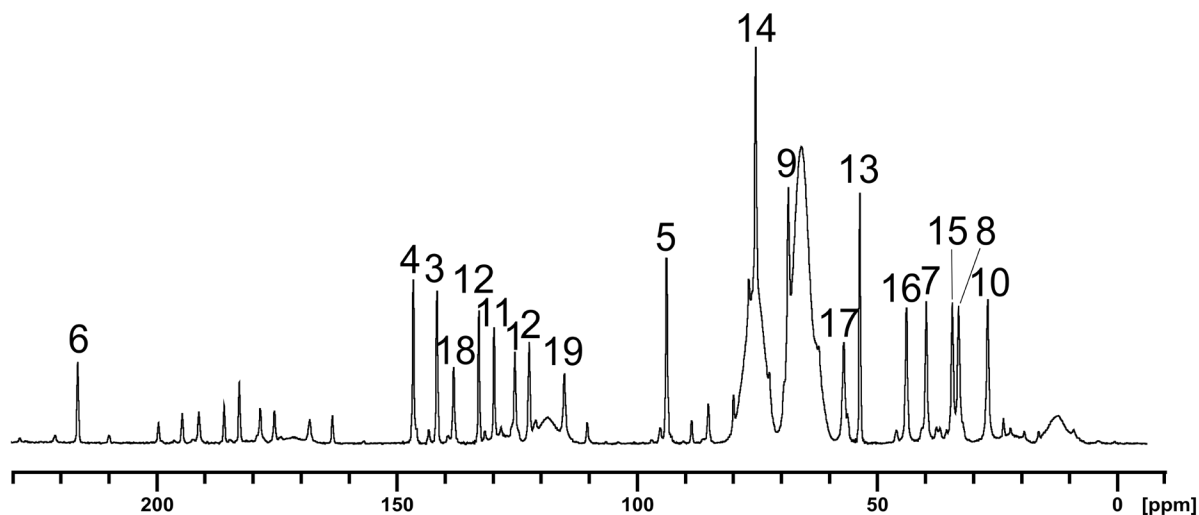


Figure 6-9, DNP enhanced 1D carbon CP of naloxone freebase monohydrate in 30 ul of 20 mM AMUPol in glycerol: D₂O:H₂O (60:30:10) with 40 mg of sample. Recorded on a 600.13 MHz magnet for 8 scans with a contact time of 2000 μs.

When looking at the 1D ¹³C of the freebase monohydrate it is possible to see and, using the assistance of CASTEP, to assign all nineteen carbons to their peaks. Carbons 16-19 consistently do not show up on RI experiments so are only assigned using CASTEP up to this point.

With the final form, naloxone freebase anhydrous, we can again see even more new correlations. As seen below in Figure 6-10 this spectrum has far less noise allowing for more correlations too be seen, this comes from the higher number of scans that were performed.

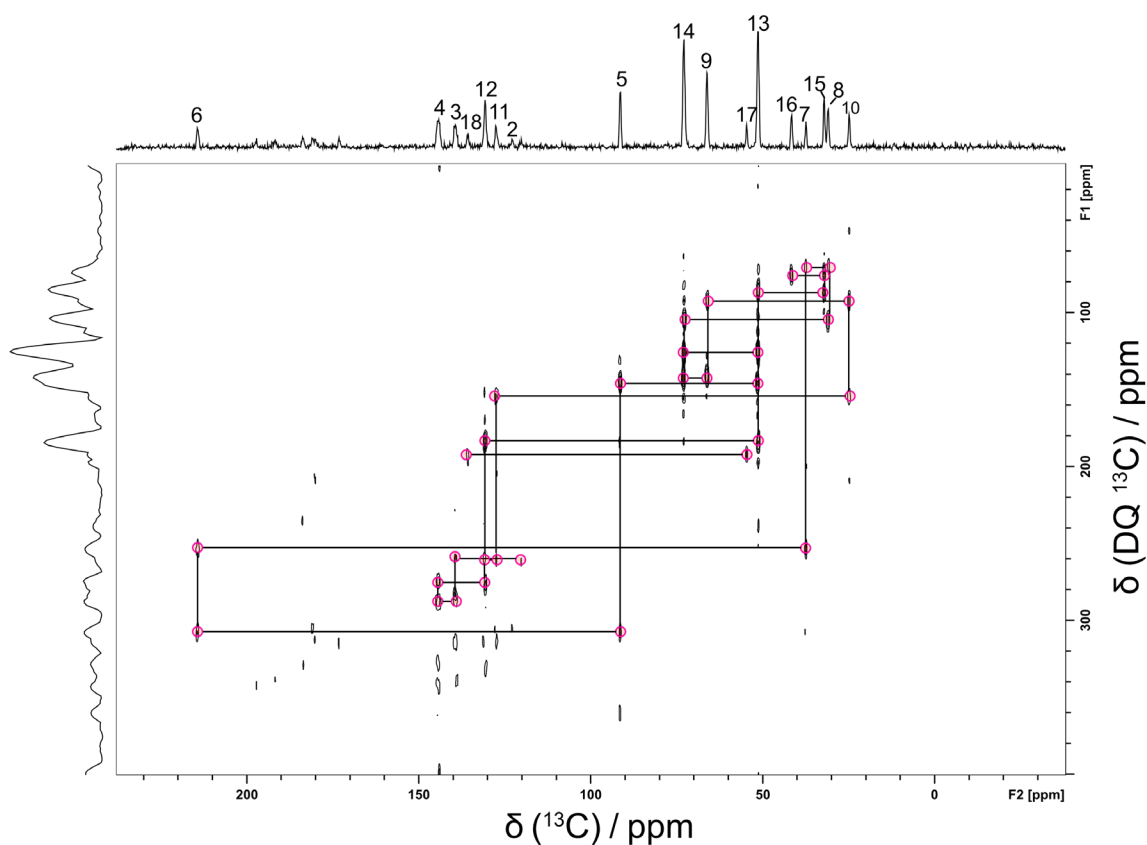


Figure 6-10 A DNP-enhanced ^{13}C ^{13}C refocused-INADEQUATE spectrum for naloxone freebase anhydrous doped in 30 μl of 20 mM AMUPol in $\text{D}_2\text{O}:\text{H}_2\text{O}(90:10)$ with 40 mg of sample. The experiment was performed on a 600.13 MHz magnet with a spinning speed of 8.0 kHz. The spectrum was acquired in 512 scans with each being made up of 86 increments in t_1 . These increments spanned 16.67 μs giving a spectral width in f_1 of 60 kHz. The contact time was 2000 μs .

As can be seen in Figure 6-10 above there are three unique correlations not seen in the other forms. The first of these is the correlation from carbon 6 to 5. This is one that has previously been missing but in this spectrum is present. The second new peak is the correlation between carbons 17 and 18. Previously these peaks did not show up along F2 and so any attempt to view correlations was impossible. With these showing up this allows for the confirmation of the assignment of 17, 18 and 19 in the 1D ^{13}C spectra in previous forms. The final new peak is

the correlation that connects to carbon 16. This has its correlation from carbon 15 visible in this form, again another correlation that is not seen in previous experiments. This allows for carbons 1-18 to be assigned using the RI experiment.

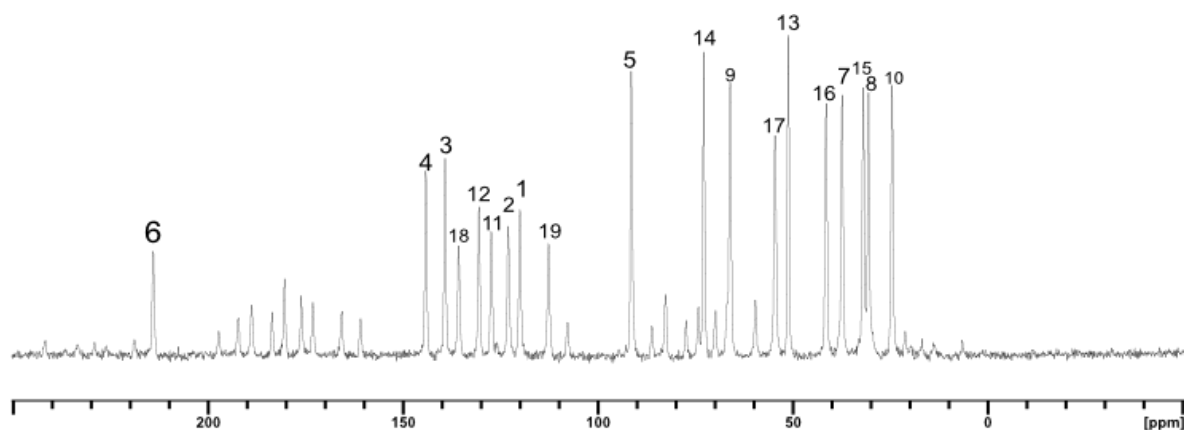


Figure 6-11, DNP enhanced 1D carbon CP of naloxone freebase anhydrous in 30 μ l of 20 mM AMUPol in $D_2O:H_2O(90:10)$ with 40 mg of sample. Recorded on a 600.13 MHz magnet for 4 scans with a contact time of 2000 μ s.

In the above Figure 6-11 all carbons are assigned. By using the assignment provided by RI and assessing which peaks are the result of spinning sidebands it is possible to deduce which peak is carbon 19. This process is applied to all the other naloxone forms available, and the RI of Figure 6-11 confirmed assignments for carbons 16-19 for them.

Something that is suggested by the RI in Figure 6-10 is that with more scans the correlations that were previously 'missing' could possibly be elucidated with high number of scans. Despite the other forms not showing as many peaks in the RI as the freebase anhydrous, with all three forms being analysed the assignment of all forms was possible.

One common feature across all the RIs was a group of carbon correlations present underneath the ones used to assign carbons 3, 4, 11 and 12. These correlations are not 'real' as can be checked by the summations of the F2 values vs the F1 value but there are

persistently present across all the forms. These likely come from spinning side bands in the indirect dimension as they are exactly 8000 Hz away from their related 'real' peaks above.

When comparing the ^{13}C -carbon spectra to the crystal structures we can see some of the expected differences between the forms. The best example of this is the position of carbon 6, this carbon's -OH is involved in different hydrogen bonds across the three analysed forms.

6.2 Solvate identity.

One of the important features of DNP NMR is that while it is still a solid-state method of analysis the samples are surrounded by an anti-solvent. This leads to the possibility of the sample having its polymorphic or solvate form changed during sample preparation. In the case of the HCl di-hydrate form the ^{13}C DNP sample lines up to traditional solid-state analysis seen in literature and so analysis of the neat powder was not undertaken [70].

For the two freebase forms this is not the case. Firstly, we compare the FM form neat to the AMUPOL in glycerol: D_2O : H_2O preparation. This can be seen below in Figure 6-12.

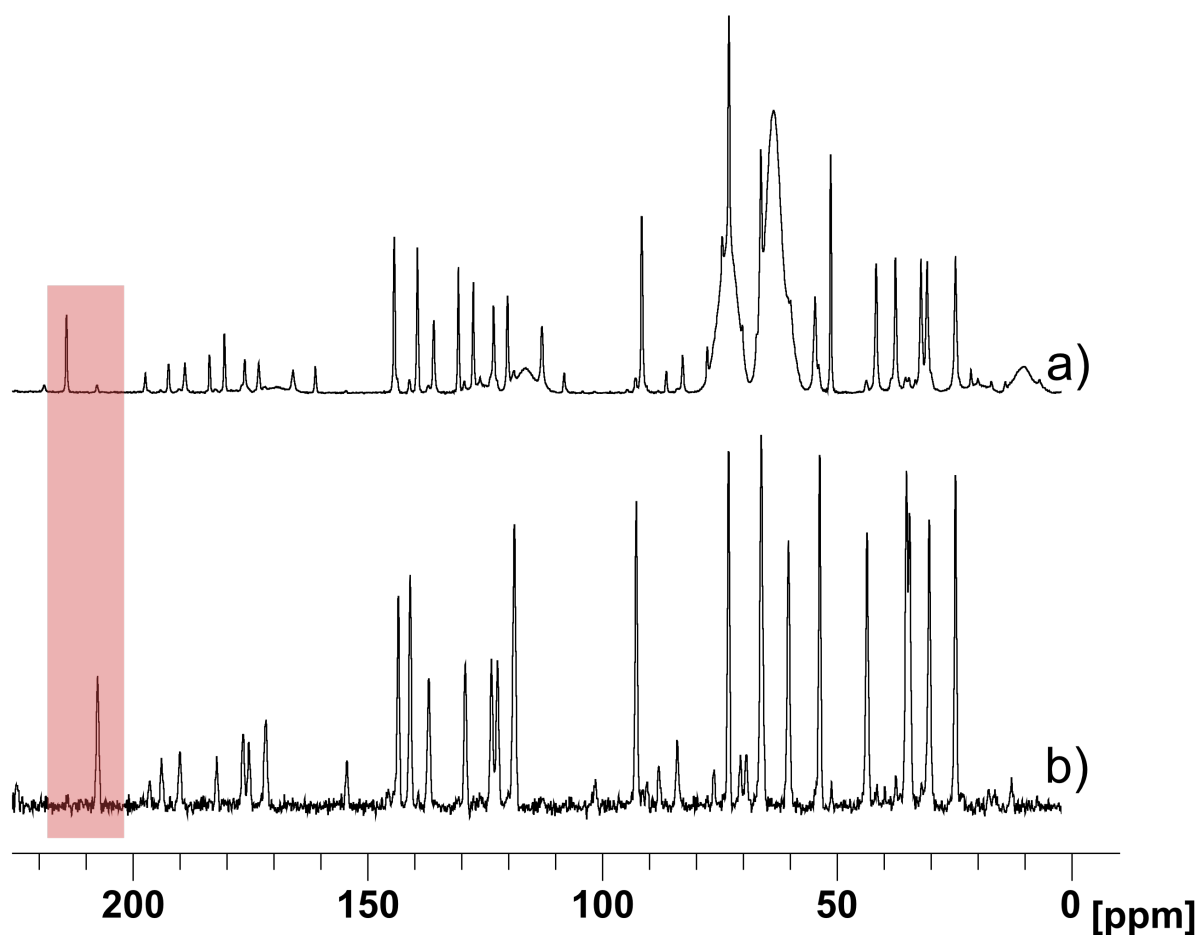


Figure 6-12, 1D carbon CP of naloxone freebase monohydrate a) in 30 μ l of 20 mM AMUPol in glycerol:D₂O:H₂O(60:30:10) with 40 mg of sample b) as the pure powder. Recorded on a 600.13 MHz magnet for 8 scans with a contact time of 2000 μ s.

When comparing the two forms in Figure 6-12 we see that there are clear differences between them. There is a shift for almost every carbon, this suggests a complete solvate or polymorphic change occurs when FM is in DNP preparation. ‘Complete’ as when in an aqueous solvent there are 19 peaks. This means that the FM form is pure in the powder form and when in DNP preparation it is completely converted to a different form. There is no mention in the literature on naloxone that suggests there are polymorphs or higher hydration forms for the freebase forms.

One thing of interest is that there is a difference in the spectrum depending on what DNP preparation is used. As already mentioned, FM was run on both AMUPOL in aqueous solvent and TEKPol TCE. When we compare the two of these in Figure 6-13 we again see a significant shift in ppm of all peaks. This suggests that the TEKPol TCE preparation of FM remains as FM and is not converted to any higher hydration forms. The choice to run the FM sample in Aqueous solvents originally was due to the literature suggesting that naloxone freebase anhydrous was insoluble in water. Based on this the FM was run in an aqueous solvent as well due to the likely similarity of solubility. The most obvious difference is the shifting of the highlighted number 6 carbon highlighted in red. As previously mentioned, this is involved in different hydrogen bonds based on what form is present and so serves as the easiest way to illustrate the forms are different.

There are changes across the whole spectra, not just the highlighted section. These other changes will be caused by different hydrogen bonds and packing. This is the case for the two carbon regions, 150-100 and 100-0 ppm. These aromatic and aliphatic regions show differences across all the solvents and could possibly be used to help illuminate packing differences. While differing hydrogen bonds will cause -OH or =O carbons to change their ppm values, as seen by the red highlighted carbon 6, the packing will cause other carbons to change. As has already been mentioned the ordering of the carbons 8 and 15, as to which one of these two is more downfield shifted, is dependent on the solvate form. The ppm shifting of these two is unlikely directly due to the forming of different hydrogen bonds as they do not have any oxygen groups, the difference in packing of the forms could be what is causing these two's positions to be changed. This idea can be carried on for all other carbons as to the cause of the shifting ppm's between the forms.

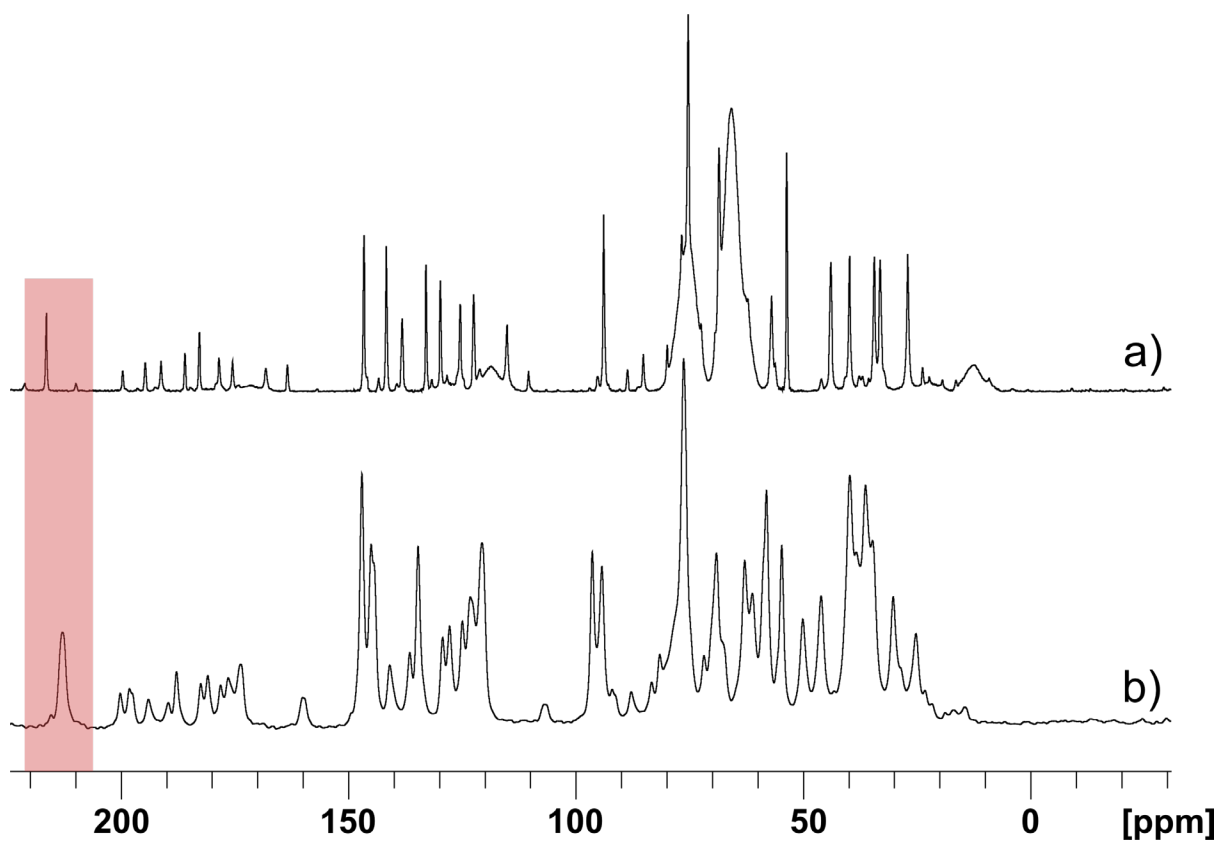


Figure 6-13, 1D carbon CP of naloxone freebase monohydrate a) in 30 μ l of 20 mM AMUPol in glycerol: D_2O : H_2O (60:30:10) with 40 mg of sample b) in 15 μ l of 20mM TEKPol/TCE with 30 mg of sample. Recorded on a 600.13 MHz magnet for 8 scans with a contact time of 2000 μ s.

When assessing the FA form, we can see a degradation of the sample. This is again highlighted in red. This can be seen below in Figure 6-14.

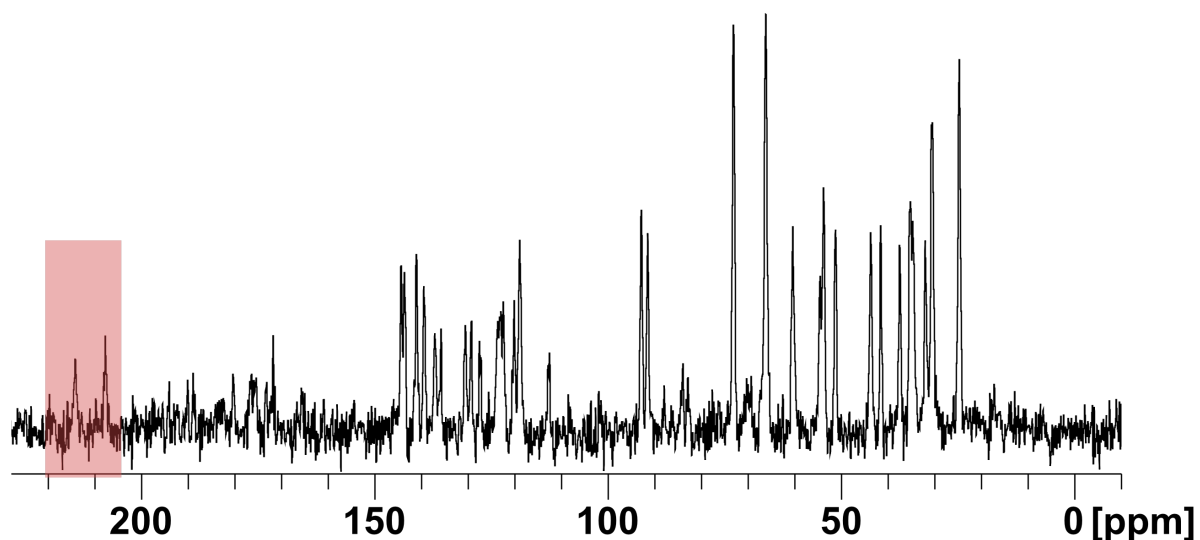


Figure 6-14, 1D carbon CP of naloxone freebase anhydrous. Recorded on a 600.13 MHz magnet for 8 scans with a contact time of 2000 μ s.

While difficult to see due to the poor resolution there are clearly more than 19 carbons in the above spectrum. There are two carbonyl peaks instead of one at 207 and 214 ppm, highlighted in red, and when counted there are over thirty total carbon peaks. This suggests that there are at least two different forms of naloxone in this sample. One consideration was an impurity but analysis by solution NMR showed only a single set of protons and no other powder was left undissolved in the tube. The solution state ^1H proton experiment below, Figure 6-15, suggests that it is indeed two forms of naloxone in this neat sample.

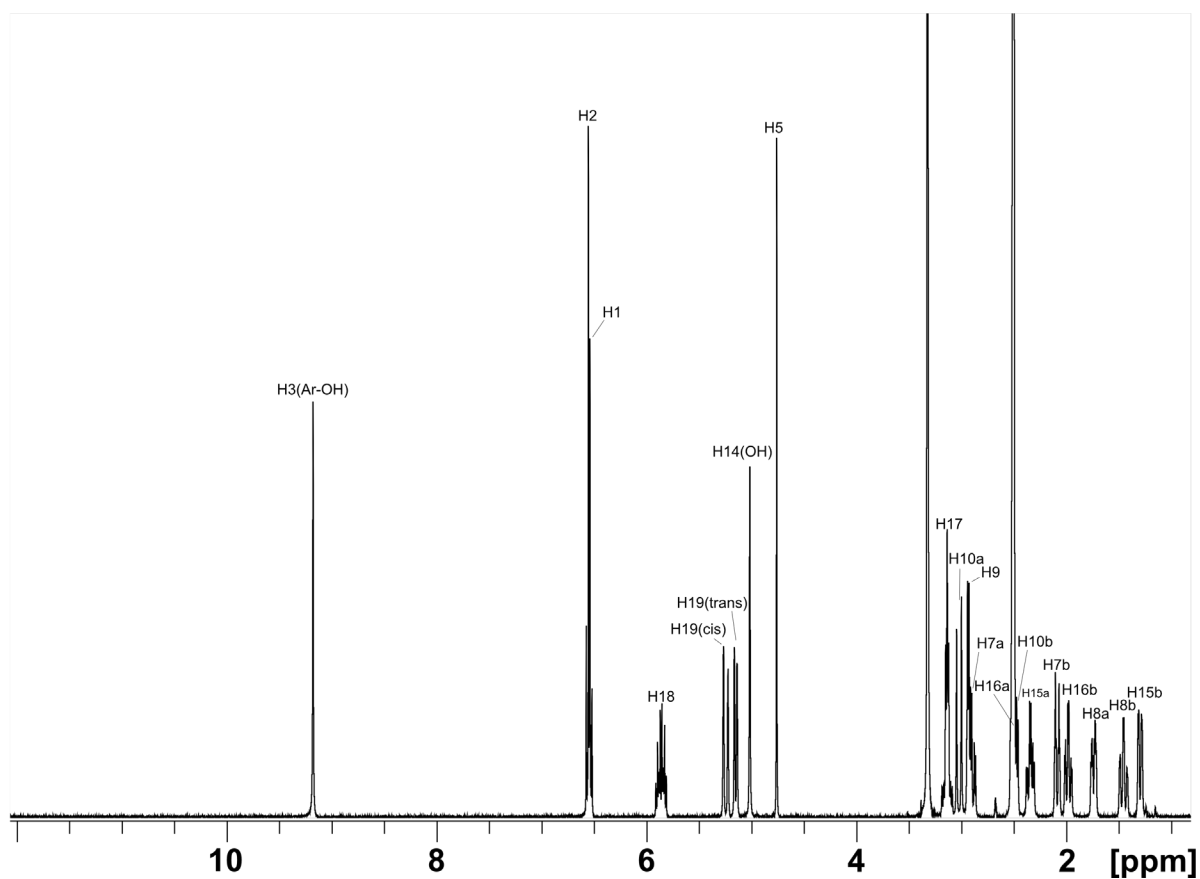


Figure 6-15, 1D proton of naloxone freebase anhydrous in DMSO. Recorded on a 600.13 MHz magnet for 16 scans across 32768 points. Performed on a Bruker 400 MHz AV(III)HD system. Fitted with a 5mm BBO prodigy nitrogen cryoprobe. The number is based on the carbon numbering in Figure 6-1. The un-labelled peaks are from the DMSO.

When we compare the DNP prep of AMUPol in D₂O:H₂O to the neat powder, in Figure 6-16 below, we can see that one of the two forms present in the neat powder converts to the other, leaving one set of 19 carbons. This is highlighted by the red and green bands. The red peak disappears leaving only the single peak at the same ppm highlighted in green.

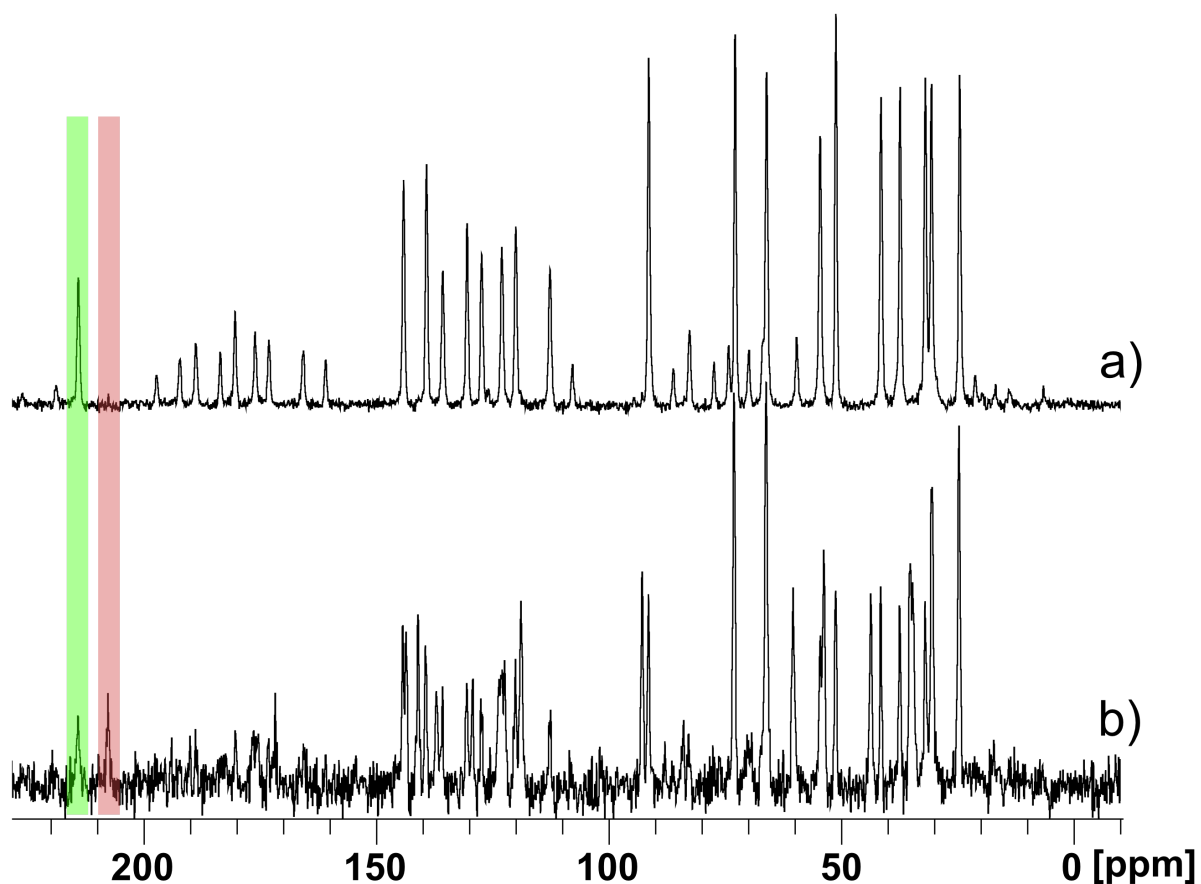


Figure 6-16, 1D carbon CP of naloxone freebase anhydrous a) in 30 ul of 20 mM AMUPol in $D_2O:H_2O(90:10)$ with 40 mg of sample and b) the neat powder. Recorded on a 600.13 MHz magnet for 4 scans with a contact time of 2000 μs .

This could be caused by a mixture of the FA form and a hydrated form, formed over time due to the moisture in the air, becoming solely this higher hydrated form when in $D_2O:H_2O$. We can see this occurring in both the FA as well as the FM forms. When both are in $D_2O:H_2O$ they convert to the same hydrated form, this is seen below in Figure 6-17. The red zone highlights that one of the peaks in the neat powder is lines up with the AMUPOL prep sample while the other doesn't.

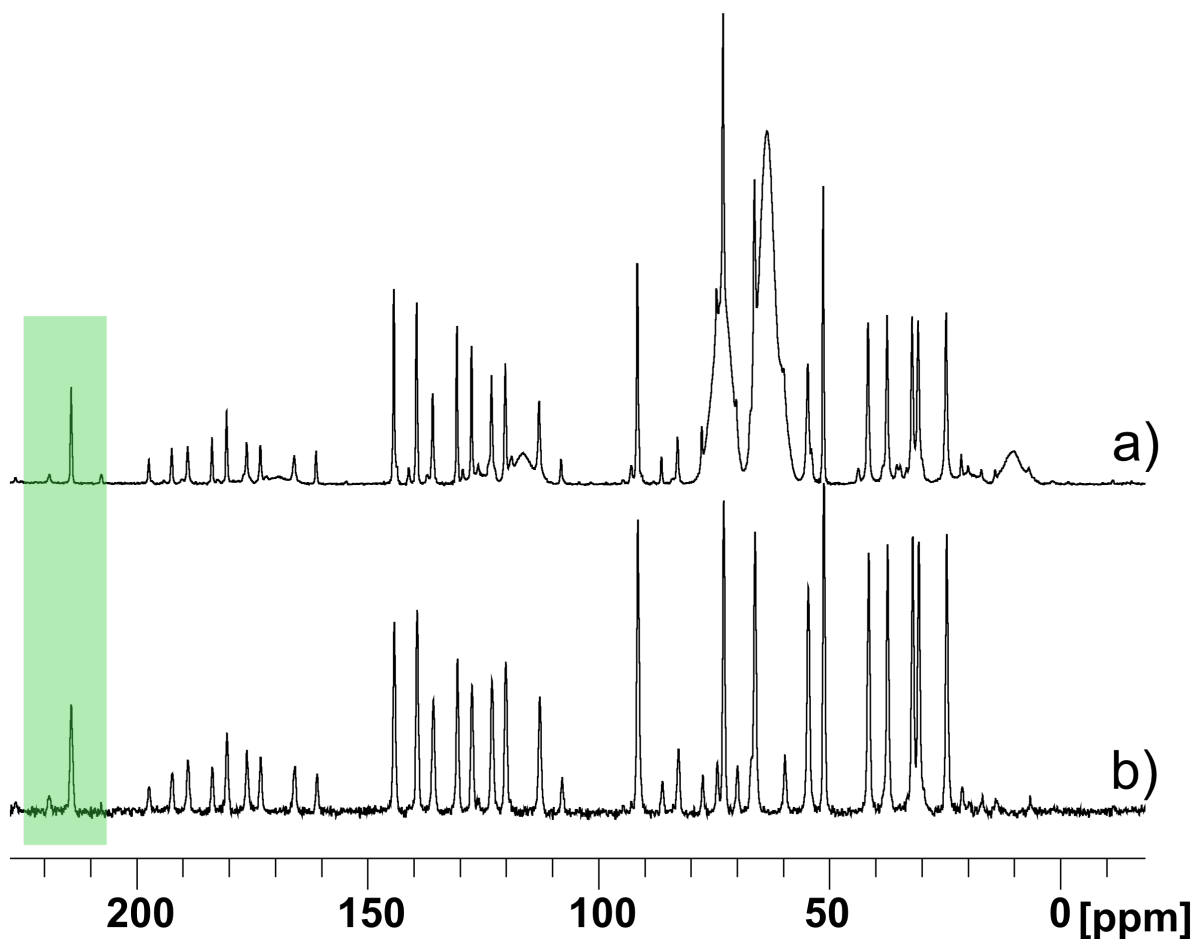


Figure 6-17, 1D carbon CP of naloxone: a) freebase monohydrate in 30 ul of 20 mM AMUPol in glycerol:D₂O:H₂O(60:30:10) with 40 mg of sample b) freebase anhydrous in 30 ul of 20 mM AMUPol in D₂O:H₂O(90:10) with 40 mg of sample. Recorded on a 600.13 MHz magnet for 4 scans with a contact time of 2000 μ s.

As can be seen in Figure 6-17 both the FA and FM forms are both the same hydrated form when in the presence of water. Both are also purely this hydrated form as both show the same nineteen carbons at the same ppm values. Going by the same carbon used to illustrate difference in previous comparisons, the green highlighted carbon now shows that the two forms are the same. Despite this it is impossible to definitively state what hydrated form this is, this is illustrated in Figure 6-18.

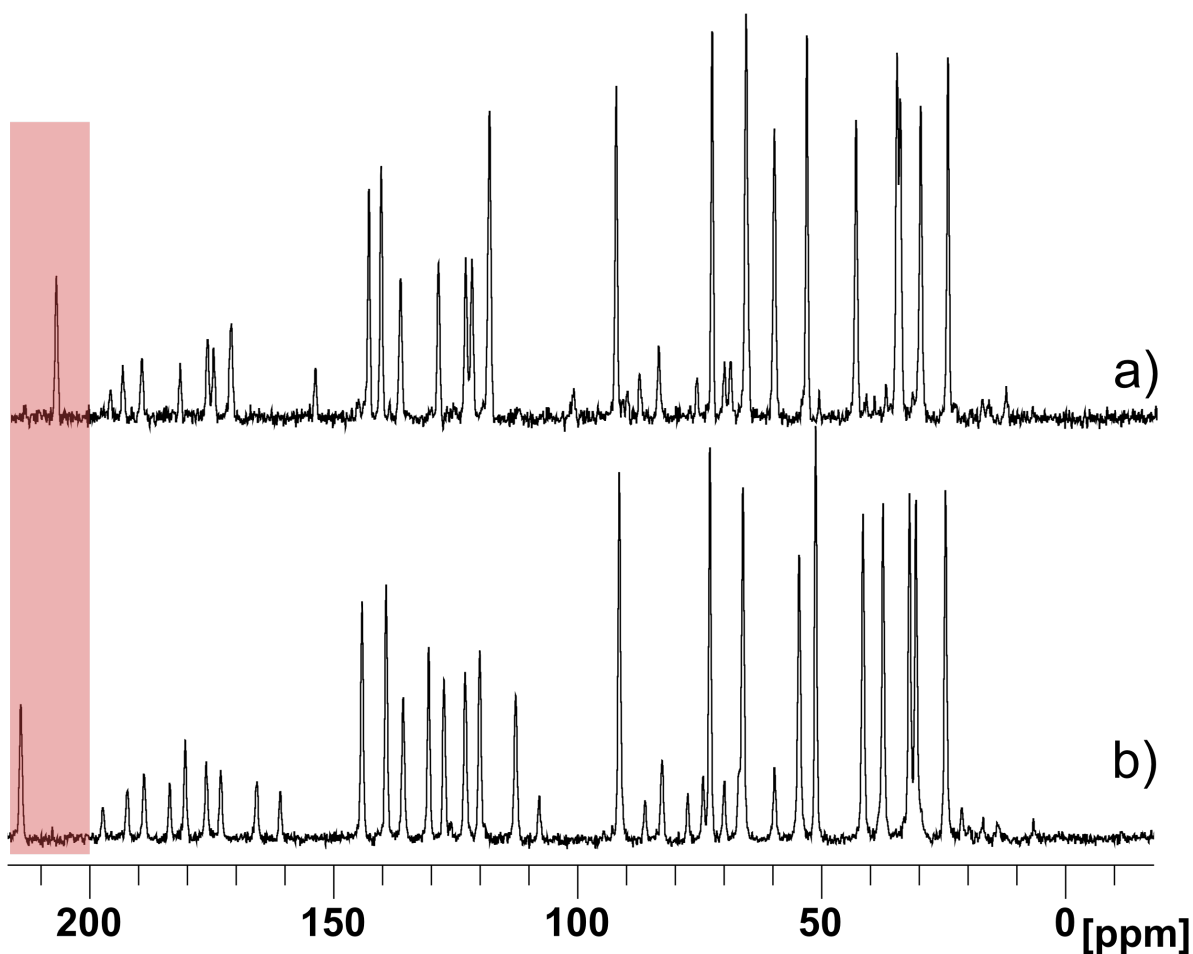


Figure 6-18, 1D carbon CP of naloxone: a) freebase monohydrate as the neat powder b) freebase anhydrous in 30 ul of 20 mM AMUPol in $D_2O:H_2O(90:10)$ with 40 mg of sample. Recorded on a 600.13 MHz magnet for 4 scans with a contact time of 2000 μs .

As is evident in Figure 6-18, the naloxone forms that produced these two spectra are different, again identified easily by the region in red with the same carbon not lining up in the two spectra. This means that the naloxone form that is formed when the freebase forms are in water is not the freebase monohydrate form. There is no higher hydrate form in the current literature and no mention of any polymorphs of any naloxone freebase forms. A sample of this mixed hydrate form under XRD could possibly identify what has occurred as it would be able to give details about the number of water molecules in the unit cell. A possibility is that a higher level of hydration can exist or possibly a variable hydration level. The freebase

anhydrous form, as shown, has degraded to a mixture of anhydrous and monohydrate but for the sake of continuity shall still be referred to as it the freebase anhydrous form.

An important difference between the forms, as shown in the crystal structure and the list of hydrogen bonds, is the involvement of the aliphatic chain in a hydrogen bond. This, according to the literature, is only involved in a hydrogen bond in the freebase monohydrate form. When looking at Figure 6-3, in the freebase forms there is a peak located at ~115 ppm, this is carbon 19. This peak is not present at the same location in the HCl form. This shifting of this peak is likely due to its involvement in a hydrogen bond and suggests that if there is indeed a higher hydration form of naloxone freebase then like the monohydrate form it also involves a hydrogen bond to a proton on carbon 19.

6.3 Differentiating via hydrogen

While the carbon analysis did allow for the differentiation of the solvate forms it also highlighted the neat powder of FA has a mixture of forms. To further investigate the structural differences between the forms, analysis into proton was made.

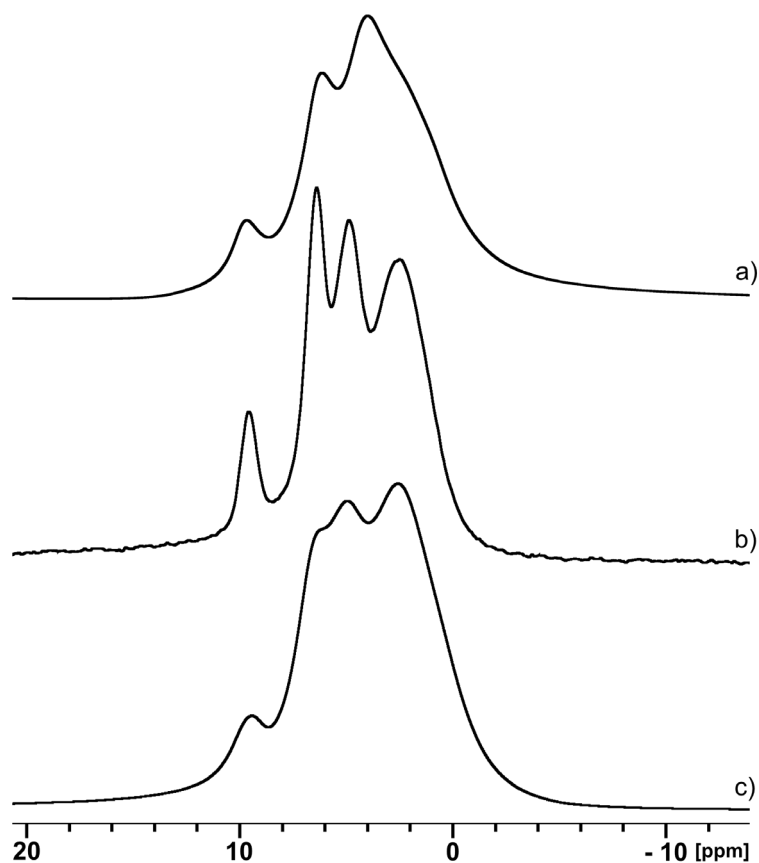


Figure 6-19, the 1D proton NMR spectra of the three naloxone forms that were available. Naloxone: a) HCl dihydrate b) Freebase monohydrate c) Freebase anhydrous. Recorded at 58 kHz on an 800 MHz magnet in 2 scans each.

As can be seen in the figure above there is a visual between the three forms when looking purely at 1D hydrogen when spinning at 58 kHz on a 600 MHz magnet but there is poor resolution. Conversely when spinning at 100 kHz on a 1 GHz magnet, there can be seen a clear difference between the forms. This was achieved during a trip to the National High-field Solid-state NMR Facility, though the naloxone freebase monohydrate form was not measured. Still, this is a fitting display of the analytical power of having both a stronger magnet and spinning faster, allowing a new peak to be observed in the freebase anhydrous form seen at a higher ppm than all others. It also showed that the 'single' proton across ~10 ppm may in fact be two next to each other in both forms.

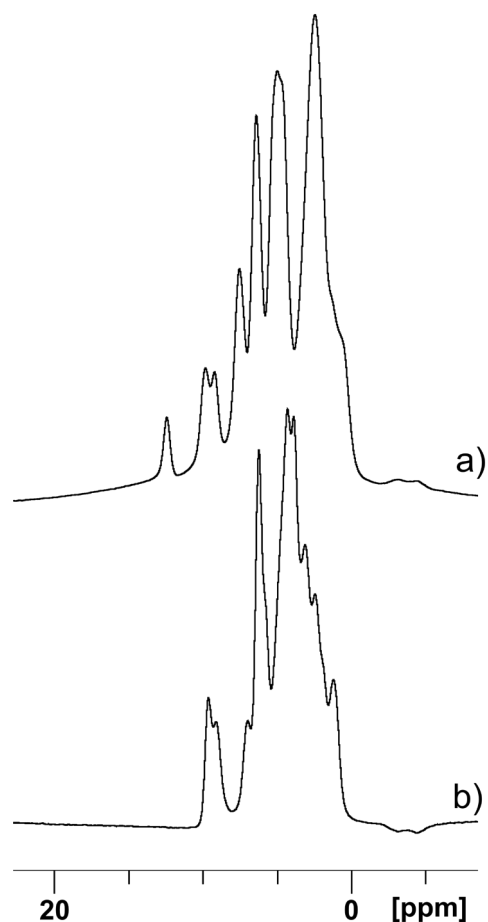


Figure 6-20, the 1D hydrogen spectra of naloxone: a) Freebase anhydrous b) HCl dihydrate. Recorded at 100 kHz on 1 GHz magnet, both in 4 scans.

When looking solely at proton an additional dimension must be included in which the chemical shift anisotropy (CSA) is reintroduced to be able to obtain more structural information. This is the orientational component of the chemical shift, and so will be affected by the difference in the hydrogen bonding between forms.

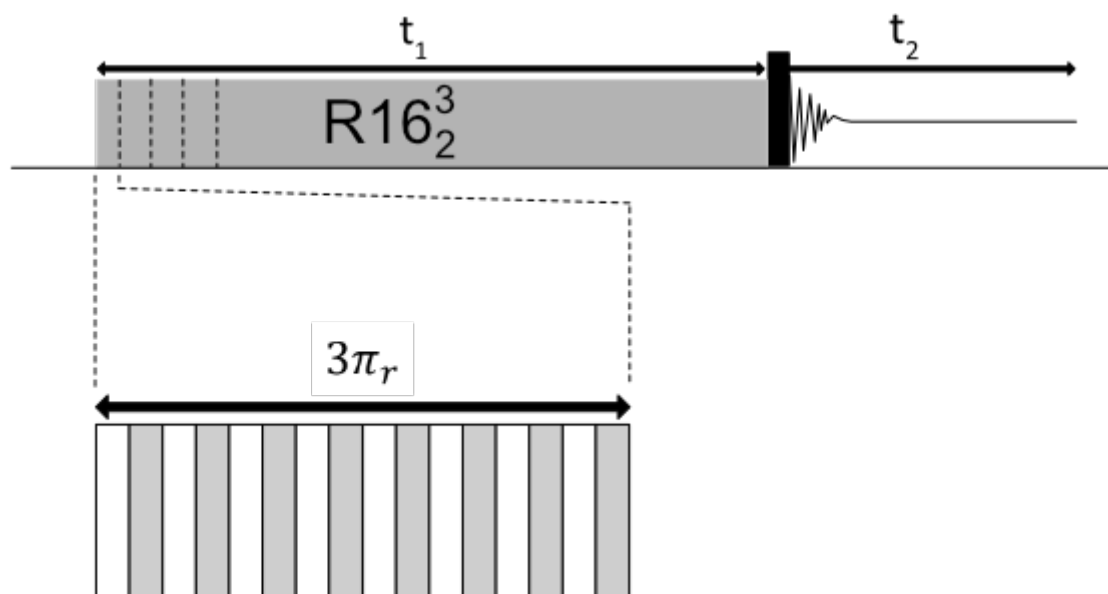


Figure 6-21, the pulse sequence design for, $R16_3^2$, which allows for the recording of anisotropic-isotropic correlation spectra at ultrafast MAS rates. Each bar represents a π pulse. This was adapted from [77].

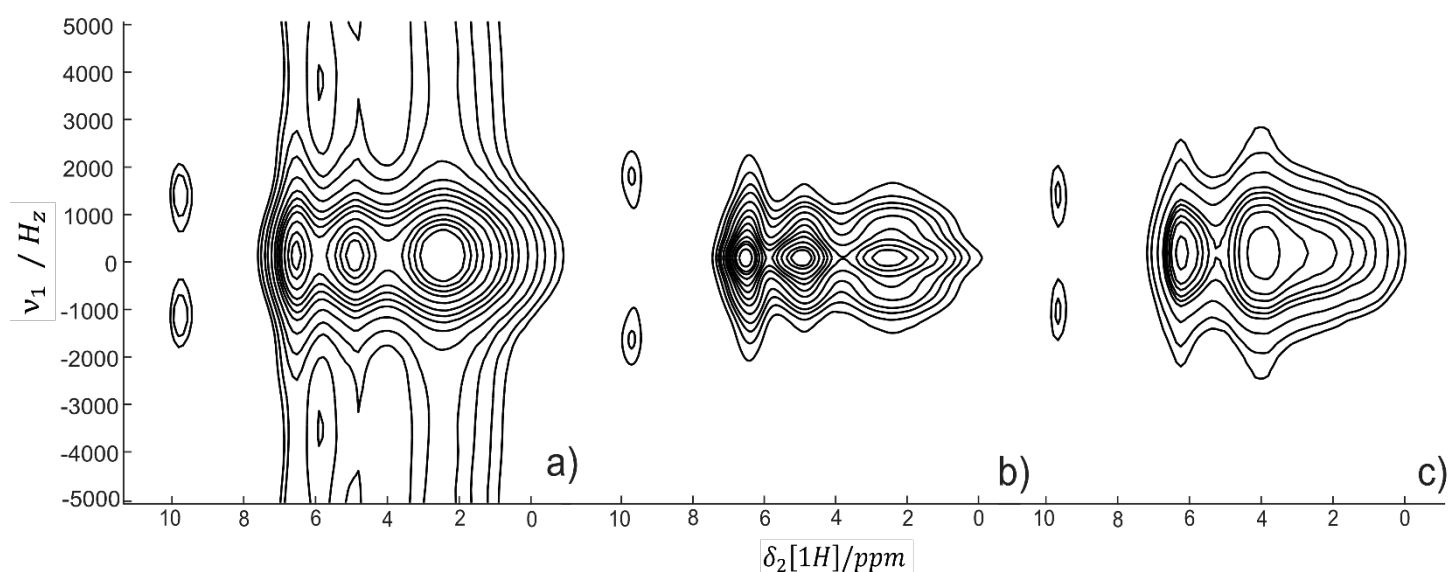


Figure 6-22, ^1H MAS NMR isotropic-anisotropic correlation spectra, $R16_3^2$, of naloxone a) Freebase anhydrous b) Freebase monohydrate c) HCl dihydrate. All three were recorded at 58 kHz on an 800 MHz magnet. This spinning speed gave a π pulse length of $3.2 \mu\text{s}$. 4096 points were acquired in f_2 and 48 in f_1 . Each spectrum was acquired in 4 scans with each being made up of t_1 lasting $38.4 \mu\text{s}$ leading to a spectra width of 26042 Hz.

The first recoupling technique to be discussed is $R16_3^2$, the pulse program of which is provided in Figure 6-21 which was previously investigated within the group [77]. This technique

reintroduces the CSA into the indirect dimension. This provides information on both the anisotropy and the asymmetry, though unlike experiments discussed later in this work, it does not provide data that would allow for the sign of the CSA to be known. This sequence produces a spectrum that is symmetrical around 0 in the f1 domain.

A clear difference between the three solvate forms can be seen in the peak at an isotropic shift of ~9.8 ppm. This comes from hydrogen 1, this is part of the -OH group that is present on carbon 3. The value of the anisotropy varies between the three solvates due to the difference in their involvement in hydrogen bonds. As can be seen below in Table 6-1 the C(3)-OH is involved in a H-bond in all three forms, though it preferentially forms a H-bond with water. The difference in the length of these bonds and the proton's environment is what leads to different values in the anisotropy. It is also worth noting that the proton at ~10 ppm in the freebase anhydrous form seems to always provide a lower signal when compared to the same proton in other forms. This could possibly be because this peak is coming from only one of the two forms that make up the freebase anhydrous sample.

Form	Hydrogen Bonds
naloxone HCl dihydrate	C(3)-OH...O(water) C(14)-OH...O(water) OH(water)...Cl ⁻ OH(water)...O-C(6)
naloxone freebase monohydrate	C(3)-OH...O(water) C(14)-OH...O(water) OH(water) ...O(2) C(19)-H...O-C(14)
naloxone freebase anhydrous	C(3)-OH...O-C(14)

Table 6-1, Hydrogen bonding in the three available forms of naloxone [70].

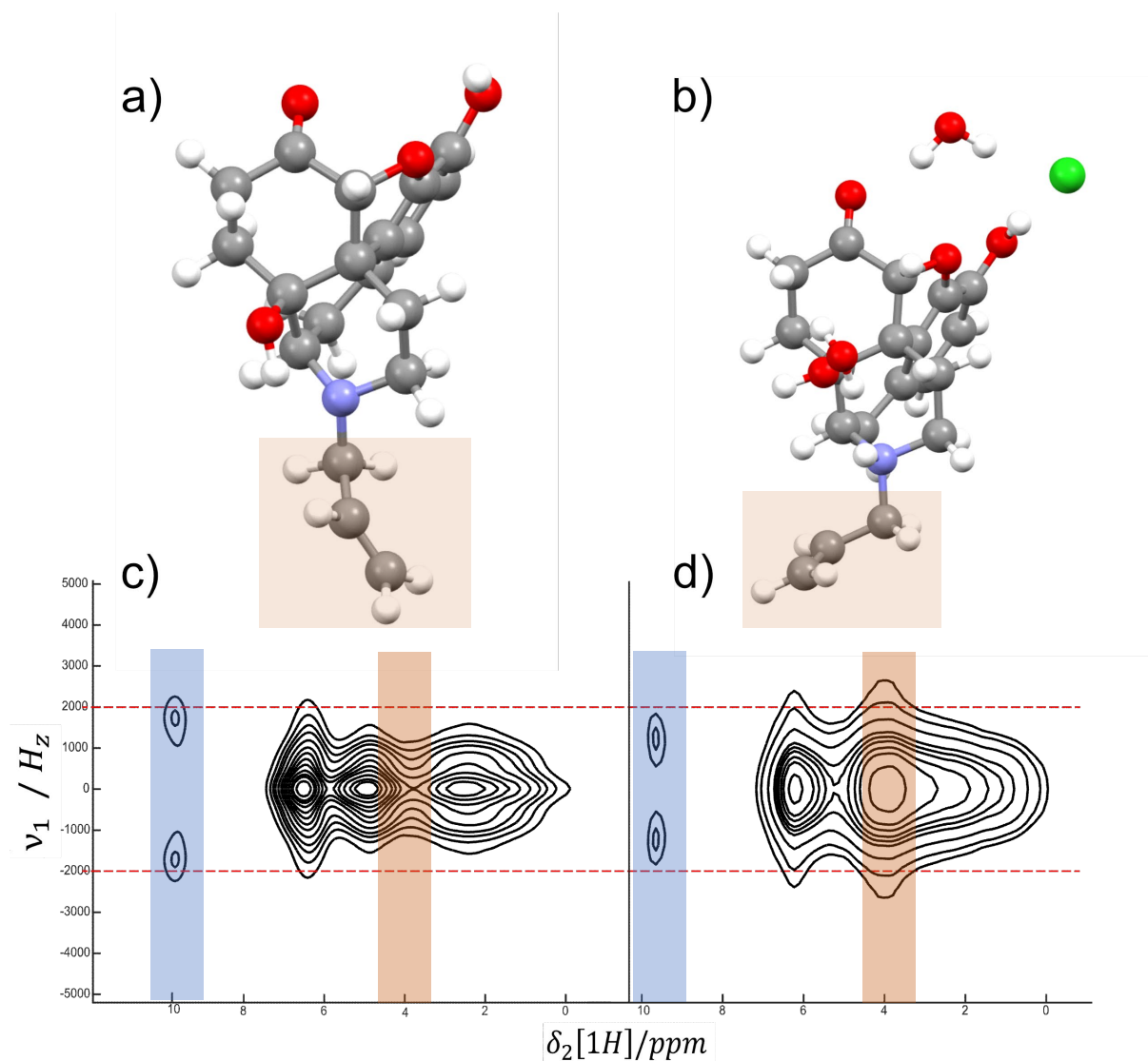


Figure 6-23, a) naloxone freebase monohydrate crystal structure. b) naloxone HCl dihydrate crystal structure. ^1H MAS NMR isotropic-anisotropic correlation spectra, $R16_3^2$, of naloxone c) Freebase monohydrate d) HCl dihydrate. Both were recorded at 58 kHz on an 800 MHz magnet. This spinning speed gave a π pulse length of 3.2 μs . 4096 points were acquired in f_2 and 48 in f_1 . Each spectrum was acquired in 4 scans with each being made up of t_1 lasting 38.4 μs leading to a spectra width of 26042 Hz.

The simplest way to now tell the forms apart is to see the clear separation of the groups of protons, with the HCl form having two concentrated areas with the other two having three. An easily observable difference between the two forms is the CSA value difference for the proton ~ 9.8 ppm, as highlighted in blue. This difference comes from the different hydrogen

bonds this proton is involved in. Looking back at Figure 6-2 the C(3)-OH is involved in different numbers of hydrogen bonds across the three forms. These different bonds will have different strengths and so will lead to larger values of CSA with the more, stronger, hydrogen bonds being present in the HCl dihydrate form as opposed to the freebase monohydrate form seen above. The HCl dihydrate form also has another interesting feature, this is its very wide cross section around an isotropic shift of 4 ppm, as highlighted in orange, which is wider than any other point across all three forms. This comes from the influence of the HCl group, this splits to a Cl⁻ which floats near carbons 17-19, also highlighted in orange, and the lone proton bonds forming a quaternary N⁺, this can be seen in Figure 6-23. This new proton, bonded to the nitrogen, forces the carbon 17-19 'tail' into a different orientation and the presence of the N⁺ and Cl⁻ cause the protons in the immediate vicinity, 23-26, which are 4/5 of the protons on the 17-19 carbon 'tail', to show a very large CSA value. This is the cause for the very wide band around an isotropic shift of 4 ppm. This is a clear example of a structural difference that can be seen using CSA recoupling techniques.

The next step was to look at the sign of the anisotropy. Due to the symmetrical nature of the $R16_3^2$ this cannot be measured, so a different symmetry based recoupling technique was used. This was $SC2_2^1$ which had recently been proposed by Kobayashi et al and the pulse sequence is given below in Figure 6-24 [69].

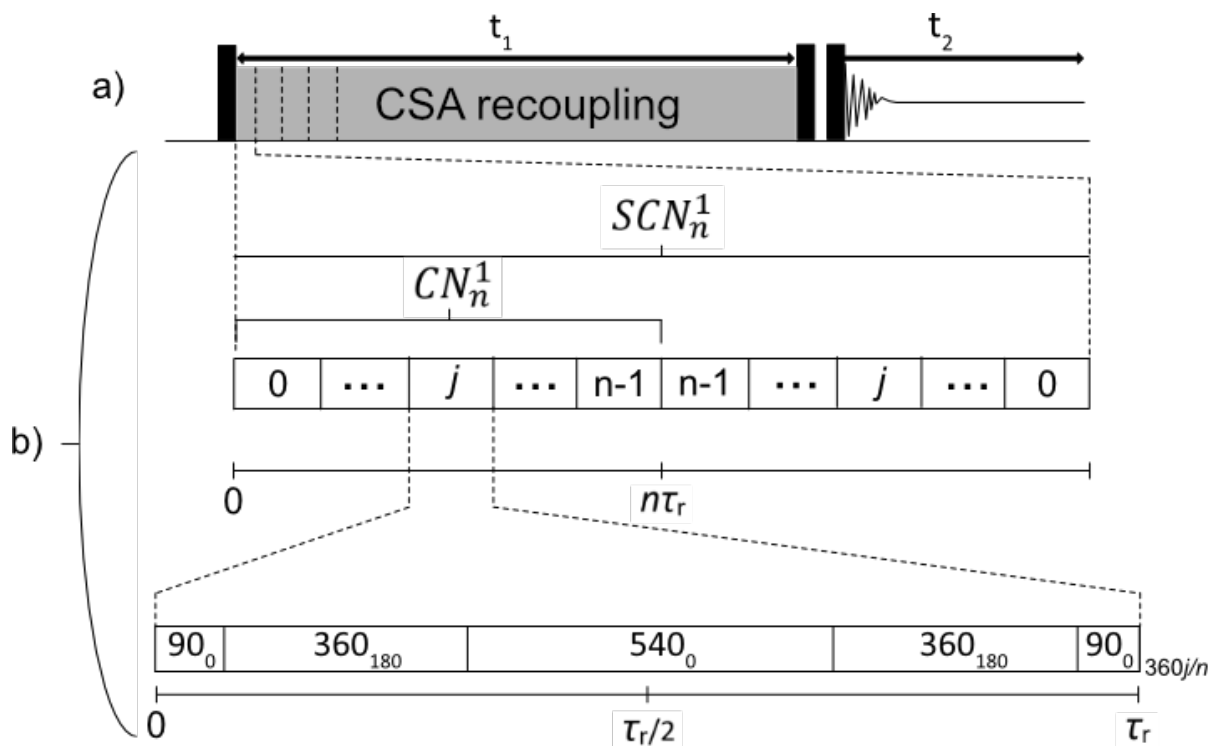


Figure 6-24, the pulse sequence design for $SC2_{\frac{1}{2}}$. a) The basic pulse sequence design for recoupling experiments where the exact pulses chosen depends on the spin-space winding numbers in question. b) the pulse sequence design unique to $SC2_{\frac{1}{2}}$

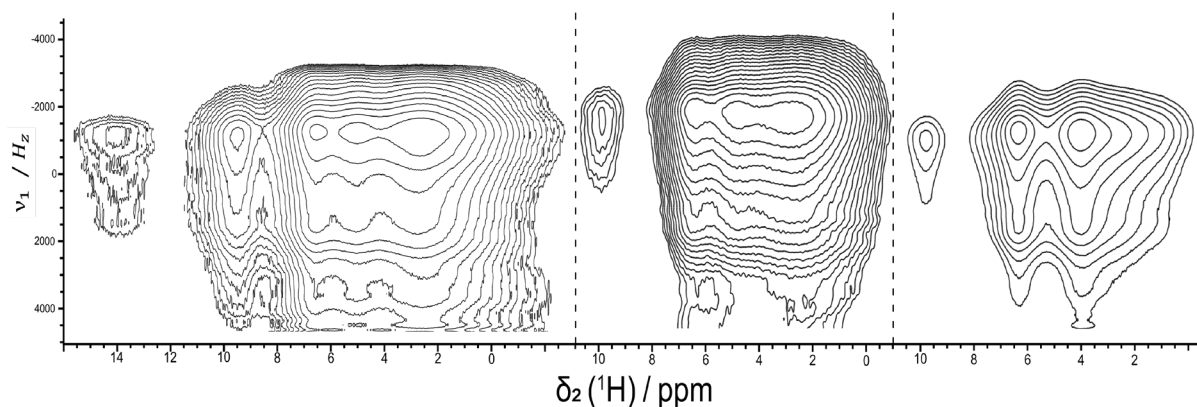


Figure 6-25, ^1H MAS NMR isotropic-anisotropic correlation spectra, $SC2_{\frac{1}{2}}$, of naloxone a) Freebase anhydrous b) Freebase monohydrate c) HCl dihydrate. All three were recorded at a spinning speed of 46296 Hz on an 800 MHz magnet. This spinning speed was calculated to give the correct symmetry for the pulse sequence with $\pi/2$ pulse lengths of $1.5 \mu\text{s}$, 2π pulse lengths of $5.3 \mu\text{s}$ and 3π pulse lengths of $8 \mu\text{s}$. 10240 points were acquired in f_2 and 64 in f_1 . Each spectrum was acquired in 8 scans. The length of the C sequence determines the spectral width in t_1 .

The spectra above allow for further investigation into the CSA of the two forms. Simply by observing the spectra it is apparent that the peaks at an isotropic shift of ~ 9.8 ppm have a positive value for their CSA in all forms. This is the same for the new peak at ~ 14 ppm in the freebase anhydrous form. This proton gave a weak signal relative to the other protons, hence why a greater number of contour levels were used compared to for $R16_3^2$. For the remainder of the protons, they are so close to each other that they cannot be individually distinguished. In all three forms the main 'groups' of protons, all show a positive value to CSA. This reflects the calculated values of CASTEP well where each form has only 3-4 negative CSA value protons. The positive CSA values come from the electron density being perpendicular to B_0 .

Cross sections of the ~ 9.8 ppm proton can be seen below in Figure 6-26. This figure highlights the difference in the CSA value between the same proton across the three forms. As previously stated this comes from the fact that the three forms have different hydrogen bonds associated with them. The freebase anhydrous form has the most distinct shape to it with both shoulders clearly visible. Despite this it is still clear to see that the others have larger values of CSA while maintaining similar asymmetry values. Naloxone HCl and the freebase anhydrous forms have similar values of CSA while freebase monohydrate is noticeably larger. This is of note as when viewing the crystal structures in a modeling program, the freebase monohydrate has the greatest distance between the two atoms involved in the hydrogen bond, this likely contributing to the larger CSA value that can be observed.

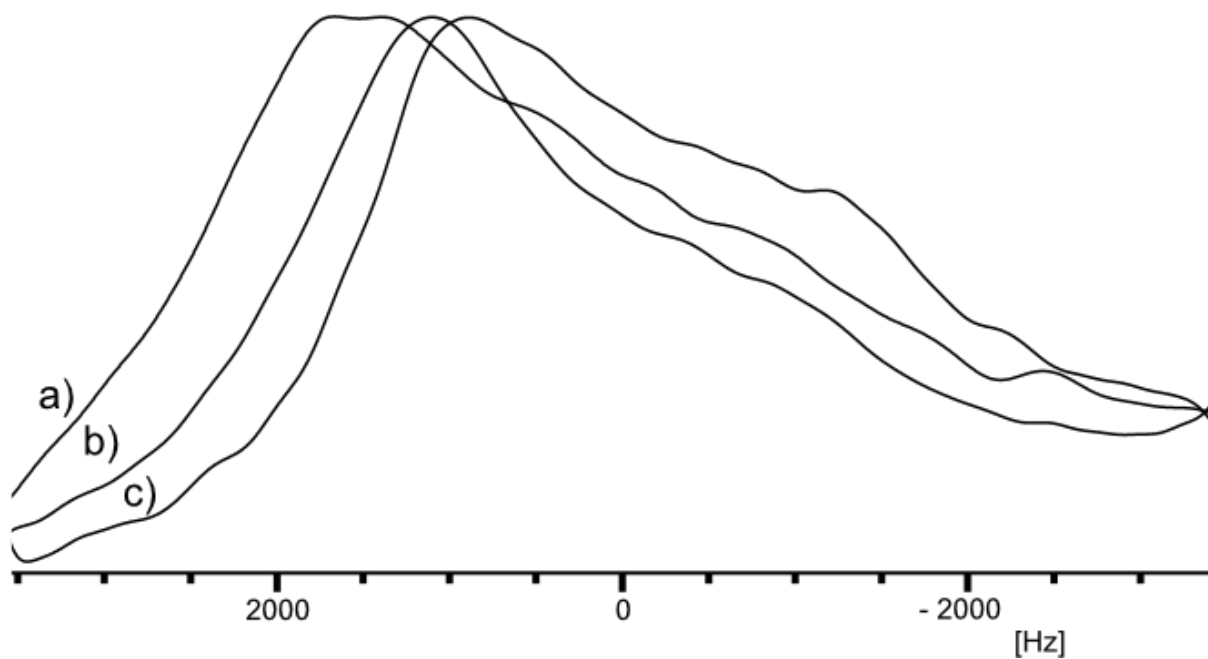


Figure 6-26 Extracted cross sections from the ^1H MAS NMR isotropic-anisotropic correlation spectra shown in Figure 6-25, naloxone a) Freebase monohydrate b) HCl dihydrate c) Freebase anhydrous. The three cross sections were all taken from the same proton, the one located at ~ 9.8 ppm, on the three forms.

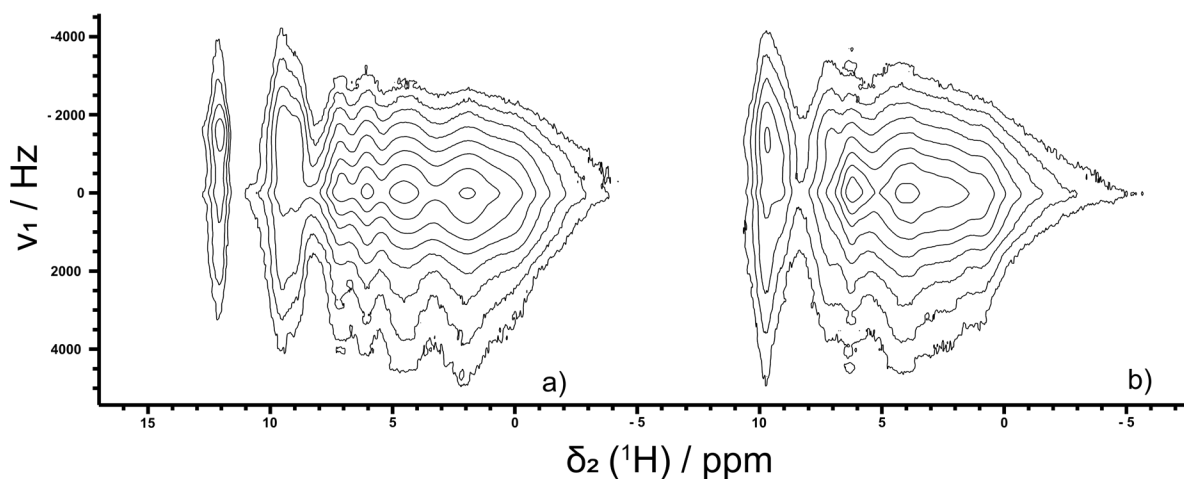


Figure 6-27, ^1H MAS NMR isotropic-anisotropic correlation spectra, $SC2_2^1$, of naloxone a) Freebase anhydrous b) HCl dihydrate. All three were recorded at 50 kHz on a 1 GHz magnet. This spinning speed gave a π pulse length of 3 μs . 10294 points were acquired in f_2 and 64 in f_1 . Each spectrum was acquired in 32 scans with each being made up of t_1 64 points with a dwell time of 3.4 μs .

Above in Figure 6-27 can be seen $SC2_2^1$ data that was obtained at The National High-field Solid-state NMR Facility on the 1 GHz instrument, using a 0.7 mm MAS probe. The advantage that the larger magnet provided allowed for the protons to be better dispersed, so providing more clarity to their distribution. They however do not show as clearly the overall positive CSA values that the experiments in Figure 6-25 did. A reason for this could be miss calibrated 360° and 540° pulses.

To understand the issue, the nature of the hardware of an NMR needs to be investigated. This is that when a pulse is switched on, for example a 90° pulse, there is a ramp into the pulse. Let us say the 90° pulse is 1.5 μs for 28.054 W, as was the case for the experiments in Figure 6-27. When the pulse is switched on it does not instantly go to 28.054 W, last 1.5 μs and then instantly stop. It ramps up to 28.054 W, maintains this power for a time less than 1.5 μs and then ramps down. Because 1.5 μs is such a short time, it is likely that the majority

of the pulse time is spent ramping. This does not have any impact on experiments normally. But because the $SC2\frac{1}{2}$ experiment requires both a 360° and a 540° pulse it plays a factor. This is because normally a 360° pulse is calculated as four times the 90° pulse, in this case being 6 μs . In the same fashion the 540° would be 9 μs as this is $6 * 1.5 \mu s$. However, because the 90° pulse likely spent a significant portion of time being ramped up and down the 360° and 540° would likely be shorter than expected. This is because for this pulse the rf field only has to ramp up and down at the end while maintaining the power level in the middle for longer, meaning a larger percentage of the pulse is actually at the full power.

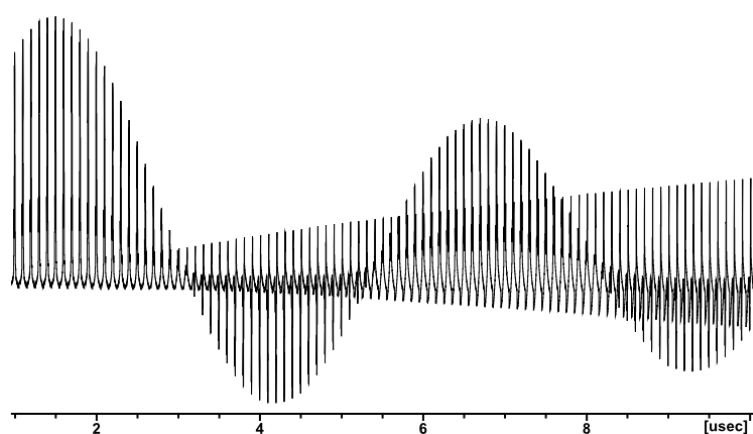


Figure 6-28, the nutation curve of naloxone HCl di-hydrate on proton. The power level was kept fixed at 28.054 W, while the length of the pulse was varied.

The manifestation of this problem can be seen above in Figure 6-28. While the 1.5 μs pulse at 28.054 W is indeed the 90° pulse. A 6 μs pulse is past the point where the 360° lies which is around 5.3 μs , as what is run in the experiment. The difference between where a pulse is calculated to be and where it actually is, is even more apparent with the 540° . As can be seen this is around 8 μs , whereas a 9 μs pulse would equate to a near 630° pulse. While the data acquired at the National High-field Solid-state NMR Facility was not as drastically different, it is possible that the pulse lengths may indeed have been incorrect for the longer pulses. One

thing to note in the above figure is an impurity that can be seen as an ever-increasing signal throughout the spectra. This impurity is present in all the naloxone samples performed at the time where the $SC2\frac{1}{2}$ experiment was performed. Though it does not show up in the 2D recoupling spectra.

6.4 Mixed hydration level affects.

In the freebase anhydrous form there is a very high ppm proton that can be seen around 12-13 ppm. This peak is not seen in the other samples. There are few occurrences that could cause a proton to be found at such a high ppm value but one of these is a considerably stronger hydrogen bond. While at the National High-field Solid-state NMR Facility a BABA experiment was conducted alongside the CSA recoupling experiments. This experiment identifies through space connections between protons and so shows where one proton is physically close to another in space.

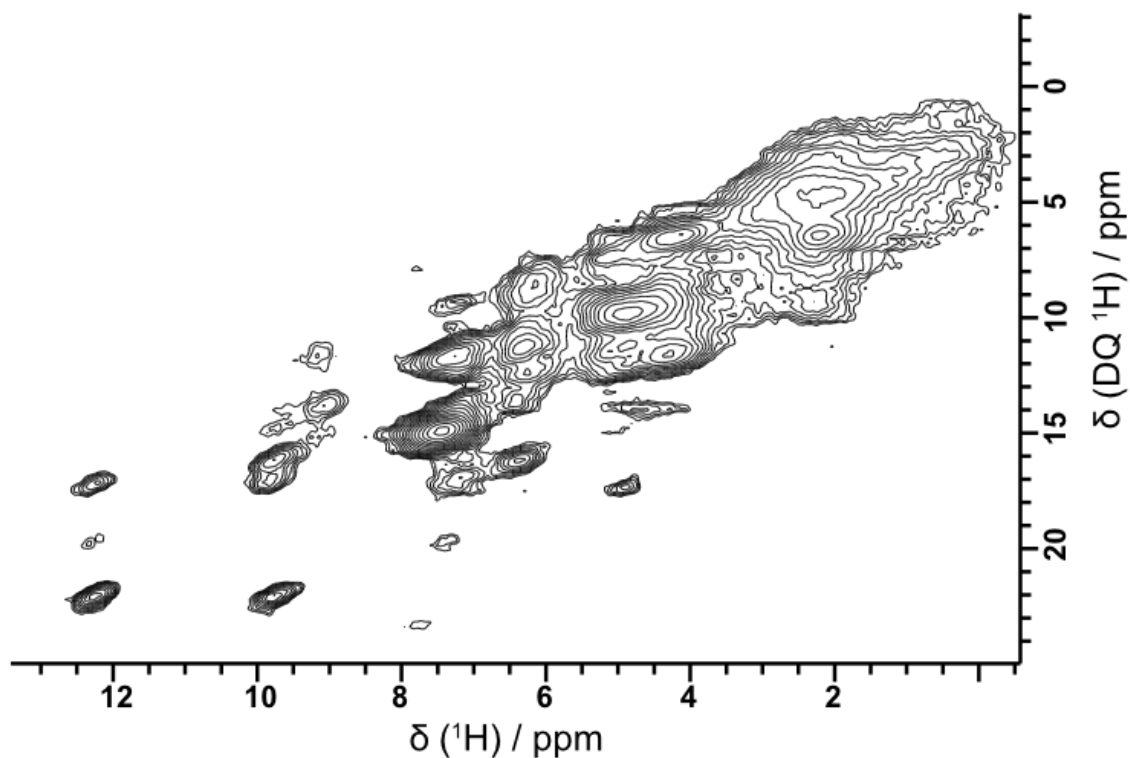


Figure 6-29, A ^1H ^1H BABA spectrum for naloxone freebase anhydrous performed at 50 kHz on a 1 GHz magnet. 10294 points were acquired in f_2 and 392 in f_1 . The spectrum was acquired in 16 scans with a dwell time of 3.4 us.

Figure 6-29 suggests that the proton at ~ 12.5 ppm is near to the proton at 9.8 ppm. This 9.8 ppm proton can be identified as the C(3)-OH proton based on chemical shift arguments and backed up by CASTEP data, shown later in this work. When viewing the crystal structures of freebase anhydrous in a program such as Mercury or in Figure 6-2, the nearest proton is the C(14)-OH. This proton is involved in hydrogen bonding in two of the hydrate forms including the freebase monohydrate form, which, as already discussed, makes up half of the freebase anhydrous sample due to exposure to air over time.

We do not see a peak this high in the pure freebase monohydrate form. This suggests that a new hydrogen bond is formed due to the mixture of freebase anhydrous and monohydrate. This bond would need to be considerably strong to be able to cause the proton to be

sufficiently shifted downfield. The BABA above also shows a correlation to 4 ppm, the current hypothesis is that this is a correlation to water and the new hydrogen bond formed is a bifurcated one with water, C(3)-OH and C(14)-OH. This could account for the proton being found at such a high ppm. A similar linkage is seen in the NOESY in Figure 6-30. A NOESY shows similar features to a BABA but with a subtle difference. While a BABA shows the nearest proton to another in space, a NOESY shows multiple near protons as this experiment allows for spin diffusion from one proton to another. This still shows a correlation between the high ppm proton of the C(14)-OH, the proton at 9.8, being C(3)-OH, and the peak around 5 ppm believed to be water. The water peak in the NOESY is negative, negative peaks in a NOESY come from double-flip double-flop terms as discussed by Vipin Agarwal in 2020 [78]. These two experiments support the hypothesis that the water molecule in this mixed hydration form contributes to the hydrogen bond, leading to the high ppm of the proton.

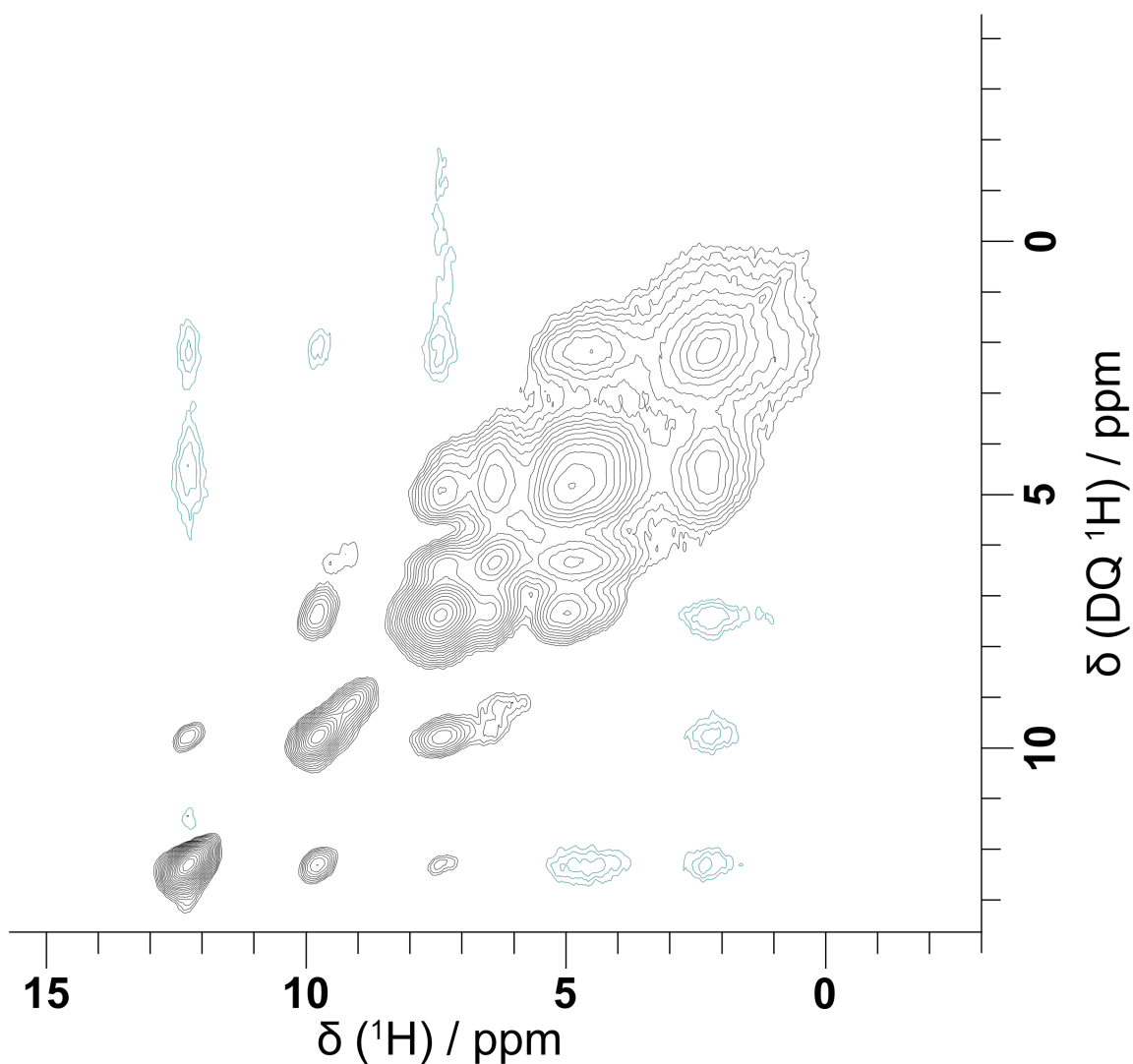


Figure 6-30, A ^1H ^1H NOESY spectrum for naloxone freebase anhydrous performed at 50 kHz on a 1 GHz magnet. 10294 points were acquired in f_2 and 392 in f_1 . The spectrum was acquired in 4 scans with a dwell time of 3.4 us.

One noticeable difference between the spectra recorded at the National High-field Solid-state NMR Facility and the ones recorded at the University of Nottingham instruments is the movement of the location of the high frequency proton. In the prior experiments this proton is located ~ 12.5 ppm whereas in the latter it is present ~ 14 ppm. This is the only proton that has its position shifted as all others lineup correctly with the older version of the sample. This is a significant shift and could be caused by different possibilities. Changes in MAS rates do

not have an effect on hydrogen bonding, and as hydrogen bonding is an electrostatic interaction, increased magnetic fields would also not have this affect. This leads to the conclusion that the sample has changed. There is a two-year time period between the experiments done at the National Facility and later at University of Nottingham, during this time the sample would likely have degraded further into the anhydrous, monohydrate mixture as previously discussed. This further degradation of the sample is hypothesized to be the cause of this movement of the proton. As the sample built up a greater hydration level the hydrogen bond formed strengthened.

When examining the various forms of naloxone, there exists the possibility that the observed differences result from a polymorphic transformation rather than variations in hydration levels. A polymorphic shift could potentially explain the observed differences between forms and the higher proton ppm value, attributed to the formation of a new hydrogen bond. However, my hypothesis leans towards a change in hydration levels rather than polymorphism because there is data indicating that the change occurs gradually over time. This suggests a shift in hydration levels, as opposed to polymorphism, since the most plausible explanation for this gradual change is the influence of water from the air altering the form over time. If it were a polymorphic shift, a gradual change over time would be unlikely.

6.5 Conclusions

The aim of this section of work was to investigate whether solid state NMR could be used to first differentiate different solvate forms of naloxone and if it could provide any structural insight. By using DNP it was possible to perform a refocused INADEQUATE on unlabelled samples. This allowed for the almost complete assign the ^{13}C spectra. Once this was done it allowed for easy differentiation of the solvate forms using carbon alone by simply viewing the 7, 8, 15, 10 carbons whose order varies from solvate to solvate as well as the movement of carbon 6. This shows the utility of DNP in allowing experiments to be performed that would be traditionally unfeasible. It is difficult to say for certainty what caused the ordering on these carbons to change though the differing hydrogen bonds and crystal packing across the solvates is the most likely the cause.

Investigations into ^{13}C also lead to the discovery that the freebase anhydrous had degraded to a mixture of anhydrous and monohydrate. The degradation was shown to progress over time with the location of a proton being increasingly downfield shifted between two sets of experiments a year apart. The carbon experiments comparing DNP data to neat preparations brought this degradation into the light but also showed that there exists a form of naloxone freebase that has yet not been documented in the literature. This is believed to be a higher hydration form or a mixed hydration form, as opposed to be polymorphic one, as it is formed when the freebase forms are exposed to water in the atmosphere over time or when in an aqueous solvent.

This section also showed that DNP sample preparation can significantly affect the solvate level of the sample being analysed. Further studies may benefit from greater exploration into

DNP sample preparation methodologies as to not only provide greater level so of enhancement but also to better help identify solvate differences.

The use of CSA recoupling experiments shows how they can be used to easily differentiate similar proton spectra which would usually be challenging due to poor resolution. The biggest advantages of CSA recoupling are insights into the structural differences between the forms. The two most prominent examples of this were the CSA differences of the 9.8 ppm protons involved in hydrogen bonds, the other being the aliphatic chain differences between the solvates. The change in orientation of this chain causes a pronounced increase in the value of the CSA. This suggests that other such changes, caused possibly by a chemical reaction or a polymorphic change, could be seen by this technique. When comparing the two techniques $SC2\frac{1}{2}$ comes with the obvious advantage of allowing for the sign of the CSA to be determined.

This technique also resolved an additional proton that could not previously be separated from noise. This is likely because the signal is so low but with the CSA parameter it could then be seen. While $R16\frac{2}{3}$ does not allow the sign to be determined it does have its own advantage in its robustness. Because the sequence does not require pulses as short as in the $SC2\frac{1}{2}$ sequence it means there is a lower pulse power requirement. The sequences robustness means that slight miss calibrations will usually not lead so significant loss in resolution. The sequence is also usually sufficient to be able to view any structural differences visible via CSA differences.

Chapter 7: Calculations

Simulations in any analytical field, including NMR, can be used as predictive tools or confirmatory tools. In the case of this work three programs were used in conjunction to be able to predict the outcome of NMR experiments.

The first program is CASTEP or Computer Aided Software for Theoretical and Experimental Physicists, it is a program that performs density functional theory calculations [79]. Practically this involves providing the software with a cartesian set of coordinates for all the atoms in the atomic cell, using this CASTEP can provide theoretical tensor values, allowing us to have estimated values of anisotropy, asymmetry, and isotropy.

For CASTEP to function it requires three files for each calculation. The first is the *.cell* file for the compound in question. A *CASTEP.sh* file that instructs the computer to perform CASTEP calculations on the given *.cell* and a *.param* file. This last accompanies the *CASTEP.sh* file and includes the exact type of CASTEP calculation to be run and the required settings. Examples of these files will be included in the appendix.

Originally *.cif* files are generated from the X-ray diffraction experiments. These are single unit cells and are converted to a *.cell* file, this is simply the x, y, z coordinates of the atoms in the format CASTEP needs. Geometry optimisation is then performed, this is a process of changing the cut-off energies, given in Ryberg energy (ry), to move atoms in the cell to find the lowest energy of the system, and so the most likely actual location of the atoms. The other parameter being optimised is the k-point. This is related to the density of the Brillouin zone which is to be sampled for calculations.

The output of these calculations is obtained in a *.castep file*, an example of the relevant parts of this is also included in the appendix. This contains, among other information, the NMR parameters of the absolute shielding tensor σ .

When looking at the chemical shift of a calculated atom a σ_{ref} is used, this is a reference shielding which is used to convert the chemical shift to an appropriate scale for experimental comparison. To obtain a reference shielding for a compound the experimental data is plotted against the calculated and the y intercept of a line of points is deemed the σ_{ref} [80]. This is the practice for carbon as the peaks are clearly resolved. In the case of the proton data, where this technique was not possible due to ssNMR resolution, the σ_{ref} was obtained from the literature and previous values obtained in the group [81–83].

When considering simple experiments like ^{13}C CP these δ_{iso} can then be directly compared to experimental spectra, as can be seen later, but for more complex experiments such as the symmetry based recoupling techniques further steps are required.

This leads to the next program used which is SIMPSON, Simulation Program for Solid-State NMR Spectroscopy. SIMPSON requires a *.in* file which contains the asymmetry and anisotropy values as well as the parameters, such as spinning speed and magnet strength, and the pulse program. Using this SIMPSON can generate 1D proton spectra for the given pulse program using the values obtained from CASTEP. The third program used will be discussed later.

7.1 Geometry optimisation and Convergence

Like all other CASTEP calculations the University of Nottingham High Performance Computer (HPC) was used. The original crystal structure files were obtained from the Cambridge Crystallographic Data Centre (CCDC). These were then geometrically optimized and converted

to produce the best quality data. This was done by measuring the distance between two chosen nuclei while varying values of k-point spacing and cut off energy. This was performed until there was no change in the distance measured. At this point there was no change in the location of atoms in the unit cell with increasing computational efforts. Decreasing the k-point spacing from 1 downwards leads to increasing computational demand and so finding the highest value where no change occurred is ideal to help reduce computational time. With cut off energy the same trade-off between better accuracy and computational demand exists, this time with the higher values being the more demanding.

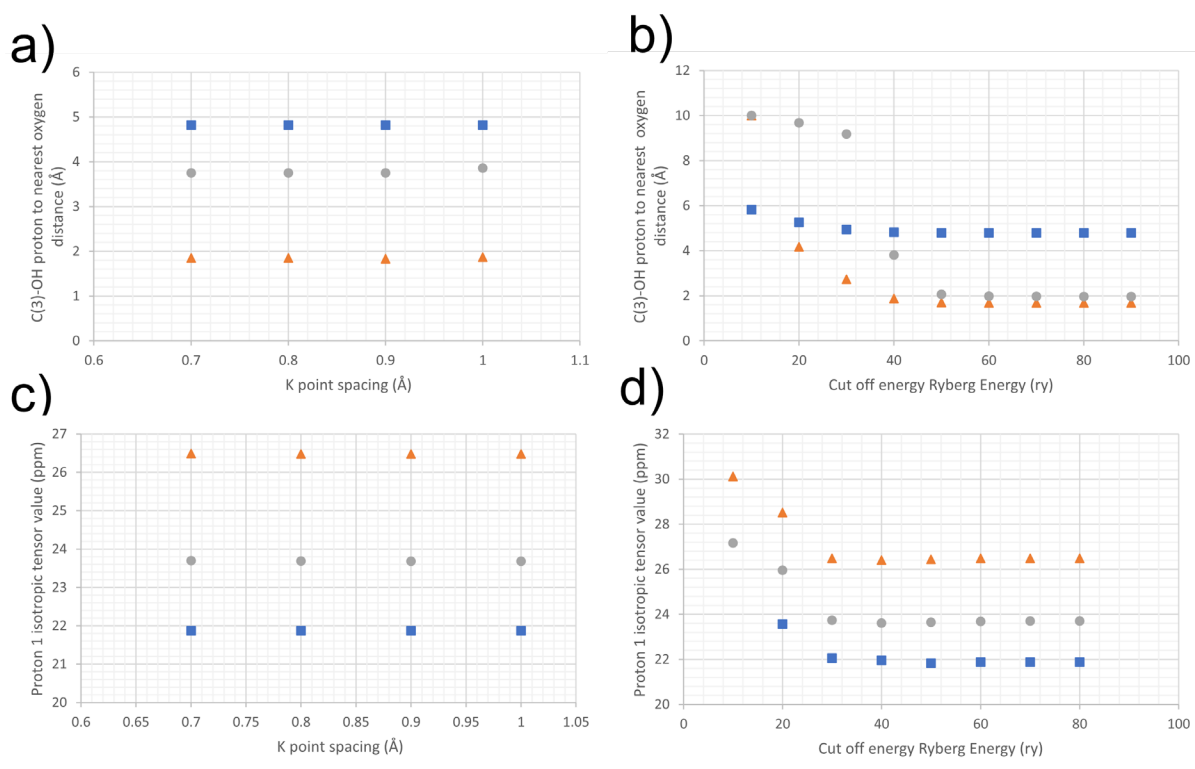


Figure 7-1, geometry optimisation for the three naloxone forms, HCl Di-hydrate (■), Freebase monohydrate (·), freebase anhydrous (triangle). a) Geometry optimisation based on change in the distance between C(3)-OH proton to the nearest oxygen, with decreasing k-point spacing. b) Geometry optimisation based on change in the distance between the C(3)-OH proton and the nearest oxygen with increasing cut off energy (ry). c) Convergence based on change in Proton 1 isotropic shift value (ppm) with decreasing k-point spacing. d) Convergence based on change in Proton 1 isotropic shift value (ppm) with increasing cut off energy (ry).

Convergence is the same process as geometry optimisation where cut off energy and k-point spacing are varied until there is no change in the shift values of a given proton. As can be seen in Figure 7-1 above, there is little to no change across all graphs when varying the k-point spacing. It is not conveyed in the graphs but at cut off energies of 10 and under there is little to no discernible structure of the atoms and they are scattered throughout the cell. Across all forms and both optimisations there is a decrease in the distance chosen and the proton ppm with the increased energy values, this however also plateaued like k-point spacing. This process of geometry optimisation and convergence is of key importance when examining a new crystal structure.

7.2 ¹³C Calculations

To start with CASTEP calculations were performed for ¹³C. CASTEP was used to check the assignments done by the RI technique, as well as to help look at the few carbons that were unassignable.

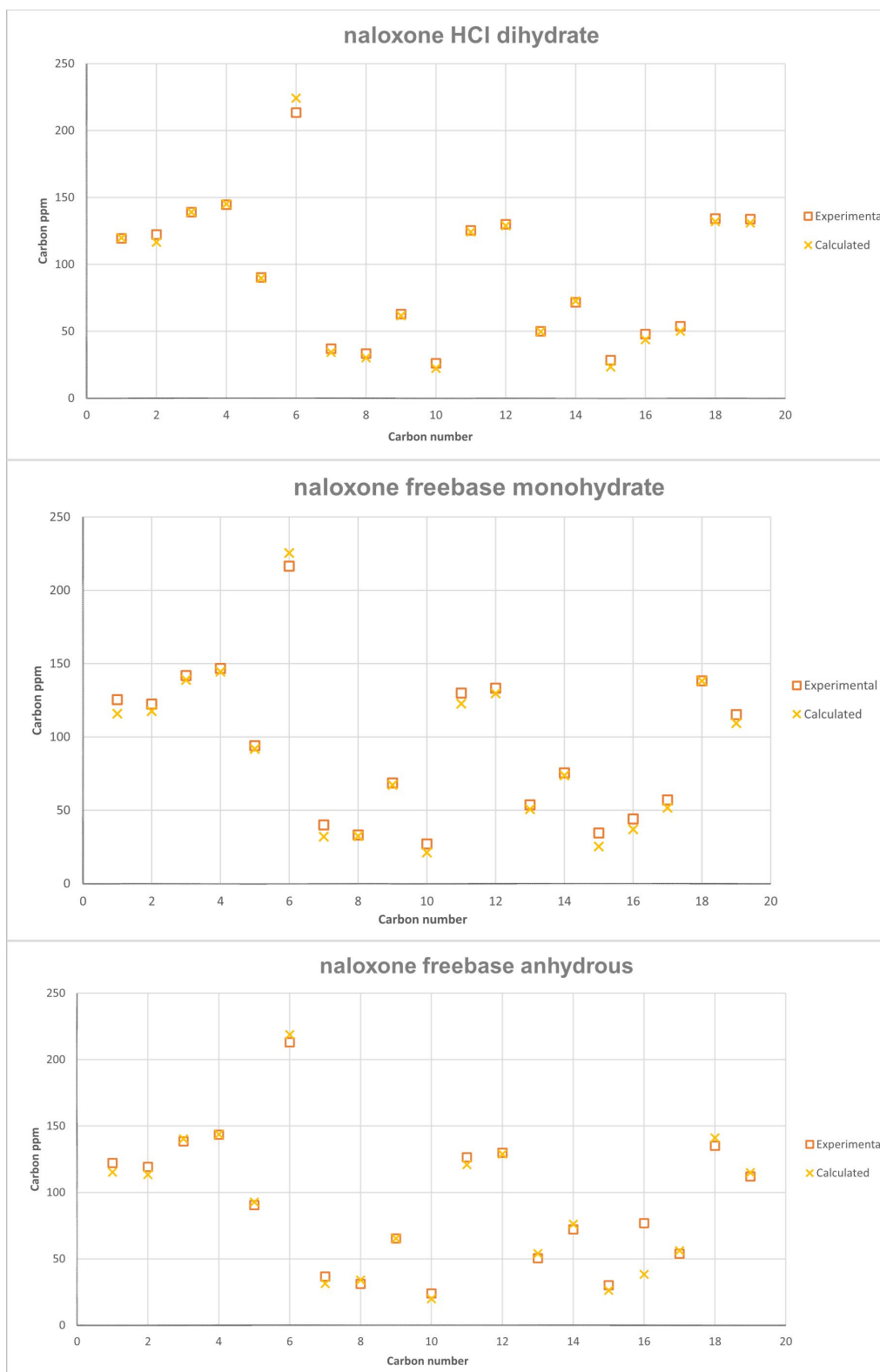


Figure 7-2, A graphical representation of the differences between experimental data and CASTEP calculated data for the three naloxone forms. The ppm's of the calculated (x) and experimental (□) carbons are plotted against their corresponding number as based on the numbering in Figure 6-1. In this case calculated ppm is δ_{iso} from the equation 2.18. The table for the data can be found in appendix 6.

The effectiveness of CASTEP can be seen above, while some carbons are in error by a greater degree the majority are within a few ppm with the mean difference being 4.5 ppm. Unlike for the proton spectra, SIMPSON was not needed due to the clear separation of the peaks leading to little ambiguity. CASTEP is generally more accurate with its carbon calculations than it is with its proton calculations. This is because the location of a carbon can be more accurately predicted than that of a proton can due to the more accurate location provided by XRD.

The carbon shift values that were used in Figure 7-2 for the freebase anhydrous form came from the TEKPol TCE ^{13}C spectrum. The freebase monohydrate data came from the AMUPol, in glycerol, D_2O and H_2O , preparation which has already discussed means this form is likely not monohydrate.

7.3 Proton calculation and simulation

Because protons are all located between 0-15 ppm they are often seen as groups rather than individual protons. This means that the power of simulation becomes far more valuable as it is often impossible to analyse an isolated peak in a proton spectrum. This is where SIMPSON comes in. By providing SIMPSON with values of anisotropy, asymmetry and the pulse program used it can output a 1D spectrum which can then be compared to the experimental data.

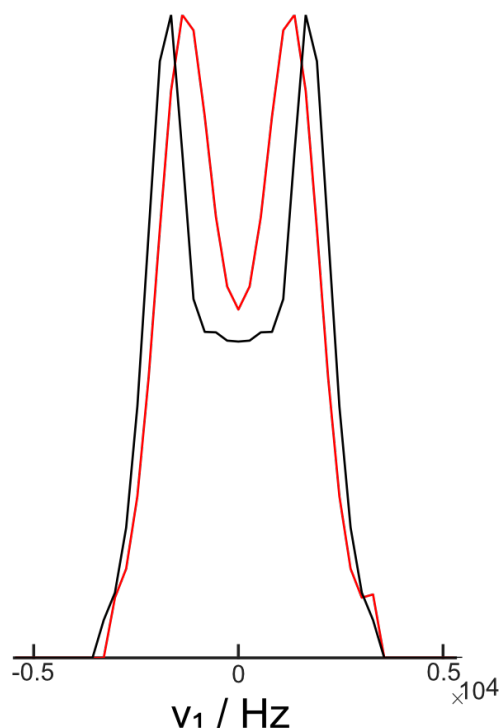


Figure 7-3, naloxone Freebase Anhydrous $R16_3^2$ cross section at 9.6 ppm (red) overlaid with the CASTEP predicted values for the same proton (black). The experimental spectrum was recorded at 58 kHz on an 800 MHz magnet. This spinning speed gave a π pulse length of 3.2 μ s. 4096 points were acquired in f_2 and 48 in f_1 . Each spectrum was acquired in 4 scans with each being made up of t_1 lasting 38.4 μ s leading to a spectra width of 26042 Hz. The simulated component was generated using CSA values of 22.44 with an asymmetry value of 0.44. The simulated spectra also had its settings matched to the equivalent values of the experimental.

As can be seen above, cross sections of the $R16_3^2$, and other sequences, can be extracted and compared to computational values. While computational values cannot exactly predict the outcome of experimental spectra, they can be used to create rough expectations. Because it would be impractical to compare the simulated spectra to the unresolved experimental protons for every compound analysed a way to create a 2D spectrum from the single 1D spectra. A brief overview of how this was achieved will be given below.

Using MATLAB as the program for which the code would be written, due to its inbuilt ability to easily view graphs, the first stage would be to automate the production of the 1D spectra.

The first step to this was to extract all the values of asymmetry, anisotropy and isotropy from the output of a CASTEP calculation for all protons and store this in an excel file.

For the simulation the *.in* file is required, this contains the asymmetry, anisotropy and pulse program that will be run for each individual proton. Some of the other parameters include the spinning speed, and magnet strength. This necessitated a list of parameters that can be easily changed to run different samples and experiments without having to manually rewrite every *.in* file. This leads, to the list of changeable parameters at the start of the MATLAB code, this will be shown in appendix x. The code, named Pantheon, currently lists 24 parameters than can be edited to obtain a better match between simulated and experimental spectra. The idea for Pantheon came from work previously done in the group but was written from scratch [77]. For now, the relevant parts of this are the ability to mass produce *.in* files for each proton given an excel file list. There is no limit to the number of protons that can be processed here outside of time and CPU limitations. With this list of *.in* files SIMPSON simulations can then be run with each one generating a 1D NMR slice.

This then leads to the main issue of producing a 2D spectrum as these 'slices' do not have width in the f2 dimension. The slices are placed onto the f2 axis based on the isotropic ppm value for each one from CASTEP. This leaves impossibly narrow peaks unachievable even with an infinite MAS rate. To make the calculated values comparable to experimental spectra each slice must be given 'width' along the f2 axis. The process to accomplish this is illustrated in Figure 7-4:

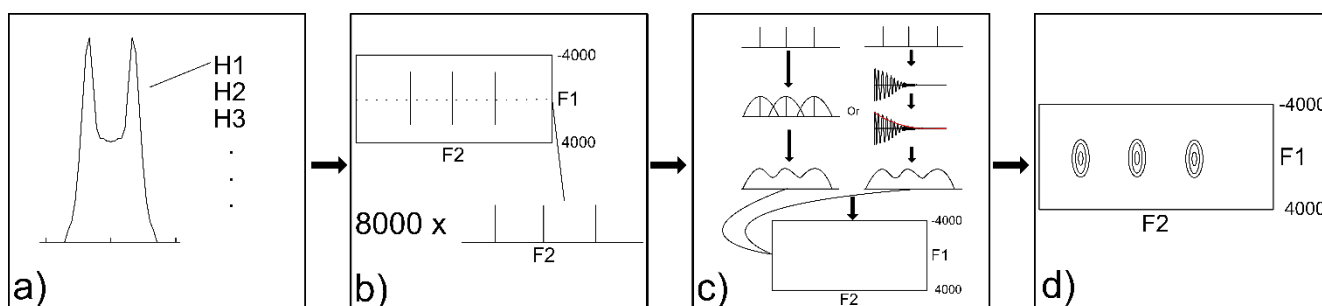


Figure 7-4, A diagram of the processes of turning 1D spectra in a 2D spectrum. a) obtaining all 1D spectra of a given compound, b) placing the 1D spectra slices onto a grid depending on their isotropic ppm and then taking 'slices' along the whole range of the F1 axis. c) the slices being given width along the F2 axis in two possible ways and then reintroduced back into the plot leading to d) the output of the process where the 1D's have been combined to create a single 2D.

As can be seen in part c) of Figure 7-4 there is a choice of how to add the width to the F2 axis, one being the 'Normal Distribution'(ND) way and the other being the 'Fourier transform way.' In the ND way each peak in the slice is transformed into a normal distribution curve with the height of the curve being set to the height of the peak. Where distributions overlap, they are summed to produce one continuous gradient.

For as to how wide these distributions are, that was calculated by measuring the width of a single proton at various spinning speeds in experimental data to obtain a ratio of spinning speed to peak width. The same process was performed on simulated data in two ways, first by measuring the width of a proton peak vs different sigma values for normal distribution. The other way was measuring the width of a proton peak vs different values of gaussian weighting. The results of these can be seen in the graphs following.

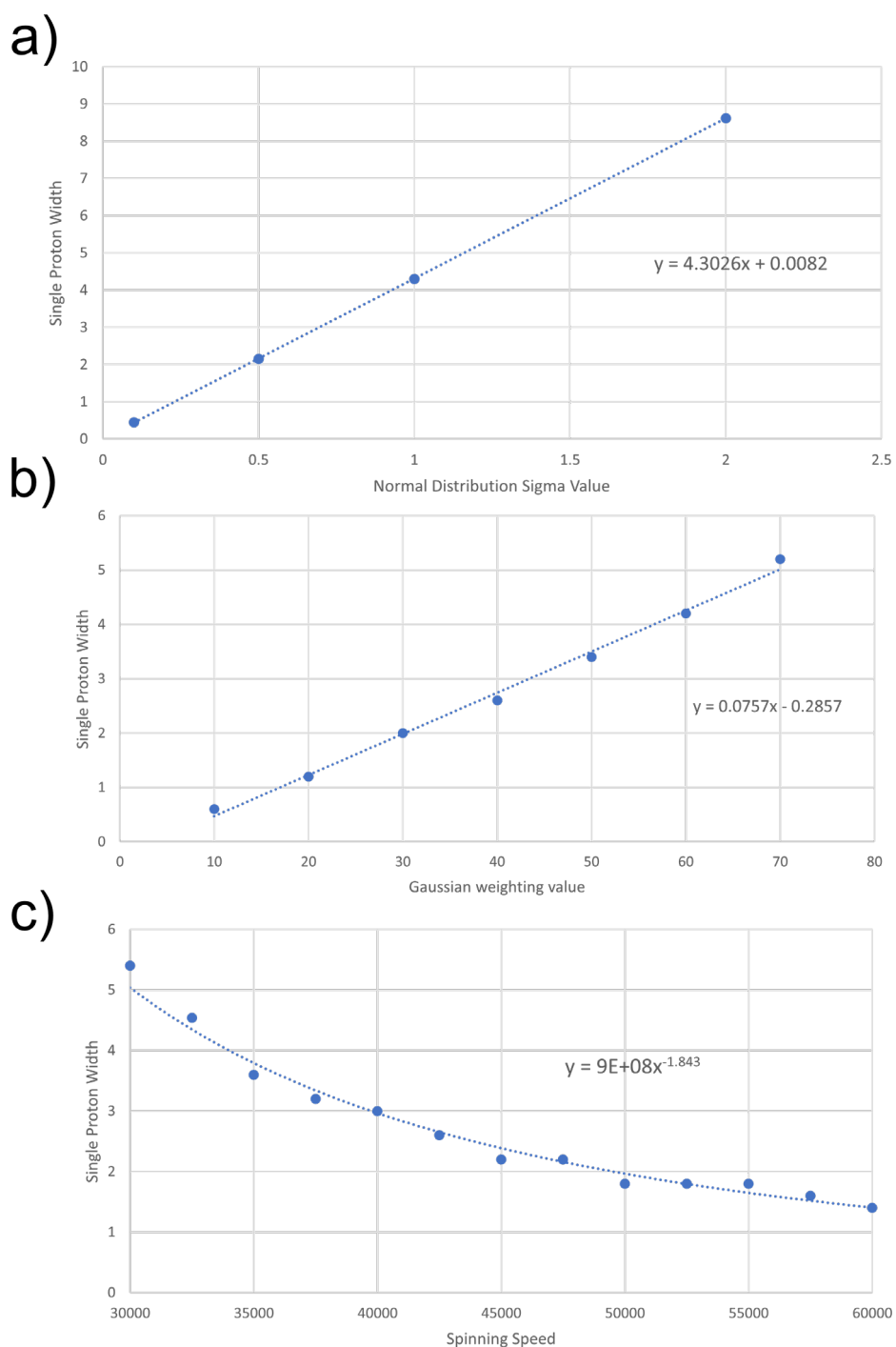


Figure 7-5, the graphs linking simulated peak widths to experimental ones. a) Correlations between sigma values and the width of a single simulated proton for obtaining the sigma for the normal distribution equation, b) Correlations between weighting values and the width of a single simulated proton for the required gaussian weighting value, c) the ratio of spinning speed to the width of a single proton in experimental data. This was obtained on a 1.3 mm rotor using a 400 MHz magnet. The sample chosen was L-tyrosine due to its ease of acquisition and it possesses a single high ppm proton that can easily be measured.

For these three graphs the equation of a line of best fit can be obtained. Since the y axis in all of these is the ppm width it is easy to find ratios between any two. This was added into Pantheon so that when setting up the simulations the user can input the experimental spinning speed and Pantheon will auto generate appropriate weighting values to best match simulated to experimental data.

7.4 Simulations vs experimental data

When putting into practice the steps previously outlined for the three naloxone forms and using the $R16_3^2$ pulse program a full 2D simulated data spectra is generated. These can then be overlaid with the experimental data; the result being seen below in Figure 7-6.

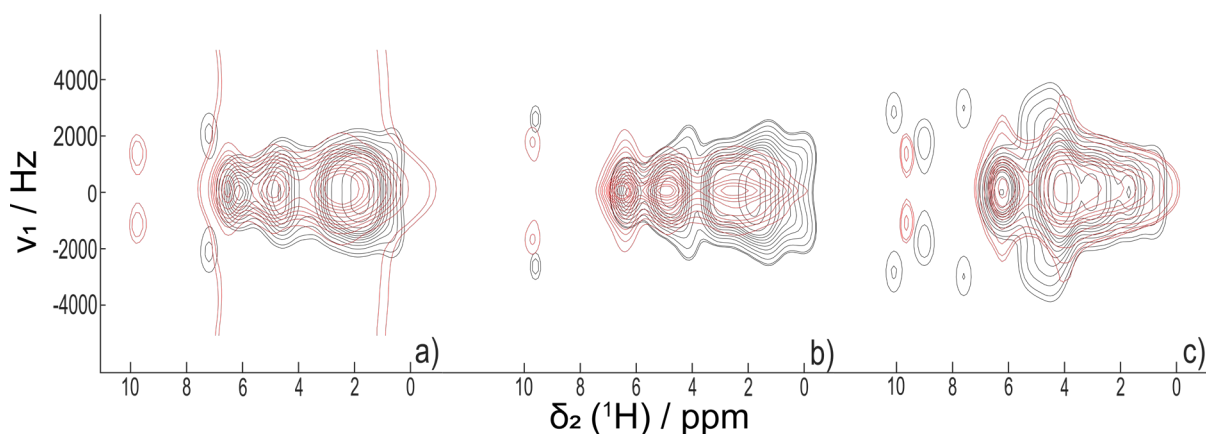


Figure 7-6, Comparison of experimental (red) to simulated (black) of ^1H MAS NMR isotropic-anisotropic correlation spectra, $R16_3^2$, of naloxone a) Freebase anhydrous b) Freebase monohydrate c) HCl dihydrate. The experimental spectra were recorded at 58 kHz on an 800 MHz magnet. This spinning speed gave a π pulse length of 3.2 μs . 4096 points were acquired in f_2 and 48 in f_1 . Each spectrum was acquired in 4 scans with each being made up of t_1 lasting 38.4 μs leading to a spectra width of 26042 Hz. The simulated components were generated using CSA and asymmetry values generated via CASTEP. The simulated spectra also had its settings matched to the equivalent values of the experimental.

The comparison shows the general agreement between experimental and computational. There is a general show of similarity between computed and experimental as can be seen in the main group of protons. The HCl form is still generally split into two sub-groups while the other two forms show three sub-groups of protons. The obvious differences isotropically come from the differences in the high ppm protons of the freebase anhydrous and HCl dihydrate forms. In the freebase anhydrous form CASTEP is unaware that this form is a mixture of two different forms and so cannot accurately predict the higher proton values which would be affected by differing hydrogen bonds. In the HCl form the difference between computational and experimental seems to be that CASTEP predicts the hydrogen bonds to have a greater impact on the protons than is actually seen. The three protons that are not grouped together are all involved in hydrogen bonds, which vary between the forms as seen in the literature and the crystal structures.

While the differences discussed so far focus more on the isotropic shifts, there are also some key anisotropic features. The main one of this being the large CSA values seen by the protons close to an isotropic shift of 4-5 ppm in the HCl form. These come from carbons 17-19, which, as already discussed, have their orientation changed due to the quaternary nitrogen. The CASTEP data allows us to see exactly which protons are the ones that cause this and can confirm the earlier assessment of their increased CSA values. This was shown previously in Figure 6-23, a) naloxone freebase monohydrate crystal structure. b) naloxone HCl dihydrate crystal structure. ^1H MAS NMR isotropic-anisotropic correlation spectra, $R16_3^2$, of naloxone c) Freebase monohydrate d) HCl dihydrate. Both were recorded at 58 kHz on an 800 MHz magnet. This spinning speed gave a π pulse length of 3.2 μs . 4096 points were acquired in f2 and 48 in f1. Each spectrum was acquired in 4 scans with each being made up of t_1 lasting 38.4 μs leading to a spectra width of 26042 Hz..

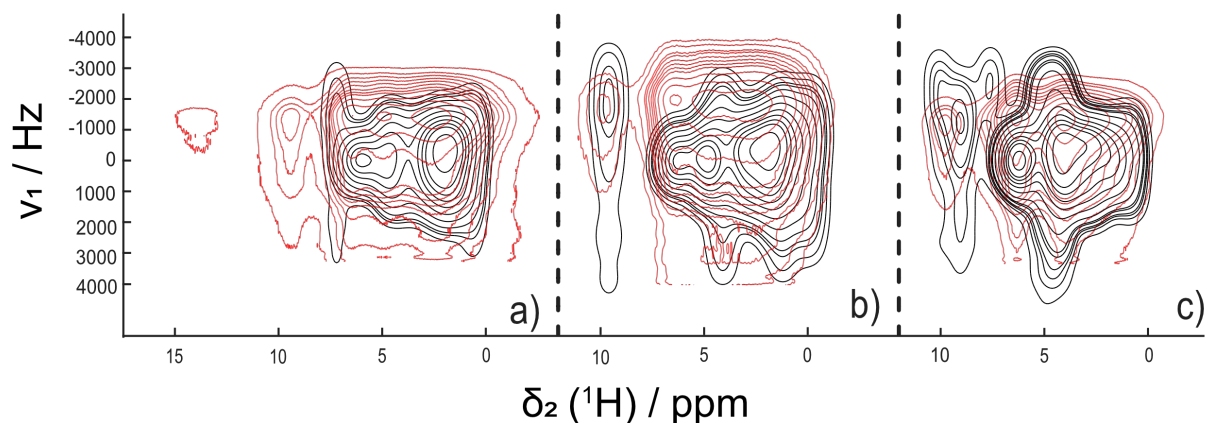


Figure 7-7, Comparison of experimental (red) to simulated (black) of ^1H MAS NMR isotropic-anisotropic correlation spectra, $SC2_2^1$, of naloxone a) Freebase anhydrous b) Freebase monohydrate c) HCl dihydrate. The experimental spectra were recorded at 46296 Hz on an 800 MHz magnet. This spinning speed was calculated to match $\pi/2$ pulse lengths of $1.5 \mu\text{s}$, 2π pulse lengths of $5.3 \mu\text{s}$ and 3π pulse lengths of $8 \mu\text{s}$. 10240 points were acquired in f_2 and 64 in f_1 . Each spectrum was acquired in 8 scans. The length of t_1 and therefore the size of the spectral width is governed by the increasing number of C sequences throughout the experiment. The simulated components were generated using CSA and asymmetry values generated via CASTEP. The simulated spectra also had its settings matched to the equivalent values of the experimental.

With the sign of the CSA visible in Figure 7-7, it is apparent that there is a greater difference between CASTEP and the experimental values. Looking at freebase anhydrous the most obvious difference of all is the 'missing' two protons in the simulated data. This was the case in the $R16_3^2$ simulated data as well, as it uses the same values, but it is more apparent in the $SC2_2^1$ sequence due to the new proton being visible.

Across all three forms there seems to be a trend of underestimating the size of the CSA and possibly the asymmetry as well. Across all three forms it is clear to see that the main body of protons has their δ_{aniso} between -1000 and -2000 Hz for the experimental data. In the CASTEP simulated data, the highest intensity in the F2 axis is centred around 0 Hz. When looking at the raw CASTEP values the cause of this becomes clear. Taking the Freebase monohydrate as

an example and focusing in on a section at 5ppm. The CASTEP predicted values in this area are protons 19 and 20. These have 5.18 and 5.03 isotropic ppm values and only CSA values of 5.75 and 3.36 respectively. This is a far cry from the experimental protons at this same location. Estimating by eye via repeated simulations, the CSA value of the net protons at this ppm is ~25 in experimental data, which is far higher than CASTEP predicted value in that area.

An exception to this is proton 1, from the C(3)-OH. This often has its CSA value more accurately estimated, and excluding the freebase anhydrous form, its isotropic value as well. This could possibly highlight the cause of the error being that CASTEP only correctly predicts higher values of CSA when the protons are part of hydrogen bonds. Despite the simulated and the experimental data being more closely aligned at this proton it is still certainly no exact match.

The use of CASTEP in work like this provides multiple benefits, despite its differences to experimental data it can still be used to assign certain protons as well as understand trends in groups.

7.5 Conclusion

We aimed to investigate the accuracy of CASTEP and its potential role in confirming experimental results. The study focused on verifying the ^{13}C assignment made through the use of the RI experiment. CASTEP was able to confirm the majority of carbon identities, exhibiting a minor discrepancy of only 2-5 ppm compared to the experimental values. However, there was a consistent overprediction for carbon 6 across all three forms. Despite this discrepancy, carbon 6 could be easily assigned using traditional chemical shift arguments and confirmed using the RI experiment. These findings indicate that CASTEP alone may not be sufficient for assigning a carbon spectrum due to its differing from experimental data, which could lead to misinterpretation of peaks. Nevertheless, it proves to be a valuable tool when used in conjunction with the RI experiment, as it can help confirm assignments and assist in cases where the experiment alone falls short.

When investigating the use of CASTEP for proton, as already discussed, SIMPSON was implemented due to the poor resolution of the spectra. When viewing protons that could be examined on their own this proved sufficient. Where this was not applicable the use of 2D simulation code was implemented. When evaluating the data there is a general isotropic agreement between experimental and simulated data. There are some key differences however, when looking at the HCl dihydrate form. A slight difference comes in this form where CASTEP predicts 3 protons above 7 ppm, when experimentally there is only one. These three are all -OH protons and are present in hydrogen bonds. One of them is the C3-O(H) which is only slightly overpredicted while the other two are C14-OH and one of the water molecules. This likely means that CASTEP believes there to be a stronger hydrogen bond formed here than what is actually present experimentally. CASTEP'S limitation with the

accuracy of proton comes from the fact that estimating the exact location of a proton is very difficult. Because of this a slight shift in where a proton is predicted in a bond, compared to where it is actually located could considerably change the isotropic and anisotropic values predicted. Because of this CASTEP is best used in conjunction with NMR data rather than as a sole source of identification.

The real difference between the simulated data and the experimental comes in the freebase anhydrous form. In this form, CASTEP can only predict the single, low strength, hydrogen bond in the pure freebase anhydrate. As the sample is actually a mixture of freebase and anhydrous the experimental data looks significantly different to the experimental.

Chapter 8: Pantheon

MATLAB code was written to be able to process simulated data and compare it to experimental data under the name Pantheon. The reason is to streamline the simulation process. Manual simulations involve changing values between each simulation and are a tedious process. An excel file can be imported which can contain any number of values to be. MATLAB was chosen as the base for writing this code due to the availability of signal processing add-ons which are essential in this line of work.

The process by which CASTEP values are converted to 1D and 2D simulations has already been given. This chapter will discuss the finer details of the code, such as: settings, limitations, challenges during development and future prospects. The process of producing the simulations involves making the 'CSA shape' of each proton and then broadening this across the isotropic axis, the full explanation of this process is given in 0. In the following figure the workflow for Pantheon can be seen. This is the sequence of operations that the settings available at the start of pantheon can manipulate.

Pantheon is the initial baseline structure to be able to simulate any 2D NMR experiment that can be done with SIMPSON. A previous member of the group made limited 2D simulations, but with no steps towards automation. Pantheon allows for a route to easy comparison of simulated to experimental data. This comes from the fact that pantheon, among other fine tune settings discussed later, comes down to simply selected the experiment and the CASTEP data and the full 2D simulated being generated.

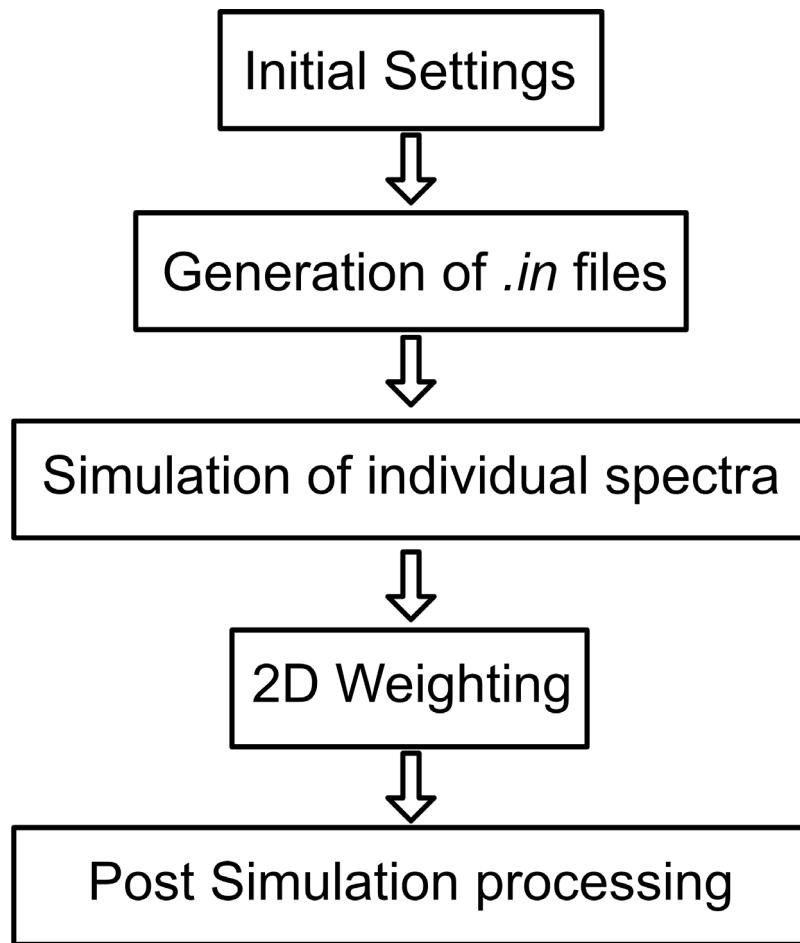


Figure 8-1 The base workflow for the Pantheon code.

8.1 Initial Settings for Pantheon

To streamline the usability of the code, a selection containing all the changeable parameters was required. This is the Initial settings section in the Figure 8-1 workflow. Without this, to be able to change between experiments or change variables would require multiple steps with increased likelihood of ‘breaking’ the code. Here will be discussed some of the settable parameters as well as some of the more advanced ones, for the full list of parameters please see appendix 1.

The initial settings primarily govern changes made to the *.in* file and selecting the experiment. The most basic of these are the setting of the magnet strength and spinning speed, these

simply have to be matched to the experimental values. This file is the input for SIMPSON to generate the simulations to be performed.

```
Magnet = 800;           % Magnet strength in MHz (Proton  
Frequency)  
Spinning_Speed = 46296; % 2D or 3D simulation spinning
```

Within the *.in* file there are two parameters that greatly affect the computational complexity of the simulation and therefore the amount of time it will take. These are the number of gamma angles and the crystal file. These two have a large effect on the total simulation time, though it is important to note the greatest effect comes simply from the number of atoms being simulated as this scales linearly. In the case of crystal files this work used only the zcw method for powder averaging [84]. Zcw is one of the possible methods for picking orientations for obtaining accurate powder averaging. This can be thought of as the number of variations of a powder that are averaged in the simulation. The value used throughout all simulations in this work was the zcw 143, this provided a good balance between high quality simulations and reasonable computation times. For example, a single proton, simulated using an $SC2\frac{1}{2}$ experiment at zcw 143 took 32.9 s, whereas the exact same at zcw 28565 took 6744.0 s and produced the exact same FID values. This is because the FIDs produced by SIMPSON contain a fixed number of values and so increasing the number of angles in the powder averaging beyond 143 causes no changes. When using zcw 20 the spectra produced hold little relation to what would be considered a typical powder pattern and so its use is reserved for fast simulations employed when testing new additions to the base code.

The other variable mentioned was gamma angles, this is the number of points per rotor period where the signal is sampled. This parameter has the same time scaling problem as the

crystal file number. Generally, a value of 5 is chosen as a balance of speed vs accuracy. In this case using the lowest crystal file value of 20 with a gamma angle of 5 takes 2.9 s, whereas the same crystal file for 32 gamma angles took 14.9 s. With both of these values there doesn't seem to be a difference with increasing them over 143 and 5 for crystal file number and gamma angles respectively, with the work carried out in this thesis. Gamma angles and crystal file packing value optimisation should follow a similar idea to convergence in CASTEP. The process of increasing the values of both until there is no change in the FID produced with increasing values.

```
Crystal_file = 143;           % Crystal file number. Typically
use 20, 143, 232, 615, 28656 NOTE takes longer
Gamma_Angle = 5;            % Number of angles tested. ~5-10
for quick analysis, ~32 for high quality NOTE takes longer
```

Selecting the experimental type comes next. This comprises choosing the pulse program to be performed as well as whether the experiment will be a 1D or a 2D experiment. There is also the option for the plot type with either 'Solo' or 'Compare' as the options. This is the option to compare the simulation generated to a specified set of experimental data or just to 'Solo' simulate. One thing to be noted is that the $R16_2^3$ sequence must be first processed in MATLAB separately and hence must be in the *.mat* file type. For other experiments the use of the command *totxt* can be used inside TopSpin to generate a *.txt* file which can be directly read in.

```
SimType = '2D';              % 1D or 2D
PlotMode = 'Compare';       % Solo or Compare
Experiment_Type = 'R1632';  % Currently Available: R1632
ExpFile = 'tyrosineR1632.mat'; % Name of the Bruker txt file(must
be 2D) or processed .mat file for R1632
SC212 C313
```

Depending on the choice of 1D or 2D the selection of the CASTEP values to be used is next. In the case of a 1D simulation then there is simply a settable parameter for the CSA and asymmetry values. Whereas in the case of 2D the name of the excel file containing the CASTEP data is chosen. Excel file inputs are used to allow for easy inputting of multiple nuclei to be simulated.

```
CSA = 18; % 1D simulated Chemical Shift
Anisotropy value
Aysm = 0.5; % 1D simulated Asymmetry
ExcelProtonData = 'H1HCl.xlsx'; % Name of the excel file containing
the CASTEP data (column 1: Iso, column 2: Aniso, column 3:
```

8.2 Simulating the spectra

When performing the simulations there is a possible error message that can occur, this being 'QNAN.' This is an error not documented in the SIMPSON literature but can be easily solved. This error occurs when SIMPSON is generating the FID for a given in file, instead of producing the values for the FID it simply gives 'QNAN.' If the exact same simulation is re-run, then there is a high probability the simulation will work as intended. This is where, in the code below, there is a section that includes `strfind(QNAN_text, 'QNAN')`. This simply searches the produced FID to see if it failed, if it did it reruns it and then checks again. This process occurs on repeat for every simulated atom until they all have succeeded. This error is inconsistent and seems to be hardware dependent.

```

list=length(ExcelProtonData);

for k = 1:list
    command = sprintf('simpson RRfiles/RR%g.in', k);
    status = system(command);
end
zero = 0;
for loop = 1:1000
    for i = 1:list
        QNAN_text=fileread(['RR', num2str(i), '.fid']);
        val = strfind(QNAN_text, 'QNAN');
        if val>zero
            fprintf 'Fail'
            disp (loop)
            fprintf 'Proton'
            disp (k)
            command = sprintf('simpson RRfiles/RR%g.in', i);
            status = system(command);
        end
    end
end

```

8.3 2D Weighting

8.3.1 'ND' vs 'Gauss'

For 2D weighting there are, as discussed in section 6.3, two different approaches. The first to be implemented was the Gauss way as this could be considered the more 'NMR' way as the weighting is done with similar ideas to weighting standard NMR data. There however is a slight issue with this technique. Due to the nature of inverse Fourier transforming, Gaussian weighting and Fourier transforming back there is a baseline error. This can only be seen when viewing very low contour levels but is definitely present.

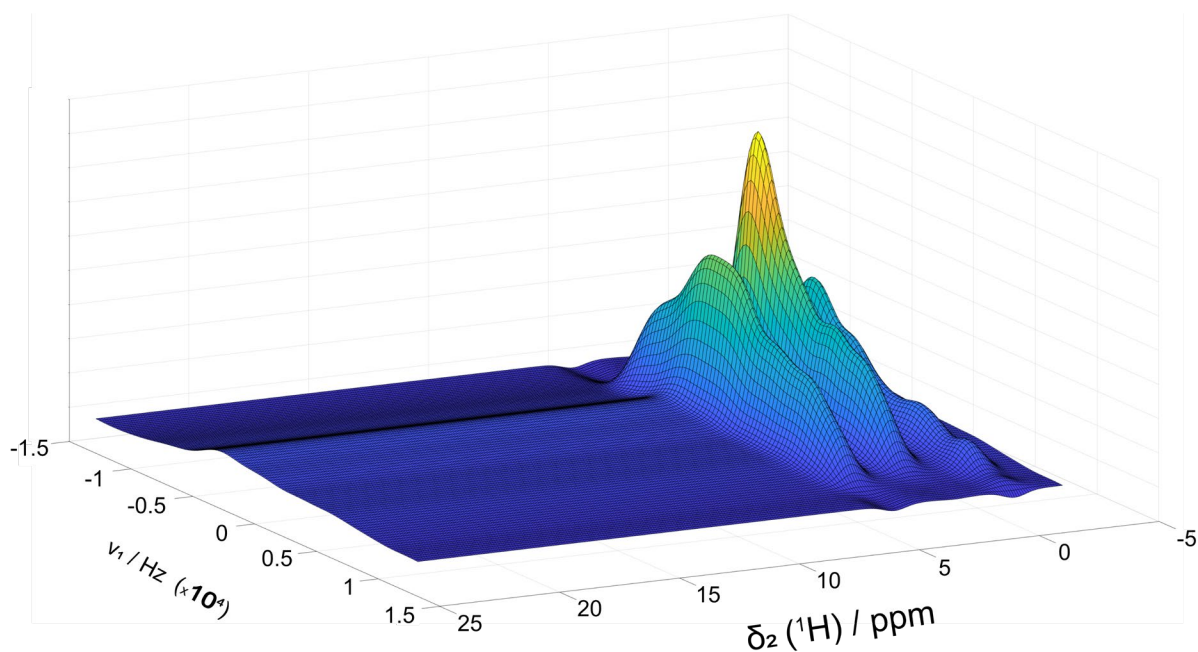


Figure 8-2, a MATLAB generated surf plot of three example protons at 0, 2.5 and 5 ppm showing the 'Gauss' approach to 2D and the baseline error.

When looking at the above figure the baseline error can be seen clearly when looking at the region of 10-25 ppm. It is clear to see this region is not flat as would be expected when there is no proton located in the region. To combat this baseline error a section approach was theorized. This way was dubbed the 'ND' way and was born from the assistance of a friend Matt Milward who helped conceptualise the idea. The 'ND' was, as previously discussed involves using normal distributions to give width. A mathematical explanation this is given in the coming pages.

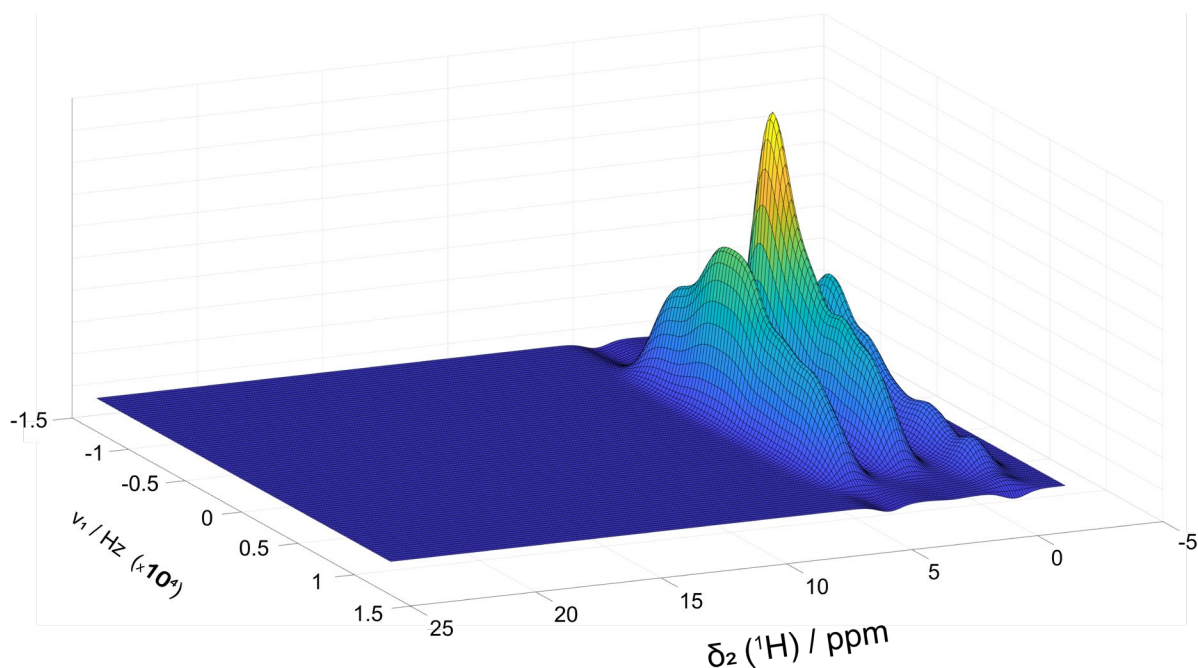


Figure 8-3, a MATLAB generated surf plot of three example protons at 0, 2.5 and 5 ppm showing the 'ND' approaching to 2D.

Comparing the two approaches, it becomes evident that by using identical parameters and data, the 'ND' approach eliminates the baseline error. This error is believed to come from the truncation of the Gaussian weighting caused by the imposed limit of the spectral width. This ultimately led to this approach being used in all simulations, though this difference would only be visible when considering very low contour levels. This is less of an issue than might be originally considered as simulated data does not give 'low signal' protons like experimental data does. An example of this 'low signal' could be the degraded freebase anhydrous proton peak ~12 ppm as depicted in Figure 6-25. Consequently, scrutinizing the lowest contour levels where this error might manifest is typically unnecessary.

The code that provides the 'ND' weighting is given below. This section creates the 2D set of 'points' based on the width of the simulated powder patterns contained in 'data' vs 270. 270

is chosen as this allows for isotropic ppm ranges of -2 to 24.9 in increments of 0.1 as shown in the code.

```

%% Weights data

points = zeros(length(data{1,1}),270);
X = -2:0.1:24.9;
X = transpose(X);

%% Add X slices
for i = 1:length(isofm)
    slice = data{i,1};
    insertpoint = dsearchn(X,isofm(i));
    points(:,insertpoint) = slice;
end
sumslice = 1:length(X);
sumslice = sumslice*0;

%% Weights Y slices
for i = 1:length(slice)
    sumslice = sumslice*0;
    for k = 1:length(isofm)
        for l = 1:length(X)
            alpha = data{k,1}(i,1);
            SliceY(l) = alpha*exp(-(X(l) - isofm(k) ) ^2
/(2*(sigma^2)));
        end
        sumslice = sumslice + SliceY;
    end
    points(i,:) = sumslice;
end
Z = points;

```

The code then extracts the simulated 1D spectra and puts them into 'points' based on the isotropic ppm of that specific proton.

$$y = \alpha e^{\frac{-(x(l)-\text{Isofm}(k))^2}{2\sigma^2}}$$

The above equation is from the previous code section, but in a more traditional mathematical presentation. This is what is used to give the individual single simulations width in the x axis, the isotropic axis. This is effectively a normal distribution equation. In this case alpha is the height of the peak, taken straight from the data. The x value works across the whole isotropic

range given, iterated by l , and has its distance from the current slice calculated by squaring the x value minus l_{sofm} , integrated by k , which is the isotropic value from CASTEP that the SIMPSON simulation is inserted onto x , this is the F2 axis. This difference squared is then divided by two times σ squared. As mentioned in section 6.3, ' σ ' is calculated based on a given experimental spinning speed. Each simulated spectra is broadened in turn and added to 'sumslice.' A visual representation of this can be seen below.

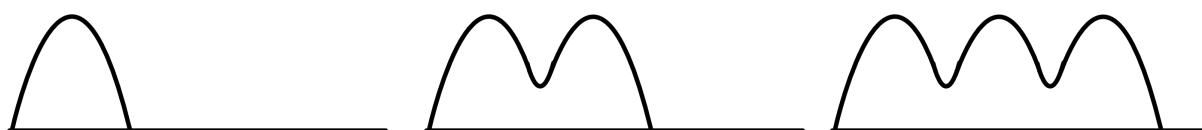


Figure 8-4. Visual representation of how the simulation broadening is built up.

This is why l_{sofm} is iterated by k , which is the number of 1D simulations that are being combined. After all iterations of k , the whole process repeats, as iterated by i . This process of iterating k , l and l can be seen in the line: $\alpha = \text{data}\{k,l\}(i,l)$ where the α , the height at the given point, is extracted from the overall dataset by taking the simulated spectra, k , along l . Then once completed the whole process shifts by one value of i so that every F1 axis is done.

8.3.2 Mirrored FID

One problem that was encountered during the processing of the data was a mirrored FID. This comes as a sub problem of using the 'Gauss' method of weighting data. In NMR experiments, the FID signal appears as a complex wave that gradually diminishes into noise. When performing the inverse Fourier Transform on the FID, a mirrored structure is observed in the time domain. This mirroring arises from the conjugate symmetry property of the Fourier

Transform, where positive and negative angular frequencies are complex conjugates of each other:

$$F(-\omega) = [F(\omega)]^*$$

It is important to note that only half of the mirrored FID is required to reconstruct the original spectrum. This is due to the redundant nature of the conjugate symmetry. By considering only half of the mirrored FID and applying the Fourier Transform, the resulting spectrum will remain unchanged from the original spectrum.

Therefore, when applying any weighting or filtering functions to the FID, it is sufficient to consider only half of the mirrored portion, effectively disregarding the redundant mirrored part of the FID.

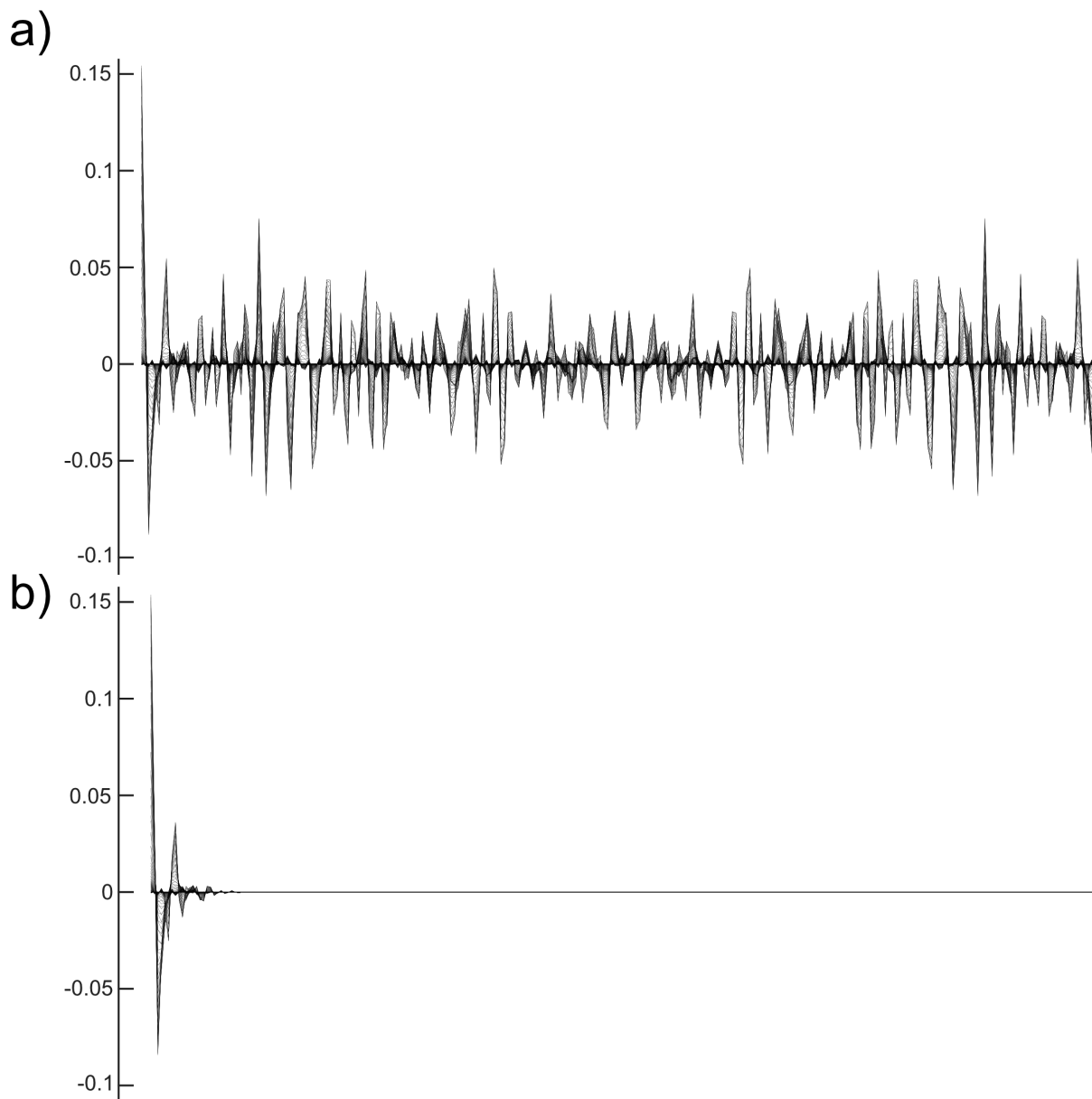


Figure 8-5, An overlay of all 96 mirrored FID's a) prior to weighting b) post weighting, of a simulation of naloxone freebase anhydrous data.

The above figure also demonstrates that the more weighted a spectrum the simpler the FID becomes. This is because single point wide signals on a spectrum require far more different compiled sine waves to produce when compared to much broader signals.

8.4 Post Simulation processing

8.4.1 Artifact Removal

In this case 'artifact' generally refers to dipole-dipole coupling which is not removed due to not spinning fast enough. This manifests, in the case of dipole-dipole coupling, as a shoulder or bump centred at 0 Hz. While NMR experiments normally attempt to remove this via MAS it is difficult to do so, due to the limitations of spinning speed.

The process by which this setting works is by smoothing over a given width centralised at a given point. Both can be chosen freely, based on the degree of smoothing required. This editing of data while not for the purpose of publishing can help match experimental data to its simulated counterpart. Depending on the cause and the size of an artifact it can make discerning the CSA and asymmetry values of experimental data challenging. This could be important in a situation where there is not access to CASTEP values and are trying to calculate CSA and asymmetry values based on repeated simulations. As can be seen below in Figure 8-6, 'Artifact Removal' can be used to smooth over sections of a spectrum.

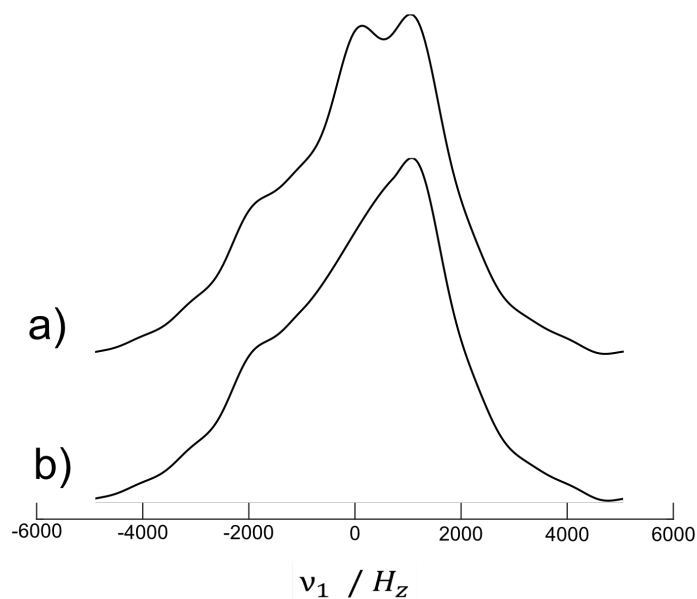


Figure 8-6, a cross section at 12 ppm of ^1H MAS NMR isotropic-anisotropic correlation spectra, SC2_2^1 , of *l*-tyrosine HCl. MAS rate of 36 kHz. a) un-altered cross section b) cross section with artifact removal on and correctly set.

While evidently use full it is essential to acknowledge that artifact removal introduces a significant dilemma concerning data integrity. This tool has the potential to be misused, altering data to present a more favourable image than reality, especially in research publications. To maintain the credibility of research outputs using Pantheon, it is imperative that this specific function is used in a considered manner.

8.4.2 DC Correction

DC correction is a setting that only affects $R16_2^3$ simulations. Because the simulation does not account for T_1 relaxation there is the presence of dipole-dipole coupling present as a peak in the centre of the spectrum. By taking a given value, DC, of points at the end of the FID to be averaged and subtracted from the centre of the spectrum the dipole-dipole coupling peak can be variably lower. Using a manual iterative process, you then match the simulated spectra to the experimental one so that they have the same level of dipole-dipole coupling.

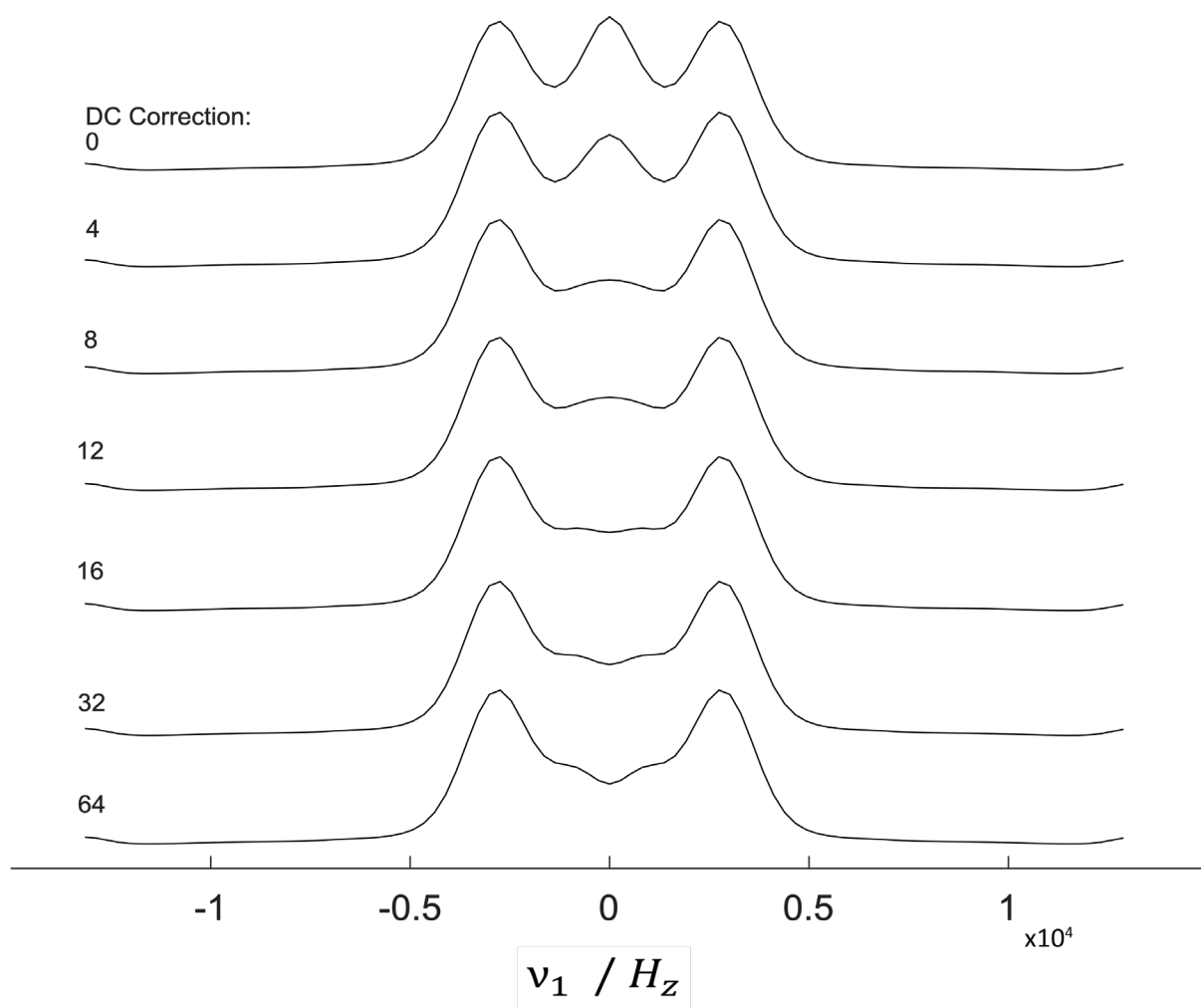


Figure 8-7, $R16_2^3$ simulation of a single proton using ζ of 25 and η of 0.1, 800 MHz, 50 kHz spinning speed. The value of DC correction is varied while all other parameters are kept fixed.

8.5 Easy Pantheon

With the aim of making the software as accessible as possible, an easy-to-use version was created. With the standard code there are, currently, twenty-six different options that can be chosen from. With someone unfamiliar with the basic workings of the code or even the NMR behind the code this could lead to confusion. To combat this, the ability to simply select a limited number of options from a dropdown menu leads to better user experience. This option does not allow for all parameters to be changed as in the standard version but streamlines the process by choosing standard parameters that will be acceptable in the majority of circumstances. An example of this being the choice of gamma angles and crystal file type as previously mentioned.

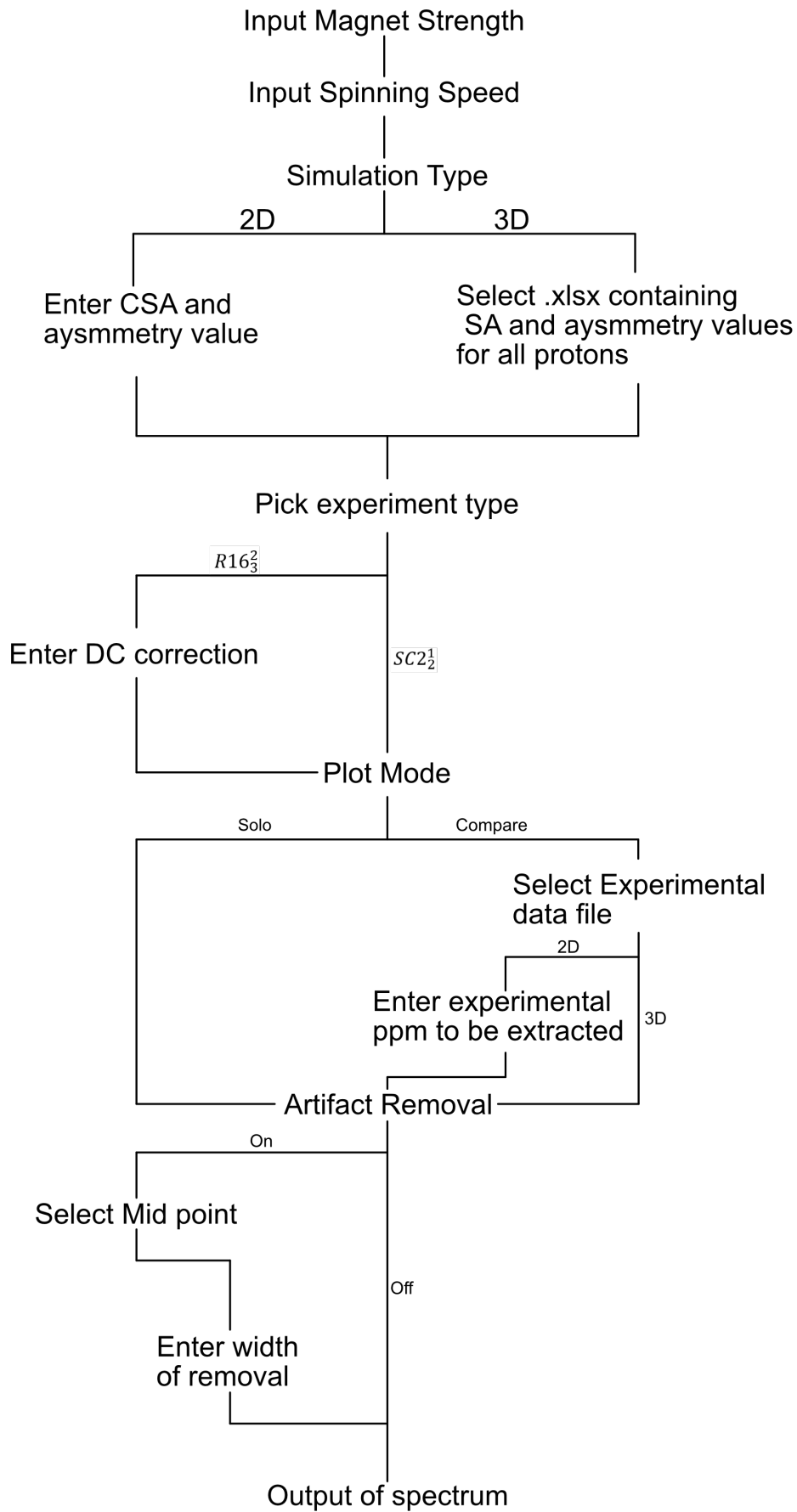


Figure 8-8, the flow chart of options for 'Easy Pantheon'

As can be seen in the above figure, what would be considered the basic options are present. This allows for someone with no experience with MATLAB or SIMPSON to be able to perform a simulation and compare it to experimental data.

8.6 Future additions to the code

While Pantheon in its current state works as intended, there is still much that can be added. There are two main ideas: the ability to run any pulse program given and to be able to obtain CSA and asymmetry values from experimental data. These two ideas will be discussed here including efforts already made and potential obstacles.

8.6.1 Expanding Pantheon

This idea has obvious merits where any experimental data could in theory be compared to its CASTEP equivalent. One of the limitations of this is the format of the pulse program required. When using TopSpin from Bruker, the pulse programs are written in the Bruker pulse programming language, whereas for SIMPSON they are required to be in the tcl language. To translate between the two a knowledge of both is required. The difficulty of writing a program to convert between the two was too challenging to have been given serious consideration, though the basis has been investigated. For simplicity the easiest way of converting between the two would be to be able to write a program that reads not the raw Bruker pulse program but to read the graphical representation instead. This can be thought of as a common language point for both.

In a more straightforward approach Pantheon could simply be written to include more pulse programs. Using the groundwork already laid out adding in a new pulse program would be trivial as long as SIMPSON is able to simulate it. An example of one that could be added simply

are any additional symmetry-based recoupling experiments as they would follow the general ideas already in use. Given time any of the experiments performed in this thesis could be likely added, namely a simple 1D proton experiment, a ^{13}C experiment and a refocused INADEQUATE. In a similar vein to 'Easy Pantheon' which comes with a full guide attached to it, a guide on implementing new pulse programs could be compiled, allowing for operators to add their own desired experiments.

The other pathway for the expansion of Pantheon involves the incorporation with Topspin. This could come in two forms, one being the complete rewriting of pantheon in python so that the native python interpreter in Topspin could be used to run Pantheon from within Topspin. The other, simpler path, is to bypass the need to 'totxt' the data in topspin and simply read in the 1r or 2rr files that contain the plotted data of Topspin. While simpler in concept this path presents possible issues regarding processing and may require the ability to process experimental data inside of Pantheon. If this were the case then the route of incorporating Pantheon into topspin would be preferable.

8.6.2 Obtaining CSA values from experimental data.

The ability to extract CSA and asymmetry values from experimental data can be thought of as the reverse of the code that has been discussed so far. A previous PhD student in the group, Miah, as well as Kobayashi et al [69]. have made efforts into this previously with some success. However, with both attempts there have been caveats and limitations. A caveat concerning Kobayashi et al. is that their experimental cross section was passed through DMFit, where it was fitted to a model CSA pattern and then this was what was analysed.

When attempting to create a similar version of this the decision was made to forgo this additional step in an attempt to limit the opportunity of data manipulation. My approach was to use the following code:

```
simalarityscore = 0;
for i = 1:length(ExperimentalY)
    diffsquared = (ExperimentalY(i,1)-SimulatedY(i,1))^2;
    score(i) = diffsquared;
    simalarityscore = simalarityscore + diffsquared;
end
SIM_Score = mean(score);
```

This simply boils down to obtaining a mean value for the differences between two lines, with one being the experimental (ExperimentalY) and the other simulated spectra (SimulatedY). The lower the value, the better the match is between the two.

One important note to make is that the experimental data and the simulated data contain a different number of points that they are made up of. This was solved by combining all points together and extrapolating the original data across the new line. This caused no change in the spectrum outside of making sure that the y points to be measured had the same x values.

This section of code was simply inserted into the end on Pantheon and then the whole script was transformed into a function. This allows for the use of a function minimalization tool to be used. By having the function input as an estimated value of CSA and asymmetry, and the output as *SIM_Score* the function can be minimalised to find values of CSA and asymmetry that best matched a given cross section of experimental data.

Functionally this worked exactly as intended and would produce values for any given cross section. The issue is with the practical difference between experimental and simulated data. Experimental data is inherently noisy also less narrow. This makes obtaining a *SIM_Score*

value of anything close to zero impossible. When comparing what the minimised function estimated the CSA and asymmetry values to be compared to the experimental cross section the two did not match up. The reason being that the simulated one was always larger i.e., it had predicted a larger CSA value in an attempt to minimise the distance between the naturally wider experimental data and the narrower simulation. The outcome of this is that there is still more work needed in this feature for it to be useful in NMR analysis.

Chapter 9: Summary

This work investigated three solvates of naloxone using various solid-state NMR techniques. This allowed for differentiation of these solvate forms as well as investigation into some of the structural differences that separate these forms. The first key discovery was that naloxone freebase anhydrous degrades overtime due to moisture in the air. This is a common occurrence in anhydrous chemicals, but it meant that analysis of the powder was actually analysis of the anhydrous and monohydrate forms together.

The carbon analysis played a critical role in the identification of the degradation of one of the samples. The refocused INADEQUATE's performed allowed for the accurate assignment of the majority of carbons. Complete assignment of a solvate form from a single experiment was shown to be possible when examining the freebase anhydrous form due to the high number of scans performed. On other forms it was possible to assign the carbons by making use of the experimental data as well as the CASTEP data. While it was demonstrated that carbon can be used to differentiate the forms, this made use of DNP which involves the use of a solvent for the radical. In this work it was found that the use of this solvent changes two of the forms upon its addition. The outcome is likely a higher hydration form of naloxone freebase that has been undocumented in literature as of writing this work. While XRD could likely shed some light onto what exactly comprises this new form it would likely be difficult to isolate a solid version of this higher hydration form. This work highlights the usefulness of the RI experiment to analyse complex pharmaceutical compounds. Naloxone contains many carbons in similar environments, meaning without the use of experiment like a RI accurate assignment of the carbons would prove unreliable. Identifying the exact carbon responsible for a peak is key to drug design and discovery.

Symmetry based recoupling techniques have been widely implemented in solid state NMR due to the ability to view structural information normally lost via MAS. In this work we showed how the conversion of a tertiary nitrogen to a quaternary nitrogen caused the movement of an aliphatic chain and the subsequent dramatic increase in anisotropy. This leads to an easy way to differentiate the forms. This technique could likely be applied for other uses such as assessing polymorphic differences or the formation of co-crystals. This work illustrates how these techniques can be used to not only differentiate between different solvate forms but also allows for probing of structural differences between the forms. The shifting of the aliphatic chain caused by the introduction of the additional proton provided by the HCl is a clear example of the possible applications of these recoupling techniques. Its increased CSA values is clearly visible in the spectra. Recoupling techniques like this also allow for a better analysis of the effects hydrogen bonds have on a proton. The proton located ~ 9.8 ppm shifts slightly isotopically between the three forms but it also changes its CSA value based on the hydrogen bond it is involved in. These CSA values can be used to observe the differences suggested by the crystal structures, in NMR data.

CASTEP proved to be a valuable tool for confirming the assignment of the carbons and also for confirming which protons were affected by the change in the nitrogen. Pantheon allows for the automated generation of 2D simulations. While currently only functioning for CSA recoupling experiments it has possible applications for most 1D and 2D experiments. The ultimate goal would be, once equipped with CASTEP data, the utility to provide simulations to accompany any experiments. There exists a path in NMR to simultaneous processing of simulation and experimental data. Because both can be fundamentally seen as the same source, and FID, both can ultimately be processed in the same way. Integration of simulations within Topspin would allow of the use of Pantheon, or other similar scripts once written, to

make use of the preexisting processing found in Topspin but for simulations. It is important to recognize the limitations of the study with respect to time for further developing the code, obtaining more experimental data, as well as the availability of naloxone forms.

References

- [1] R.W. Chan, J.Y.C. Lau, W.W. Lam, A.Z. Lau, *Magnetic Resonance Imaging*, Encyclopedia of Biomedical Engineering, Elsevier, (2019), p. 574-587.
<https://doi.org/10.1016/B978-0-12-801238-3.99945-8>.
- [2] A. Zhuravleva, D.M. Korzhnev, Protein folding by NMR, *Prog. Nucl. Magn. Reson. Spectrosc.*, 100 (2017), p. 52–77. doi:10.1016/j.pnmrs.2016.10.002.
- [3] G.F. Pauli, S.-N. Chen, D.C. Lankin, J. Bisson, R.J. Case, L.R. Chadwick, T. Gödecke, T. Inui, A. Kronic, B.U. Jaki, J.B. McAlpine, S. Mo, J.G. Napolitano, J. Orjala, J. Lehtivarjo, S.-P. Korhonen, M. Niemitz, Essential Parameters for Structural Analysis and Dereplication by ^1H NMR Spectroscopy, *J. Nat. Prod.*, 77 (2014), p. 1473–1487.
<https://doi.org/10.1021/np5002384>.
- [4] Peter Hore, *Nuclear Magnetic Resonance*, Oxford University Press, First ed., 1995.
- [5] D. Apperley, R. Harris, P. Hodgkinson, *Solid-State NMR: Basic Principles and Practice*, Momentum Press, 2012. <https://doi.org/10.5643/9781606503522>.
- [6] E.D. Becker, A Brief History Of Nuclear Magnetic Resonance, *Anal. Chem.*, 65 (1993), p. 295A-302A. <https://doi.org/10.1021/ac00054a716>.
- [7] J.M.B. Kellogg, I.I. Rabi, N.F. Ramsey, J.R. Zacharias, The Magnetic Moments of the Proton and the Deuteron. The Radiofrequency Spectrum of ^2H in Various Magnetic Fields, *Phys. Rev.*, 56 (1939), p. 728. <https://doi.org/10.1103/PhysRev.56.728>.
- [8] F. Bloch, W.W. Hansen, M. Packard, Nuclear Induction, *Phys. Rev.*, 69 (1946), p. 127.
<https://doi.org/10.1103/PhysRev.69.127>.

- [9] E.M. Purcell, H.C. Torrey, R. v. Pound, Resonance Absorption by Nuclear Magnetic Moments in a Solid, *Phys. Rev.*, 69 (1946), p. 37.
<https://doi.org/10.1103/PhysRev.69.37>.
- [10] E.R. Andrew, L.F. Farnell, T.D. Gledhill, Resolved Spin Multiplets in the Nuclear Magnetic Resonance Spectra of Solids, *Phys. Rev. Lett.*, 19 (1967), p. 6.
<https://doi.org/10.1103/PhysRevLett.19.6>.
- [11] I.J. Lowe, Free Induction Decays of Rotating Solids, *Phys. Rev. Lett.*, 2 (1959), p. 285.
<https://doi.org/10.1103/PhysRevLett.2.285>.
- [12] E. Luchinat, L. Barbieri, M. Cremonini, L. Banci, Protein in-cell NMR spectroscopy at 1.2 GHz, *J. Biomol. NMR*, 75 (2021), p. 97-107. <https://doi.org/10.1007/s10858-021-00358-w>.
- [13] Y. Nishiyama, Fast magic-angle sample spinning solid-state NMR at 60–100 kHz for natural abundance samples, *Solid State Nucl. Magn. Reson.*, 78 (2016), p. 24-36.
<https://doi.org/10.1016/j.ssnmr.2016.06.002>.
- [14] E Andrew, Magic angle spinning in solid state NMR spectroscopy, *Philosophical Transactions of the Royal Society of London. Series A, Math. Phys.*, 299 (1981).
<https://doi.org/10.1098/rsta.1981.0032>.
- [15] E.R. Andrew, E. Szczesniak, A historical account of NMR in the solid state, *Prog. Nucl. Magn. Reson. Spectrosc.*, 28 (1995), p. 11–36. [https://doi.org/10.1016/0079-6565\(95\)01018-1](https://doi.org/10.1016/0079-6565(95)01018-1).

- [16] S. Penzel, A. Oss, M.-L. Org, A. Samoson, A. Böckmann, M. Ernst, B.H. Meier, Spinning faster: protein NMR at MAS frequencies up to 126 kHz, *J. Biomol. NMR*, 73 (2019), p. 19-29. <https://doi.org/10.1007/s10858-018-0219-9>.
- [17] E.H. Lee, A practical guide to pharmaceutical polymorph screening and selection, *Asian J. Pharm. Sci.*, 9 (2014), p. 163-175. <https://doi.org/10.1016/j.ajps.2014.05.002>.
- [18] R. Censi, P. Di Martino, Polymorph Impact on the Bioavailability and Stability of Poorly Soluble Drugs, *Molecules*, 20 (2015), p. 18759-18776. <https://doi.org/10.3390/molecules201018759>.
- [19] A.J. Florence, A. Johnston, P. Fernandes, N. Shankland, K. Shankland, An automated platform for parallel crystallization of small organic molecules, *J. Appl. Crystallogr.*, 39 (2006), p. 922-924. <https://doi.org/10.1107/S0021889806040921>.
- [20] W. Liebenberg, M.M. de Villiers, D.E. Wurster, E. Swanepoel, T.G. Dekker, A.P. Lötter, The Effect of Polymorphism on Powder Compaction and Dissolution Properties of Chemically Equivalent Oxytetracycline Hydrochloride Powders, *Drug Dev. Ind. Pharm.*, 25 (1999), p. 1027-1033. <https://doi.org/10.1081/DDC-100102265>.
- [21] D.S. Moyo, E.M. van der Merwe, M. Rademeyer, F.P. Malan, M.T. Atanasova, A.B. Mapossa, W.W. Focke, Characterizing the thermal phase behaviour of fipronil polymorphs, *J. Therm. Anal. Calorim.*, 148 (2023), p. 6761-6777. <https://doi.org/10.1007/s10973-023-12198-x>.
- [22] E. Jurczak, A.H. Mazurek, Ł. Szeleszczuk, D.M. Pisklak, M. Zielińska-Pisklak, Pharmaceutical Hydrates Analysis—Overview of Methods and Recent Advances, *Pharmaceutics*, 12 (2020), p. 959. <https://doi.org/10.3390/pharmaceutics12100959>.

- [23] ATLAS Collaboration, Evidence for the spin-0 nature of the Higgs boson using ATLAS data, *Phys. Lett. B*, 76 (2013), p. 120–144.
<https://doi.org/10.1016/j.physletb.2013.08.026>
- [24] O.L. de Lange, R.E. Raab, Ladder operators for orbital angular momentum, *Am. J. Phys.*, 54 (1986), p. 372-375. <https://doi.org/10.1119/1.14625>.
- [25] Timothy Claridge, *High-Resolution NMR Techniques in Organic Chemistry*, Elsevier, (2016) <https://doi.org/10.1016/C2015-0-04654-8>.
- [26] James Keeler, *Understanding NMR Spectroscopy*, John Wiley & Sons Ltd; First ed., (2005).
- [27] M. Weingarth, M. Baldus, *Advances in Biological Solid-State NMR and Membrane-Active Peptides*, RSC., (2014): p. 1–17. <https://doi.org/10.1039/9781782627449-00001>.
- [28] M. Duer, *Solid-State NMR Spectroscopy Principles and Applications*, Wiley, (2001), <https://doi.org/10.1002/9780470999394>.
- [29] S. Cadars, J. Sein, L. Duma, A. Lesage, T.N. Pham, J.H. Baltisberger, S.P. Brown, L. Emsley, The refocused INADEQUATE MAS NMR experiment in multiple spin-systems: Interpreting observed correlation peaks and optimising lineshapes, *J. Magn. Reson.*, 188 (2007), p. 24-34. <https://doi.org/10.1016/j.jmr.2007.05.016>.
- [30] J.A.S. Smith, Nuclear quadrupole resonance spectroscopy. General principles, *J. Chem. Educ.*, 48 (1971), p. 39. <https://doi.org/10.1021/ed048p39>.
- [31] M.H. Levitt, *Spin Dynamics: Basics of Nuclear Magnetic Resonance*, John Wiley & Sons Ltd; First ed., 2001.

- [32] M. Bak, J.T. Rasmussen, N.C. Nielsen, SIMPSON: A General Simulation Program for Solid-State NMR Spectroscopy, *J. Magn. Reson.*, 147 (2000), p. 296-330.
<https://doi.org/10.1006/jmre.2000.2179>.
- [33] F. Bloch, Nuclear Induction, *Phys. Rev.*, 70 (1946), p. 460.
<https://doi.org/10.1103/PhysRev.70.460>.
- [34] D. Reichert, G. Hempel, Receiver imperfections and CYCLOPS: An alternative description, *Concepts Magn. Reson.*, 14 (2002), p. 130-139.
<https://doi.org/10.1002/cmr.10004>.
- [35] Q.Z. Ni, E. Daviso, T. v. Can, E. Markhasin, S.K. Jawla, T.M. Swager, R.J. Temkin, J. Herzfeld, R.G. Griffin, High Frequency Dynamic Nuclear Polarization, *Acc. Chem. Res.*, 46 (2013), p.1933–1941. <https://doi.org/10.1021/ar300348n>.
- [36] S. Hediger, D. Lee, F. Mentink-Vigier, G. De Paëpe, MAS-DNP Enhancements: Hyperpolarization, Depolarization, and Absolute Sensitivity, *EMagRes.*, 7 (2018), p. 309-322. <https://doi.org/10.1002/9780470034590.emrstm1559>.
- [37] L.R. Becerra, G.J. Gerfen, R.J. Temkin, D.J. Singel, R.G. Griffin, Dynamic nuclear polarization with a cyclotron resonance maser at 5 T, *Phys. Rev. Lett.*, 71 (1993), p. 3561. <https://doi.org/10.1103/PhysRevLett.71.3561>.
- [38] M. Blank, P. Borchard, S. Cauffman, K. Felch, M. Rosay, L. Tometich, Experimental demonstration of a 527 GHz gyrotron for dynamic nuclear polarization, in: 2013 Abstracts IEEE International Conference on Plasma Science (ICOPS), IEEE, 2013, p. 1-1.
<https://doi.org/10.1109/PLASMA.2013.6635226>.

- [39] D. Lee, E. Bouleau, P. Saint-Bonnet, S. Hediger, G. De Paëpe, Ultra-low temperature MAS-DNP, *J. Magn. Reson.*, 264 (2016), p. 116-124.
<https://doi.org/10.1016/j.jmr.2015.12.010>.
- [40] M. Lelli, S.R. Chaudhari, D. Gajan, G. Casano, A.J. Rossini, O. Ouari, P. Tordo, A. Lesage, L. Emsley, Solid-State Dynamic Nuclear Polarization at 9.4 and 18.8 T from 100 K to Room Temperature, *J. Am. Chem. Soc.*, 137 (2015), p. 14558-14561.
<https://doi.org/10.1021/jacs.5b08423>.
- [41] P. Berruyer, S. Björgvinsdóttir, A. Bertarello, G. Stevanato, Y. Rao, G. Karthikeyan, G. Casano, O. Ouari, M. Lelli, C. Reiter, F. Engelke, L. Emsley, Dynamic Nuclear Polarization Enhancement of 200 at 21.15 T Enabled by 65 kHz Magic Angle Spinning, *J. Phys. Chem., Lett* 11 (2020), p. 8386-8391.
<https://doi.org/10.1021/acs.jpcllett.0c02493>.
- [42] S.R. Chaudhari, D. Wisser, A.C. Pinon, P. Berruyer, D. Gajan, P. Tordo, O. Ouari, C. Reiter, F. Engelke, C. Copéret, M. Lelli, A. Lesage, L. Emsley, Dynamic Nuclear Polarization Efficiency Increased by Very Fast Magic Angle Spinning, *J. Am. Chem. Soc.*, 139 (2017), p. 10609-10612. <https://doi.org/10.1021/jacs.7b05194>.
- [43] A.S. Lilly Thankamony, J.J. Wittmann, M. Kaushik, B. Corzilius, Dynamic nuclear polarization for sensitivity enhancement in modern solid-state NMR, *Prog. Nucl. Magn. Reson. Spectrosc.*, 102–103 (2017), p. 120–195.
<https://doi.org/10.1016/j.pnmrs.2017.06.002>.
- [44] Y. Matsuki, T. Maly, O. Ouari, H. Karoui, F. Le Moigne, E. Rizzato, S. Lyubenova, J. Herzfeld, T. Prisner, P. Tordo, R.G. Griffin, Dynamic Nuclear Polarization with a Rigid

- Biradical, *Angew. Chem. Int. Ed.*, 48 (2009), p. 4996–5000.
<https://doi.org/10.1002/anie.200805940>.
- [45] K.-N. Hu, H. Yu, T.M. Swager, R.G. Griffin, Dynamic Nuclear Polarization with Biradicals, *J. Am. Chem. Soc.*, 126 (2004), p. 10844–10845.
<https://doi.org/10.1021/ja039749a>.
- [46] A. Zagdoun, A.J. Rossini, D. Gajan, A. Bourdolle, O. Ouari, M. Rosay, W.E. Maas, P. Tordo, M. Lelli, L. Emsley, A. Lesage, C. Copéret, Non-aqueous solvents for DNP surface enhanced NMR spectroscopy, *Chem. Commun.*, 48 (2012), p. 654–656.
<https://doi.org/10.1039/C1CC15242D>.
- [47] T.-C. Ong, M.L. Mak-Jurkauskas, J.J. Walish, V.K. Michaelis, B. Corzilius, A.A. Smith, A.M. Clausen, J.C. Cheetham, T.M. Swager, R.G. Griffin, Solvent-Free Dynamic Nuclear Polarization of Amorphous and Crystalline *ortho*-Terphenyl, *J. Phys. Chem. B*, 117 (2013), p. 3040–3046. <https://doi.org/10.1021/jp311237d>.
- [48] K.R. Thurber, T.-N. Le, V. Changcoco, D.J.R. Brook, Verdazyl-ribose: A new radical for solid-state dynamic nuclear polarization at high magnetic field, *J. Magn. Reson.*, 289 (2018), p. 122-131. <https://doi.org/10.1016/j.jmr.2018.02.016>.
- [49] T.J. Keller, A.J. Laut, J. Sirigiri, T. Maly, High-resolution Overhauser dynamic nuclear polarization enhanced proton NMR spectroscopy at low magnetic fields, *J. Magn. Reson.*, 313 (2020), p. 106719. <https://doi.org/10.1016/j.jmr.2020.106719>.
- [50] B. Corzilius, Theory of solid effect and cross effect dynamic nuclear polarization with half-integer high-spin metal polarizing agents in rotating solids, *Phys. Chem. Chem. Phys.*, 18 (2016), p. 27190-27204. <https://doi.org/10.1039/C6CP04621E>.

- [51] W.Th. Wenckebach, Electron Spin–Spin Interactions in DNP: Thermal Mixing vs. the Cross Effect, *Appl. Magn. Reson.*, 52 (2021), p. 731-748.
<https://doi.org/10.1007/s00723-021-01335-0>.
- [52] Kessenikh AV, Manenkov AA, Lushchikov VI, Proton Polarization in Irradiated Polyethylenes, *Soviet Phys.-Solid State*, 5 (1963), p. 37232.
- [53] Z. Pang, S. Jain, C. Yang, X. Kong, K.O. Tan, A unified description for polarization-transfer mechanisms in magnetic resonance in static solids: Cross polarization and DNP, *J. Chem. Phys.*, 156 (2022), p. 244109. <https://doi.org/10.1063/5.0092265>.
- [54] Y. Hovav, A. Feintuch, S. Vega, Theoretical aspects of dynamic nuclear polarization in the solid state – The cross effect, *J. Magn. Reson.*, 214 (2012), p. 29–41.
<https://doi.org/10.1016/j.jmr.2011.09.047>.
- [55] Q.Z. Ni, E. Daviso, T. V. Can, E. Markhasin, S.K. Jawla, T.M. Swager, R.J. Temkin, J. Herzfeld, R.G. Griffin, High Frequency Dynamic Nuclear Polarization, *Acc. Chem. Res.*, 46 (2013), p. 1933–1941. <https://doi.org/10.1021/ar300348n>.
- [56] T. Maly, G.T. Debelouchina, V.S. Bajaj, K.-N. Hu, C.-G. Joo, M.L. Mak–Jurkauskas, J.R. Sirigiri, P.C.A. van der Wel, J. Herzfeld, R.J. Temkin, R.G. Griffin, Dynamic nuclear polarization at high magnetic fields, *J. Chem. Phys.*, 128 (2008), p. 052211.
<https://doi.org/10.1063/1.2833582>.
- [57] K.-N. Hu, C. Song, H. Yu, T.M. Swager, R.G. Griffin, High-frequency dynamic nuclear polarization using biradicals: A multifrequency EPR lineshape analysis, *J. Chem. Phys.*, 128 (2008), p. 052302. <https://doi.org/10.1063/1.2816783>.

- [58] D. Marks, S. Vega, A Theory for Cross-Polarization NMR of Nonspinning and Spinning Samples, *J. Magn. Reson. A*, 118 (1996), p. 157–172.
<https://doi.org/10.1006/jmra.1996.0024>.
- [59] H. Takahashi, C. Fernández-de-Alba, D. Lee, V. Maurel, S. Gambarelli, M. Bardet, S. Hediger, A.-L. Barra, G. De Paëpe, Optimization of an absolute sensitivity in a glassy matrix during DNP-enhanced multidimensional solid-state NMR experiments, *J. Magn. Reson.*, 239 (2014), p. 91–99. <https://doi.org/10.1016/j.jmr.2013.12.005>.
- [60] W.T. Dixon, Spinning-sideband-free and spinning-sideband-only NMR spectra in spinning samples, *J. Chem. Phys.*, 77 (1982), p. 1800–1809.
<https://doi.org/10.1063/1.444076>.
- [61] Y. Yarim-Agaev, P.N. Tutunjian, J.S. Waugh, Sample spinning at the magic angle with rotation-synchronized rf pulses, *J. Magn. Reson.* (1969), 47 (1982), p. 51–60.
[https://doi.org/10.1016/0022-2364\(82\)90320-1](https://doi.org/10.1016/0022-2364(82)90320-1).
- [62] R. Tycko, G. Dabbagh, Double-quantum filtering in magic-angle-spinning NMR spectroscopy: an approach to spectral simplification and molecular structure determination, *J. Am. Chem. Soc.*, 113 (1991), p. 9444–9448.
<https://doi.org/10.1021/ja00025a003>.
- [63] N.C. Nielsen, H. Bildso/e, H.J. Jakobsen, M.H. Levitt, Double-quantum homonuclear rotary resonance: Efficient dipolar recovery in magic-angle spinning nuclear magnetic resonance, *J. Chem. Phys.*, 101 (1994), p. 1805–1812.
<https://doi.org/10.1063/1.467759>.

- [64] T. Guillon, J. Schaefer, Detection of Weak Heteronuclear Dipolar Coupling by Rotational-Echo Double-Resonance Nuclear Magnetic Resonance, *Adv. Magn. Opt. Reason.*, 13 (1989), p. 57–83. <https://doi.org/10.1016/B978-0-12-025513-9.50009-4>.
- [65] M.H. Levitt, *Symmetry-Based Pulse Sequences in Magic-Angle Spinning Solid-State NMR*, eMagRes., John Wiley & Sons, Ltd, Chichester, UK, 9 (2007), p. 165-196. <https://doi.org/10.1002/9780470034590.emrstm0551>.
- [66] A. Brinkmann, M. Edén, M.H. Levitt, Synchronous helical pulse sequences in magic-angle spinning nuclear magnetic resonance: Double quantum recoupling of multiple-spin systems, *J. Chem. Phys.*, 112 (2000), p. 8539–8554. <https://doi.org/10.1063/1.481458>.
- [67] M. Hohwy, H.J. Jakobsen, M. Edén, M.H. Levitt, N.C. Nielsen, Broadband dipolar recoupling in the nuclear magnetic resonance of rotating solids: A compensated C7 pulse sequence, *J. Chem. Phys.*, 108 (1998), p. 2686–2694. <https://doi.org/10.1063/1.475661>.
- [68] J.C.C. Chan, R. Tycko, Recoupling of chemical shift anisotropies in solid-state NMR under high-speed magic-angle spinning and in uniformly ^{13}C -labeled systems, *J. Chem. Phys.*, 118 (2003), p. 8378–8389. <https://doi.org/10.1063/1.1565109>.
- [69] T. Kobayashi, F.A. Perras, Y. Nishiyama, Determination of the chemical shift tensor anisotropy and asymmetry of strongly dipolar coupled protons under fast MAS, *Solid State Nucl. Magn. Reason.*, 114 (2021), p. 101743. <https://doi.org/10.1016/j.ssnmr.2021.101743>.

- [70] C. Guguta, Th.P.J. Peters, R. de Gelder, Structural Investigations of Hydrate, Anhydrate, Free Base, and Hydrochloride Forms of Morphine and Naloxone, *Cryst. Growth Des.*, 8 (2008), p. 4150-4158. <https://doi.org/10.1021/cg800622m>.
- [71] MATLAB (2020), MathWorks main home page. Available at: <https://uk.mathworks.com/products/matlab.html> (accessed January 2020).
- [72] SIMPSON (2020), The Interdisciplinary Nanoscience Centre at Aarhus University: SIMPSON. Aarhus University website for the distribution of SIMPSON. Available at: <https://inano.au.dk/about/research-centers-and-projects/nmr/software/simpson> (accessed January 2020).
- [73] A. Hanson, J.E. Lindgren, Analysis of Morphine base, *Arch. Toxicol.*, 31 (1973), p. 1-6. <https://doi.org/10.1007/BF00330289>.
- [74] J.W. Lewis, S.M. Husbands, 14-Amino-4,5-epoxymorphinan derivatives and their pharmacological actions. *Top. Curr. Chem.*, 299 (2011), p. 93-119. doi:10.1007/128_2010_89. PMID: 21630516.
- [75] M.A. Irvine, D. Oller, J. Boggis, B. Bishop, D. Coombs, E. Wheeler, M. Doe-Simkins, A.Y. Walley, B.D.L. Marshall, J. Bratberg, T.C. Green, Estimating naloxone need in the USA across fentanyl, heroin, and prescription opioid epidemics: a modelling study, *Lancet Public Health*, 7 (2022), p. e210–e218. [https://doi.org/10.1016/S2468-2667\(21\)00304-2](https://doi.org/10.1016/S2468-2667(21)00304-2).
- [76] P. Dietze, M. Jauncey, A. Salmon, M. Mohebbi, J. Latimer, I. van Beek, C. McGrath, D. Kerr, Effect of Intranasal vs Intramuscular Naloxone on Opioid Overdose, *JAMA*.

- Netw. Open, 2 (2019), p. e1914977.
<https://doi.org/10.1001/jamanetworkopen.2019.14977>.
- [77] H.K. Miah, D.A. Bennett, D. Iuga, J.J. Titman, Measuring proton shift tensors with ultrafast MAS NMR, *J. Magn. Reson.*, 235 (2013), p. 1-5.
<https://doi.org/10.1016/j.jmr.2013.07.005>.
- [78] V. Agarwal, The origin of negative cross-peaks in proton-spin diffusion spectrum of fully protonated solids at fast MAS: Coherent or incoherent effect?, *J. Magn. Reson.*, 311 (2020), p. 106661. <https://doi.org/10.1016/j.jmr.2019.106661>.
- [79] S.J. Clark, M.D. Segall, C.J. Pickard, P.J. Hasnip, M.I.J. Probert, K. Refson, M.C. Payne, First principles methods using CASTEP, *Z Kristallogr. Cryst. Mater.*, 220 (2005), p. 567-570. <https://doi.org/10.1524/zkri.220.5.567.65075>.
- [80] J.R. Yates, S.E. Dobbins, C.J. Pickard, F. Mauri, P.Y. Ghi, R.K. Harris, A combined first principles computational and solid-state NMR study of a molecular crystal: flurbiprofen, *Phys. Chem. Chem. Phys.*, 7 (2005), p. 1402-1407.
<https://doi.org/10.1039/b500674k>.
- [81] J.R. Yates, T.N. Pham, C.J. Pickard, F. Mauri, A.M. Amado, A.M. Gil, S.P. Brown, An Investigation of Weak CH...O Hydrogen Bonds in Maltose Anomers by a Combination of Calculation and Experimental Solid-State NMR Spectroscopy, *J. Am. Chem. Soc.*, 127 (2005) p. 10216–10220. <https://doi.org/10.1021/ja051019a>.
- [82] M. Kibalchenko, D. Lee, L. Shao, M.C. Payne, J.J. Titman, J.R. Yates, Distinguishing hydrogen bonding networks in α -D-galactose using NMR experiments and first

principles calculations, Chem. Phys. Lett., 498 (2010), p. 270-276.

<https://doi.org/10.1016/j.cplett.2010.08.077>.

- [83] H.K. Miah, R. Cresswell, D. Iuga, J.J. Titman, ^1H CSA parameters by ultrafast MAS NMR: Measurement and applications to structure refinement, Solid State Nucl. Magn. Reson., 87 (2017), p. 67-72. <https://doi.org/10.1016/j.ssnmr.2017.02.002>.

- [84] D.W. Juhl, Z. Tošner, T. Vosegaard, Versatile NMR simulations using SIMPSON, Annu. Rep. Prog. NMR Spectrosc., 100 (2020) p. 1–59.
<https://doi.org/10.1016/bs.arnmr.2019.12.001>.

Appendix

Appendix 1 – Pantheon Code

```
clear
addpath('C:\Matlab\Pantheon\Functions')
%% Settable Parameters
Magnet = 800; % Magnet strength in MHz
CSA = 18; % 2D simulated Chemical Shift
Anisotropy value
Aysm = 0.5; % 2D simulated Asymmetry
Spinning_Speed = 46296; % 2D or 3D simulation spinning
speed 46296
Number_of_points = 96; % Number of points in the f1
dimension of simulation
Crystal_file = 20; % Crystal file number. Typically
use 20, 143, 232, 615, 28656 NOTE takes longer
Gamma_Angle = 5; % Number of angles tested. ~5-10
for quick analysis, ~32 for high quality NOTE takes longer
DCcor = 64; % Number points of the FID that
are averaged to bring the dipole-dipole coupling down.
Weighting_type = 'Gaussian'; % Type of weighting parameter
Weighting_value = 20; % 'Power' of the above weighting
type
Searchedppm = 6.24; % The ppm value that the '2D'
data will compare itself to.
Additional_Sim_Scaling = 1; % Used to bring down peak heights
to combat artifact
Spectral_Width = 26041; % Only needs to be set for R1632
SimType = '3D'; % 2D or 3D (in the math sense,
1D or 2D NMR language)
MathType3DWeighting = 'Matt'; % Gauss or Matt
Experiment_Type = 'R1632'; % Currently Available: R1632
SC212 C313
PlotMode = 'Compare'; % Solo or Compare
ExpFile = 'tyrosineR1632.mat'; % Name of the bruker
txt file(must be 2D) or processed .mat file for R1632
ExcelProtonData = 'H1HCl.xlsx'; % Name of the excel file containing
the CASTEP data (column 1: Iso, column 2: Aniso, column 3: Aysmmetry)
Artifact_Removal = 'Off'; % Removes the artifact at 0Hz in
experimental data
Artifact_mid_point = -200; % Moves the Artifact removal
window
Artifact_Removal_width = 5; %Sets the size of the removal
window
Bonus_RFinhomogeneity = 'Off'; % Uses a larger profile for rf
inhomogeneity. NOTE takes longer
Mirror_f1_sim = 'Off'; % Reverses the f1 axis
Mirror_f1_exp = 'On'; % Reverses the f1 axis
Exp_2D_Hz_width = 6500; % Width of F1 in Hz (only affected
when artifact removal is on)
```

```

%% Weighting Parameters
fu=' Hz';
dc = DCcor;
ls = 0;
wt = Weighting_type;
wp = Weighting_value;
zf = 256;
bo = 0;
bp = 16;
nothing = 0;
Weighting_2D = ((9*10^8*(Spinning_Speed^-1.843))+0.2)/0.0757;
sigma = ((9*10^8*(Spinning_Speed^-1.843))-0.0082)/4.3026;
%% Picks Experiment
switch SimType
    case '2D'
        switch PlotMode
            case 'Compare'
                switch Experiment_Type
                    case 'R1632'
                        infile = 'R1632.in';
                        load(ExpFile)
                        closest = dsearchn(f2.fq,Searchedppm);
                        ExpY = dat.smx(:,closest);
                        ExpX = f1.fq;
                    case 'SC212'
                        infile = 'SC212.in';
                        Spectral_Width = Spinning_Speed/4;
                        [F1LEFT,F1RIGHT,F2LEFT,F2RIGHT,NROWS,NCOLS]
= readbrukertxt(ExpFile);
                        raw = ExpFile;
                        raw = readmatrix(raw);
                        ExpZ = zeros(NROWS,NCOLS);
                        for i = 1:NROWS
                            blockstart =NCOLS*(i-1)+i;
                            blockend = NCOLS+blockstart-1;
                            ExpZ(i,:) = raw(blockstart:blockend,1);
                        end
                        f1high = F1LEFT*Magnet;
                        f1low = F1RIGHT*Magnet;
                        f2low = F2RIGHT;
                        f2high = F2LEFT;
                        ppmRangef1 = f1high+-f1low;
                        incrementsf1 = ppmRangef1/NROWS;
                        ppmRangef2 = f2high+-f2low;
                        incrementsf2 = ppmRangef2/NCOLS;
                        Expf1 = f1high:-incrementsf1:f1low;
                        Expf1 = Expf1(1:NROWS);
                        Expf2 = f2high:-incrementsf2:f2low;
                        Expf2 = Expf2(1:NCOLS);
                        Expf2 = Expf2';
                        closest = dsearchn(Expf2,Searchedppm);
                        ExpY = ExpZ(:,closest);
                        ExpX = Expf1;
                        ExpX = ExpX';

```

```

        case 'C313'
            infile = 'C313.in';
            Spectral_Width = Spinning_Speed/3;
            [F1LEFT,F1RIGHT,F2LEFT,F2RIGHT,NROWS,NCOLS]
= readbrukertxt(ExpFile);
            raw = ExpFile;
            raw = readmatrix(raw);
            ExpZ = zeros(NROWS,NCOLS);
            for i = 1:NROWS
                blockstart =NCOLS*(i-1)+i;
                blockend = NCOLS+blockstart-1;
                ExpZ(i,:) = raw(blockstart:blockend,1);
            end
            f1high = F1LEFT*Magnet;
            f1low = F1RIGHT*Magnet;
            f2low = F2RIGHT;
            f2high = F2LEFT;
            ppmRangef1 = f1high+-f1low;
            incrementsf1 = ppmRangef1/NROWS;
            ppmRangef2 = f2high+-f2low;
            incrementsf2 = ppmRangef2/NCOLS;
            Expf1 = f1high:-incrementsf1:f1low;
            Expf1 = Expf1(1:NROWS);
            Expf2 = f2high:-incrementsf2:f2low;
            Expf2 = Expf2(1:NCOLS);
            Expf2 = Expf2';
            closest = dsearchn(Expf2,Searchedppm);
            ExpY = ExpZ(:,closest);
            ExpX = Expf1;
            ExpX = ExpX';
        end

        case 'Solo'
            switch Experiment_Type
                case 'R1632'
                    infile = 'R1632.in';
                case 'SC212'
                    infile = 'SC212.in';
                case 'C313'
                    infile = 'C313.in';
            end
        end
    case '3D'
        ExcelProtonData = readmatrix(ExcelProtonData);
        switch PlotMode
            case 'Compare'
                switch Experiment_Type
                    case 'R1632'
                        infile = 'R1632.in';
                        load(ExpFile)
                        ExpZ = dat.smx;
                        ExpZ = real(ExpZ);
                        ExpY = f1.fq;
                        ExpX = f2.fq;
                    end
                end
            end
        end
    end
end

```

```

case 'SC212'
    infile = 'SC212.in';
    Spectral_Width = Spinning_Speed/4;
    [F1LEFT,F1RIGHT,F2LEFT,F2RIGHT,NROWS,NCOLS]
= readbrukertxt(ExpFile);
    raw = ExpFile;
    raw = readmatrix(raw);
    ExpZ = zeros(NROWS,NCOLS);
    for i = 1:NROWS
        blockstart =NCOLS*(i-1)+i;
        blockend = NCOLS+blockstart-1;
        ExpZ(i,:) = raw(blockstart:blockend,1);
    end
    f1high = F1LEFT*Magnet;
    f1low = F1RIGHT*Magnet;
    f2low = F2RIGHT;
    f2high = F2LEFT;
    ppmRangef1 = f1high+-f1low;
    incrementsf1 = ppmRangef1/NROWS;
    ppmRangef2 = f2high+-f2low;
    incrementsf2 = ppmRangef2/NCOLS;
    Expf1 = f1high:-incrementsf1:f1low;
    Expf1 = Expf1(1:NROWS);
    Expf2 = f2high:-incrementsf2:f2low;
    Expf2 = Expf2(1:NCOLS);
    ExpX = Expf2';
    ExpY = Expf1;
case 'C313'
    infile = 'C313.in';
    Spectral_Width = Spinning_Speed/3;
    [F1LEFT,F1RIGHT,F2LEFT,F2RIGHT,NROWS,NCOLS]
= readbrukertxt(ExpFile);
    raw = ExpFile;
    raw = readmatrix(raw);
    ExpZ = zeros(NROWS,NCOLS);
    for i = 1:NROWS
        blockstart =NCOLS*(i-1)+i;
        blockend = NCOLS+blockstart-1;
        ExpZ(i,:) = raw(blockstart:blockend,1);
    end
    f1high = F1LEFT*Magnet;
    f1low = F1RIGHT*Magnet;
    f2low = F2RIGHT;
    f2high = F2LEFT;
    ppmRangef1 = f1high+-f1low;
    incrementsf1 = ppmRangef1/NROWS;
    ppmRangef2 = f2high+-f2low;
    incrementsf2 = ppmRangef2/NCOLS;
    Expf1 = f1high:-incrementsf1:f1low;
    Expf1 = Expf1(1:NROWS);
    Expf2 = f2high:-incrementsf2:f2low;
    Expf2 = Expf2(1:NCOLS);
    ExpX = Expf2';
    ExpY = Expf1;
end
end

```

```

        case 'Solo'
            switch Experiment_Type
                case 'R1632'
                    infile = 'R1632.in';
                case 'SC212'
                    infile = 'SC212.in';
                case 'C313'
                    infile = 'C313.in';
            end
        end
    end
end
%% Creates .in files
mkdir RRfiles
switch SimType
    case '2D'
        text = fileread(infile);
        index = strfind(text, '0p ');
        text1 = text(1:index+2);
        tempstr = text(index+3:end);
        index = strfind(tempstr, ' ');
        index = index(1);
        text2 = tempstr(index+5:end);
        newtext1 = [text1, num2str(CSA), 'p ', num2str(Aysm), text2]
;

        index1 = strfind(newtext1, 'spin_rate');
        text1 = newtext1(1:index1+14);
        tempstr = newtext1(index1+3:end);
        index1 = strfind(tempstr, 'np');
        index1 = index1(1);
        text2 = tempstr(index1-4:index1+5);
        text3 = tempstr(index1+19:index1+41);
        text4 = tempstr(index1+45:index1+63);
        text5 = tempstr(index1+67:index1+133);
        text6 = tempstr(index1+137:end);
        newtext1 = [text1, num2str(Spinning_Speed), text2,
num2str(Number_of_points), text3, num2str(Crystal_file) , text4
,num2str(Gamma_Angle), text5, num2str(Magnet), text6] ;

        index = strfind(newtext1, 'sw');
        text1 = newtext1(1:index+2);
        text2 = newtext1(index+12:end);
        newtext1 = [text1, num2str(Spectral_Width) text2] ;
        switch Bonus_RFinhomogeneity
            case 'On'
                text = newtext1;
                index = strfind(text, '1.3Profile.rf');
                text1 = text(1:index-1);
                text2 = text(index+13:end);
                newtext1 = [text1, 'BigProfile.rf' ,text2] ;
            case 'Off'
                Existence = nothing;
        end
    end
filename = 'RRthing.in';

```



```

file = fopen(filename, 'w');
fprintf(file, newtext1);
fclose(file);
movefile ( filename, 'RRfiles');

case '3D'
for i = 1:length(ExcelProtonData)
    CSA =ExcelProtonData(i,2);
    Aysm =ExcelProtonData(i,3);
    text = fileread(infile);
    index = strfind(text, '0p ');
    text1 = text(1:index+2);
    tempstr = text(index+3:end);
    index = strfind(tempstr, ' ');
    index = index(1);
    text2 = tempstr(index+5:end);
    newtext1 = [text1, num2str(CSA), 'p ', num2str(Aysm),
text2] ;
    index1 = strfind(newtext1, 'spin_rate');
    text1 = newtext1(1:index1+14);
    tempstr = newtext1(index1+3:end);
    index1 = strfind(tempstr, 'np');
    index1 = index1(1);
    text2 = tempstr(index1-4:index1+5);
    text3 = tempstr(index1+19:index1+41);
    text4 = tempstr(index1+45:index1+63);
    text5 = tempstr(index1+67:index1+133);
    text6 = tempstr(index1+137:end);
    newtext1 = [text1, num2str(Spinning_Speed), text2,
num2str(Number_of_points), text3, num2str(Crystal_file) , text4
,num2str(Gamma_Angle), text5, num2str(Magnet), text6] ;
    index = strfind(newtext1, 'sw');
    text1 = newtext1(1:index+2);
    text2 = newtext1(index+12:end);
    newtext1 = [text1, num2str(Spectral_Width) text2] ;
    switch Bonus_RFinhomogeneity
        case 'On'
            text = newtext1;
            index = strfind(text, '1.3Profile.rf');
            text1 = text(1:index-1);
            text2 = text(index+13:end);
            newtext1 = [text1, 'BigProfile.rf' ,text2] ;
        case 'Off'
            Existence = nothing;
    end
    filename = ['RRfiles/RR', num2str(i), '.in'];
    file = fopen(filename, 'w');
    fprintf(file, newtext1);
    fclose(file);
end
end
%% Create fid files
switch SimType
    case '2D'
        command = sprintf('simpson RRfiles/RRthing.in');

```

```

status = system(command);
zero = 0;
for loop = 1:1000
    QNAN_text=fileread('RRthing.fid');
    val = strfind(QNAN_text, 'QNAN');
    if val>zero
        fprintf 'Fail'
        disp (loop)
        command = sprintf('simpson RRfiles/RRthing.in');
        status = system(command);
    end
end
case '3D'
list=length(ExcelProtonData);

for k = 1:list
    command = sprintf('simpson RRfiles/RR%g.in', k);
    status = system(command);
end
zero = 0;
for loop = 1:1000
    for i = 1:list
        QNAN_text=fileread(['RR', num2str(i), '.fid']);
        val = strfind(QNAN_text, 'QNAN');
        if val>zero
            fprintf 'Fail'
            disp (loop)
            fprintf 'Proton'
            disp (k)
            command = sprintf('simpson RRfiles/RR%g.in', i);
            status = system(command);
        end
    end
end
end
end
%% Makes Fid Directory and moves them into it
mkdir Fidfiles
switch SimType
case '2D'
    filename = 'RRthing.fid';
    movefile ( filename, 'Fidfiles');
case '3D'
    for t = 1:list
        filename = ['RR', num2str(t), '.fid'];
        movefile ( filename, 'Fidfiles');
    end
end
end
%% Data
switch SimType
case '2D'
    switch PlotMode
    case 'Compare'
        file = 'C:\Matlab\Pantheon\Fidfiles\RRthing.fid';
        x = fullfile(file);
        FID = readSimpson(x);

```

```

        sw=simpsonPar(x,'SW');
        lf=-sw/2; % temporary scale
        hf=sw/2;
    case 'Solo'
        file = 'C:\Matlab\Pantheon\Fidfiles\RRthing.fid';
        x = fullfile(file);
        FID = readSimpson(x);
        sw=simpsonPar(x,'SW');
        lf=-sw/2; % temporary scale
        hf=sw/2;
    end
case '3D'
    fids = 'C:\Matlab\Pantheon\Fidfiles';
    info = dir(fullfile(fids,'*.fid'));
    list = {info.name};
    list = natsortfiles(list);
    data = {};
    for i = 1:length(list)
        x = fullfile(fids, list{i});
        FID = readSimpson(x);
        sw=simpsonPar(x,'SW');
        lf=-sw/2; % temporary scale
        hf=sw/2;

        FID=normalize(FID);
        FID=dcOffset(FID,dc);
        FID=leftShift(FID,ls);
        FID=windowFID(FID,sw,wt,wp);
        SPE=FT(FID,zf);
        SPE=baselineCorrect(SPE,sw,bo,bp);
        FREQ=getFrequency(SPE,lf,hf);
        SPE = real(SPE);
        data{i,1} = SPE; %#ok<SAGROW>
        data{i,2} = FREQ; %#ok<SAGROW>
    end
    %% Iso ppm values
    isofm = ExcelProtonData(:,1);
    isofm = round(isofm,1);
end
%% Processes data
switch SimType
case '2D'
    switch Experiment_Type
    case 'R1632'
        FID=normalize(FID);
        FID=dcOffset(FID,dc);
        FID=leftShift(FID,ls);
        FID=windowFID(FID,sw,wt,wp);
        SPE=FT(FID,zf);
        SPE=baselineCorrect(SPE,sw,bo,bp);
        FREQ=getFrequency(SPE,lf,hf);
        close all
    case 'SC212'
        FID=normalize(FID);

```

```

FID=dcOffset(FID,dc);
FID=leftShift(FID,ls);
FID>windowFID(FID,sw,wt,wp);
SPE=FT(FID,zf);
SPE=baselineCorrect(SPE,sw,bo,bp);
FREQ=getFrequency(SPE,lf,hf);
close all

case 'C313'
FID=normalize(FID);
FID=dcOffset(FID,dc);
FID=leftShift(FID,ls);
FID>windowFID(FID,sw,wt,wp);
SPE=FT(FID,zf);
SPE=baselineCorrect(SPE,sw,bo,bp);
FREQ=getFrequency(SPE,lf,hf);
close all

end
case '3D'
switch MathType3DWeighting
case 'Gauss'
% Weights data
points = zeros(length(data{1,1}),270);
X = -2:0.1:24.9;

for i = 1:length(isofm)
t = isofm(i);
[~,u]=ismembertol(t,X);
p = data{i,1};
p = transpose(p);
points(:,u) = p;
clear t u p ~;
end
preweight = [];
for i = 1:length(data{1,1})
datapoints = points(i,:);
datapoints = ifft(datapoints);
preweight(i,:) = datapoints; %#ok<SAGROW>
clear datapoints
end
postweight = [];
for i = 1:length(data{1,1})
asd = preweight(i,:);
asd = transpose(asd );
asd = asd (1:270);
asd = windowFID(asd,sw,wt,Weighting_2D);
asd = transpose(asd);
asd = fft(asd );
postweight(i,:) = asd ; %#ok<SAGROW>
clear points
end
postweight = real(postweight);
Z = postweight;
Z = real(Z);
case 'Matt'

```

```

        %% Weights data
        points = zeros(length(data{1,1}),270);
        X = -2:0.1:24.9;
        X = transpose(X);
        %% Add X slices
        for i = 1:length(isofm)
            slice = data{i,1};
            insertpoint = dsearchn(X,isofm(i));
            points(:,insertpoint) = slice;
        end
        sumslice = 1:length(X);
        sumslice = sumslice*0;
        %% Weights Y slices
        for i = 1:length(slice)
            sumslice = sumslice*0;
            for k = 1:length(isofm)
                for l = 1:length(X)
                    alpha = data{k,1}(i,1);
                    SliceY(l) = alpha*exp(-(X(l) -isofm(k)
) ^2) / (2*(sigma^2))); %#ok<SAGROW>
                end
                sumslice = sumslice + SliceY;
            end
            points(i,:) = sumslice;
        end
        Z = points;
    end

end

%% Scales to Experimental data
SPE = SPE*100000;
%% Finds mid point x value
switch Experiment_Type
    case 'R1632'
        SPE = real(SPE);
        lFREQ = length(FREQ);
        lFREQ = lFREQ/2;
        lFREQ = lFREQ+1;
        MidLocation = FREQ(lFREQ);
        MidCorrection = MidLocation;
        FREQ = FREQ-MidCorrection;
    case 'SC212'
        SPE = real(SPE);
    case 'C313'
        SPE = real(SPE);
end

%% Finding Mid point of Experiment data
switch SimType
    case '2D'
        switch PlotMode
            case 'Compare'
                switch Experiment_Type
                    case 'R1632'
                        ExpY = real(ExpY);
                        TExpX = length(ExpX);

```

```

        TExpX = TExpX/2;
        TExpX = TExpX+1;
        TExpX = round(TExpX);
        MidLocation = ExpX(TExpX);
        MidCorrection = MidLocation;
        ExpX = ExpX-MidCorrection;
    case 'SC212'
        TExpX = length(ExpX);
        TExpX = TExpX/2;
        TExpX = TExpX+1;
        TExpX = round(TExpX);
        MidLocation = ExpX(TExpX);
        MidCorrection = MidLocation;
        ExpX = ExpX-MidCorrection;
    case 'C313'
        TExpX = length(ExpX);
        TExpX = TExpX/2;
        TExpX = TExpX+1;
        TExpX = round(TExpX);
        MidLocation = ExpX(TExpX);
        MidCorrection = MidLocation;
        ExpX = ExpX-MidCorrection;
    end
    case 'Solo'
        Existence = nothing;
    end
case '3D'
    switch PlotMode
        case 'Compare'
            switch Experiment_Type
                case 'R1632'
                    TExpY = length(ExpY);
                    TExpY = TExpY/2;
                    TExpY = TExpY+1;
                    TExpY = round(TExpY);
                    MidLocation = ExpY(TExpY);
                    MidCorrection = MidLocation;
                    ExpY = ExpY-MidCorrection;
                case 'SC212'
                    TExpY = length(ExpY);
                    TExpY = TExpY/2;
                    TExpY = TExpY+1;
                    TExpY = round(TExpY);
                    MidLocation = ExpY(TExpY);
                    MidCorrection = MidLocation;
                    ExpY = ExpY-MidCorrection;
                case 'C313'
                    TExpX = length(ExpY);
                    TExpX = TExpX/2;
                    TExpX = TExpX+1;
                    TExpX = round(TExpX);
                    MidLocation = ExpY(TExpX);
                    MidCorrection = MidLocation;
                    ExpY = ExpY-MidCorrection;
            end
        end
    end
end

```

```

        case 'Solo'
            Existence = nothing;
        end
    end
end
%% Fixes Experimental Background level
switch SimType
    case '2D'
        switch PlotMode
            case 'Compare'
                minval = min(ExpY);
                ExpY = ExpY-minval;
                minval = min(SPE);
                SPE = SPE-minval;
                switch Experiment_Type
                    case 'R1632'
                        MaxWidth = Magnet*5+500;
                        closestpos = dsearchn(FREQ,MaxWidth);
                        closestposExp = dsearchn(f1.fq,MaxWidth);
                        OtherMaxWidth = -MaxWidth;
                        closestneg = dsearchn(FREQ,OtherMaxWidth);
                        closestnegExp =
dsearchn(f1.fq,OtherMaxWidth);
                        % Sim Zeroing
                        SPE(1:closestneg)=0;
                        endval = length(SPE);
                        SPE(closestpos:endval)=0;
                        ExpY(1:closestnegExp)=0;
                        endval = length(ExpY);
                        ExpY(closestposExp:endval)=0;
                    case 'SC212'
                        MaxWidth = Magnet*5 + 50000;
                        closestpos = dsearchn(FREQ,MaxWidth);
                        closestposExp = dsearchn(ExpX,MaxWidth);
                        OtherMaxWidth = -MaxWidth;
                        closestneg = dsearchn(FREQ,OtherMaxWidth);
                        closestnegExp =
dsearchn(ExpX,OtherMaxWidth);
                        % Sim Zeroing
                        SPE(1:closestneg)=0;
                        endval = length(SPE);
                        SPE(closestpos:endval)=0;
                    case 'C313'
                        MaxWidth = Magnet*5 + 50000;
                        closestpos = dsearchn(FREQ,MaxWidth);
                        closestposExp = dsearchn(ExpX,MaxWidth);
                        OtherMaxWidth = -MaxWidth;
                        closestneg = dsearchn(FREQ,OtherMaxWidth);
                        closestnegExp =
dsearchn(ExpX,OtherMaxWidth);
                        % Sim Zeroing
                        SPE(1:closestneg)=0;
                        endval = length(SPE);
                        SPE(closestpos:endval)=0;
                end
            case 'Solo'

```

```

        Existence = nothing;
    end
    case '3D'
        switch PlotMode
            case 'Compare'
                minval = min(min(ExpZ));
                ExpZ = ExpZ-minval;
                switch Experiment_Type
                    case 'R1632'
                        MaxWidth = Magnet*10;
                        closestposExp = dsearchn(ExpY,MaxWidth);
                        OtherMaxWidth = -MaxWidth;
                        closestnegExp =
dsearchn(ExpY,OtherMaxWidth);
                        if closestnegExp<closestposExp
                            for i = 1:length(ExpX)
                                ExpZ(1:closestnegExp,i) = 0;
                                ExpZ(closestposExp:end,i) = 0;
                            end
                        else
                            for i = 1:length(ExpX)
                                ExpZ(1:closestposExp,i) = 0;
                                ExpZ(closestnegExp:end,i) = 0;
                            end
                        end
                    end
                case 'Solo'
                    Existence = nothing;
            end
        end
    end

%% Removal of artifact at 0Hz
switch PlotMode
    case 'Compare'
        switch Artifact_Removal
            case 'On'
                switch SimType
                    case '2D'
                        x0 = ExpX;
                        y0 = ExpY;
                        mid = dsearchn(ExpX,Artifact_mid_point);
                        x01 = x0(1:mid-Artifact_Removal_width);
                        x02 = x0(mid+Artifact_Removal_width:end);
                        y01 = y0(1:mid-Artifact_Removal_width);
                        y02 = y0(mid+Artifact_Removal_width:end);
                        y02 = fliplr(y02);
                        x0 = cat(1,x01,x02);
                        y0 = cat(1,y01,y02);
                        spl = spline(x0,y0);
                        ExpX =
                        linspace(-
Exp_2D_Hz_width/2,Exp_2D_Hz_width/2,1000);
                        ExpY = fnval(spl,ExpX);
                    case '3D'
                        for i = 1:length(ExpX)
                            y0 = ExpY;

```



```

        z0 = ExpZ(:,i);
        ExpYWigs = ExpY';
        mid =
dsearchn(ExpYWigs,Artifact_mid_point);
        y01 = y0(1:mid-Artifact Removal_width);
        y02 =
y0(mid+Artifact Removal_width:end);
        z01 = z0(1:mid-Artifact Removal_width);
        z02 =
z0(mid+Artifact Removal_width:end);
        z02 = fliplr(z02);
        y0 = cat(2,y01,y02);
        z0 = cat(1,z01,z02);
        spl = spline(y0,z0);
        switch Experiment_Type
            case 'SC212'
                ExpYY = linspace(-
5000,5000,1000);
            case 'C313'
                ExpYY = linspace(-
5000,5000,1000);
        end
        MidData = fnval(spl,ExpYY);
        MidData = fliplr(MidData);
        ExpZZ(:,i) = MidData; %#ok<SAGROW>

    end
    ExpZ = ExpZZ;
    ExpY = ExpYY;
end
case 'Off'
    Existence = nothing;
end
case 'Solo'
    Existence = nothing;
end
%% Sets max height to the same
switch SimType
    case '2D'
        switch PlotMode
            case 'Compare'
                minval = min(ExpY);
                ExpY = ExpY-minval;
                minval = min(SPE);
                SPE = SPE-minval;
                ymax=max(ExpY);
                SPEmax=max(SPE);
                if SPEmax>ymax
                    factor = SPEmax/ymax;
                    ExpY=ExpY*factor;
                else
                    factor = ymax/SPEmax;
                    SPE=SPE*factor;
                end
            case 'Solo'

```

```

        Existence = nothing;
    end
    case '3D'
        switch PlotMode
            case 'Compare'
                ymax=max(max(ExpZ));
                zmax=max(max(Z));
                if zmax>ymax
                    factor = zmax/ymax;
                    ExpZ=ExpZ*factor;
                else
                    factor = ymax/zmax;
                    Z=Z*factor;
                end
            case 'Solo'
                Existence = nothing;
            end
        Y=data{1,2};
        SExpY = length(Y);
        SExpY = SExpY/2;
        SExpY = SExpY+1;
        SExpY = round(SExpY);
        MidLocation = Y(SExpY);
        MidCorrection = MidLocation;
        Y = Y-MidCorrection;
    end
    switch Mirror_f1_sim
        case 'On'
            switch SimType
                case '2D'
                    %ExpX=-ExpX;
                    FREQ=-FREQ;
                case '3D'
                    Y=-Y;
                    %ExpY=-ExpY;
                end
            case 'Off'
                Existence = nothing;
            end
        switch Mirror_f1_exp
            case 'On'
                switch SimType
                    case '2D'
                        ExpX=-ExpX;
                        %FREQ=-FREQ;
                    case '3D'
                        ExpY=-ExpY;
                    end
                case 'Off'
                    Existence = nothing;
                end
            end
        %% Plotting
        switch SimType
            case '2D'
                SPE = SPE*Additional_Sim_Scaling;

```

```

switch PlotMode
    case 'Compare'
        plot(ExpX,ExpY, 'color', 'r')
        hold on
        plot(FREQ,SPE, 'color', 'k')
    case 'Solo'
        plot(FREQ,SPE, 'color', 'k')
end
case '3D'
    switch PlotMode
        case 'Compare'
            %% Plots Sim data

pl=[1,0.75,0.7,0.65,0.6,0.55,0.5,0.49,0.48,0.47,0.46,0.45,0.44,0.43,
0.42,0.41,0.4,0.39,0.38,0.37,0.36,0.35,0.34,0.33,0.32,0.31,0.3,0.29,
0.28,0.27,0.26,0.25,0.24,0.23,0.22,0.21,0.2,0.19,0.18,0.17,0.16,0.15
,0.14,0.13,0.12,0.11,0.1,0.09,0.08,0.07,0.06,0.05,0.04,0.03,0.02,0.0
1];

            pl=pl*max(max(Z));
            contour(X,Y,Z,pl,'k');
            hold on
            %% Plots Experimental data

%pl=[1,0.75,0.7,0.65,0.6,0.55,0.5,0.49,0.48,0.47,0.46,0.45,0.44,0.43
,0.42,0.41,0.4,0.39,0.38,0.37,0.36,0.35,0.34,0.33,0.32,0.31,0.3,0.29
,0.28,0.27,0.26,0.25,0.24,0.23,0.22,0.21,0.2,0.19,0.18,0.17,0.16,0.1
5,0.14,0.13,0.12,0.11,0.1];

pl=[1.0,0.95,0.9,0.85,0.8,0.75,0.7,0.65,0.6,0.55,0.5,0.45,0.4,0.35,0
.3,0.25,0.2];

%pl=[1.0,0.9,0.75,0.675,0.6,0.55,0.5,0.4,0.325,0.285];
            pl=pl*max(max(real(ExpZ)));
            contour(ExpX,ExpY,ExpZ,pl,'r')
            set(gca, 'XDir','reverse') %reverse x axis
            xlim([-2 30])
            hold off
        case 'Solo'
            Y=data{1,2};

pl=[1,0.75,0.7,0.65,0.6,0.55,0.5,0.49,0.48,0.47,0.46,0.45,0.44,0.43,
0.42,0.41,0.4,0.39,0.38,0.37,0.36,0.35,0.34,0.33,0.32,0.31,0.3,0.29,
0.28,0.27,0.26,0.25,0.24,0.23,0.22,0.21,0.2,0.19,0.18,0.17,0.16,0.15
,0.14,0.13,0.12,0.11,0.1,0.06];
            pl=pl*max(max(Z));
            contour(X,Y,Z,pl,'k');
            set(gca, 'XDir','reverse') %reverse x axis
        end
    end
end
% Cleanup Section
fclose('all');

switch SimType
    case '2D'
        cd 'C:\Matlab\Pantheon\Fidfiles'

```

```

thing = 'RRthing.fid';

delete (thing);
clear thing

cd 'C:\Matlab\Pantheon\RRfiles'

```

Appendix 2 – Example .in file

```

spinsys {
  channels 1H
  nuclei 1H
  shift 1 0p 12p 0.61 0 0 0
}

par {
  spin_rate      58600
  np             128
  crystal_file   zcw143
  gamma_angles   32
  start_operator I1x
  detect_operator I1p
  proton_frequency 400e6
  variable N     2
  variable n     2
  variable nu    1
  variable S     1
  sw            12500
  verbose       1101
  rfprof_file   1.3Profile.rf
}

proc pulseseq {} {
  global par

  maxdt 1.0

  set rf [expr 4.*$par(spin_rate)]
  set t90 [expr 0.25e6/$rf]
  set t360 [expr 1.0e6/$rf]
  set t540 [expr 1.5e6/$rf]
  set t270 [expr 0.75e6/$rf]

  if {$par(S) == 1} {
    acq
    for {set i 0} {$i < [expr $par(np)/(2*$par(n))-1]} {incr i} {
      for {set j 0} {$j < $par(n)} {incr j} {
        set phi [expr 360.*$j*$par(nu)/$par(N)]
        pulse $t90 $rf $phi
        pulse $t360 $rf [expr 180.+$phi]
        pulse $t540 $rf $phi
      }
    }
  }
}

```

```

    pulse $t360 $rf [expr 180.+$phi]
    pulse $t90 $rf $phi
}

for {set j [expr $par(n)]} {$j > 0} {incr j -1} {
    set phi [expr 360.*($j-1)*$par(nu)/$par(N)]
    pulse $t90 $rf $phi
    pulse $t360 $rf [expr 180.+$phi]
    pulse $t540 $rf $phi
    pulse $t360 $rf [expr 180.+$phi]
    pulse $t90 $rf $phi
}
acq
}
}

if {$par(S) == 0} {
    acq
    for {set i 0} {$i < [expr $par(np)/$par(n)-1]} {incr i} {
        for {set j 0} {$j < $par(n)} {incr j} {
            set phi [expr 360.*$j*$par(nu)/$par(N)]
            pulse $t90 $rf $phi
            pulse $t360 $rf [expr 180.+$phi]
            pulse $t540 $rf $phi
            pulse $t360 $rf [expr 180.+$phi]
            pulse $t90 $rf $phi
            acq
        }
    }
}
}

proc main {} {
    global par
    set f [fsimpson]
    fsave $f $par(name).fid
}

```

Appendix 3 – Example .cell file (naloxone HCl)

#

CIF written by cell_write_cif: Keith Refson, Apr 2010

#

data_naloxoneHCl

_audit_creation_date '14:02:24 (GMT+1.0) 25th June 2021'

_audit_creation_method 'Generated by CASTEP 18.100'

_symmetry_Int_Tables_number 19

_symmetry_space_group_name_Hall 'P 2ac 2ab'

_symmetry_space_group_name_H_M 'P2_12_12_1'

loop_

_symmetry_equiv_pos_as_xyz

x,y,z

x+1/2,-y+1/2,-z

-x+1/2,-y,z+1/2

-x,y+1/2,-z+1/2

_cell_length_a 7.881433812586057

_cell_length_b 13.411020570480717

_cell_length_c 18.660471216330436

_cell_angle_alpha 90.000000000000000

_cell_angle_beta 90.000000000000000

_cell_angle_gamma 90.000000000000000

loop_

_atom_site_label

_atom_site_type_symbol

_atom_site_fract_x

_atom_site_fract_y

_atom_site_fract_z

_atom_site_U_iso_or_equiv

_atom_site_occupancy

H1 H 0.395114440502399 0.582586092579280 0.400483502490528 0.0100 1.0000

H5 H 0.519449146615871 0.318297471800898 0.018744145796705 0.0100 1.0000

H9 H 0.654833901766802 0.491518563794173 0.003963274765509 0.0100 1.0000

H13 H 0.088181882309710 0.716708594792725 0.160599724413022 0.0100 1.0000

H17 H 0.105103029176223 0.721696035401782 0.293668376067178 0.0100 1.0000

H21 H 0.646901482972617 0.357325040187570 0.237012644362005 0.0100 1.0000

H25 H 0.423510978898245 0.222726214534585 0.137871768517865 0.0100 1.0000

H29 H 0.211722399509447 0.220067159549320 0.171060356014226 0.0100 1.0000

H33 H 0.177491010052802 0.400901043221571 0.128595457455697 0.0100 1.0000

H37 H 0.232507054657970 0.320829590302659 0.057306764942138 0.0100 1.0000

H41 H 0.357687937345668 0.475476417549063 0.989411271975522 0.0100 1.0000

H45 H 0.148778209616841 0.557122583312706 0.053070561883963 0.0100 1.0000

H49 H 0.291386980217055 0.655223237278483 0.039335590075035 0.0100 1.0000

H53 H 0.780306587638249 0.455202103944164 0.128109175654155 0.0100 1.0000

H57 H 0.737711536153089 0.548569352266626 0.194032896076482 0.0100 1.0000

H61 H 0.793993591634738 0.618234265042644 0.067988841195450 0.0100 1.0000

H65 H 0.596598111452141 0.656733001332872 0.105705337303222 0.0100 1.0000

H69 H 0.710311315151023 0.642874935888021 0.950228965680643 0.0100 1.0000

H73 H 0.518842695445959 0.695538824645605 0.984251796387687 0.0100 1.0000

H77 H 0.348065900874318 0.596779519218740 0.893881149062961 0.0100 1.0000

H81 H 0.709298659281177 0.540671447633380 0.842311688915299 0.0100 1.0000

H85 H 0.504951623502992 0.521280361016390 0.793469871057649 0.0100 1.0000

H89 H 0.504288339396961 0.396870222923928 0.437207061262147 0.0100 1.0000

H93 H 0.437488237833363 0.323412018181290 0.379250639291022 0.0100 1.0000

H97 H 0.834384269730805 0.211329094472220 0.075630491100667 0.0100 1.0000

H101 H 0.897029484346447 0.308919391452531 0.035701140133829 0.0100 1.0000

C1 C 0.176600000000000 0.667430000000000 0.188210000000000 0.0100 1.0000

C5 C 0.185600000000000 0.670670000000000 0.263370000000000 0.0100 1.0000

C9 C 0.293800000000000 0.605960000000000 0.303370000000000 0.0100 1.0000

C13 C 0.3921000000000000 0.5376700000000000 0.2639600000000000 0.0100 1.0000

C17 C 0.5230000000000000 0.3934500000000000 0.2292900000000000 0.0100 1.0000

C21 C 0.3836000000000000 0.3104300000000000 0.2318500000000000 0.0100 1.0000

C25 C 0.3214000000000000 0.2684100000000000 0.1612400000000000 0.0100 1.0000

C29 C 0.2793000000000000 0.3534400000000000 0.1073700000000000 0.0100 1.0000

C33 C 0.4044000000000000 0.5054800000000000 0.0404800000000000 0.0100 1.0000

C37 C 0.2752000000000000 0.5847600000000000 0.0685800000000000 0.0100 1.0000

C41 C 0.2815000000000000 0.6004600000000000 0.1491700000000000 0.0100 1.0000

C45 C 0.3889800000000000 0.5391900000000000 0.1893300000000000 0.0100 1.0000

C49 C 0.5143200000000000 0.4618300000000000 0.1616700000000000 0.0100 1.0000

C53 C 0.4414500000000000 0.4153400000000000 0.0923400000000000 0.0100 1.0000

C57 C 0.6892000000000000 0.5122700000000000 0.1454000000000000 0.0100 1.0000

C61 C 0.6699000000000000 0.5926000000000000 0.0870500000000000 0.0100 1.0000

C65 C 0.5762000000000000 0.6277600000000000 0.9619000000000000 0.0100 1.0000

C69 C 0.4859000000000000 0.5894200000000000 0.8957900000000000 0.0100 1.0000

C73 C 0.5715000000000000 0.5488200000000000 0.8407400000000000 0.0100 1.0000

N1 N 0.5786400000000000 0.5504100000000000 0.0221400000000000 0.0100 1.0000

O1 O 0.2894800000000000 0.6106500000000000 0.3776500000000000 0.0100 1.0000

O5 O 0.4970600000000000 0.4616700000000000 0.2902400000000000 0.0100 1.0000

O9 O 0.3303000000000000 0.2809800000000000 0.2898800000000000 0.0100 1.0000

O13 O 0.5710800000000000 0.3534500000000000 0.0611000000000000 0.0100 1.0000

O17 O 0.4781000000000000 0.3256900000000000 0.4292100000000000 0.0100 1.0000

O21 O 0.9346500000000000 0.2435700000000000 0.0542400000000000 0.0100 1.0000

Cl1 Cl 0.5794200000000000 0.5492700000000000 0.4711200000000000 0.0100 1.0000

Appendix 4. Refocused INADEQUATE pulse program.

```
# 1 "/root/.topspin-
BladeEpu/local_acqu/NaloxoneFA_D20H2O_90_10_2472023/30/lists/pp/ref_inadequate.jjt"
# 1 "<built-in>"
# 1 "<command-line>"
# 1 "/root/.topspin-
BladeEpu/local_acqu/NaloxoneFA_D20H2O_90_10_2472023/30/lists/pp/ref_inadequate.jjt"
;ref_inadequate
```

;See Emsley et al. JACS 119, 7867 (1997)

```
;Avance III version
;parameters:
;d0 : =1u, t1 evolution period
;d1 : recycle delay
;d10 : tau delay for J evolution
;l0 : make d10=1/(4J), synchronised to spinning
;l20 : loop counter for saturation
;in0 : = 1/swh(F1)
;p1 : X 90 degree pulse
;p2 : X 180 degree pulse
;p3 : H 90 degree pulse
```

```

;p15 : contact time
;pcpd2 : pulse length in decoupling sequence
;p11 : X power level for CP
;sp0 : proton power level during CP
;p12 : =120dB, not used
;p111 : power level for X pulses
;p112 : power level for H 90 and proton decoupling
;cpdprg2 : sequence used for decoupling
;spnam0 : shape name for variable amplitude CP
;cnst31 : spinning frequency
;cnst11 : to adjust t=0 for acquisition, if digmod = baseopt
# 28 "/root/.topspin-
BladeEpu/local_acqu/NaloxoneFA_D20H20_90_10_2472023/30/lists/pp/ref_inadequate.jjt"
;$COMMENT=INADEQUATE, CP excitation
;$CLASS=Solids
;$DIM=2D
;$TYPE=cross polarisation
;$SUBTYPE=homonuclear correlation

"d10=(1s/cnst31)*I0-p2/2"
"d11=d10-p1/2"
"acqt0=1u*cnst11"
"in0=inf1"

# 1 "/root/.topspin-
BladeEpu/local_acqu/NaloxoneFA_D20H20_90_10_2472023/30/lists/pp/p15_prot.incl" 1
;p15_prot.incl
;avance-version (13/01/29)
;Test the rf on-time and duty cycle
;protect against too long contact time
;Test the rf on-time and duty cycle

```

```

;
;$CLASS=Solids INCL
;$COMMENT=protect against too long contact time

1m
if "p15 < 10.1m" goto Passp15
2u
print "contact time exceeds 10msec limit!"
goto HaltAcqu
Passp15, 1m
# 20 "/root/.topspin-
BladeEpu/local_acqu/NaloxoneFA_D20H20_90_10_2472023/30/lists/pp/p15_prot.incl"
;$Id:$
# 40 "/root/.topspin-
BladeEpu/local_acqu/NaloxoneFA_D20H20_90_10_2472023/30/lists/pp/ref_inadequate.jjt"
2
                ;make sure p15 does not exceed 10 msec
                ;let supervisor change this pulseprogram if
                ;more is needed

# 1 "/root/.topspin-
BladeEpu/local_acqu/NaloxoneFA_D20H20_90_10_2472023/30/lists/pp/aq_prot.incl" 1
;aq_prot.incl
;avance-version (13/01/28)
;Test the rf on-time and duty cycle
;protect against too long acquisition time

;$CLASS=Solids INCL
;$COMMENT=protect against too long acquisition time
# 9 "/root/.topspin-
BladeEpu/local_acqu/NaloxoneFA_D20H20_90_10_2472023/30/lists/pp/aq_prot.incl"

```

```

1m
if "aq < 50.1m" goto Passaq
2u
print "acquisition time exceeds 50m limit!"
goto HaltAcqu
Passaq, 1m

;$ld:$
# 44 "/root/.topspin-
BladeEpu/local_acqu/NaloxoneFA_D20H20_90_10_2472023/30/lists/pp/ref_inadequate.jjt"
2
;allows max. 50 msec acquisition time, supervisor
;may change to max. 1s at less than 5 % duty cycle
;and reduced decoupling field

# 1 "mc_line 48 file /root/.topspin-
BladeEpu/local_acqu/NaloxoneFA_D20H20_90_10_2472023/30/lists/pp/ref_inadequate.jjt
exp. def. part of mc cmd. before ze"
; dimension 2D; AQ_mode (F1) States-TPPI
define delay MCWRK
define delay MCREST
define loopcounter ST1CNT
"ST1CNT = trunc(td1 / 2)"
"MCREST = 10m - 10m"
"MCWRK = 0.200000*10m"
# 48 "/root/.topspin-
BladeEpu/local_acqu/NaloxoneFA_D20H20_90_10_2472023/30/lists/pp/ref_inadequate.jjt"
1 ze
# 1 "mc_line 48 file /root/.topspin-
BladeEpu/local_acqu/NaloxoneFA_D20H20_90_10_2472023/30/lists/pp/ref_inadequate.jjt
exp. def. of mc cmd. after ze"
LBLAV, MCWRK

```

```

# 49 "/root/.topspin-
BladeEpu/local_acqu/NaloxoneFA_D20H20_90_10_2472023/30/lists/pp/ref_inadequate.jjt"
# 1 "mc_line 49 file /root/.topspin-
BladeEpu/local_acqu/NaloxoneFA_D20H20_90_10_2472023/30/lists/pp/ref_inadequate.jjt
exp. start label for mc cmd."

2 MCWRK * 3 do:f2

LBLSTS1, MCWRK

LBLF1, MCWRK

MCREST

# 50 "/root/.topspin-
BladeEpu/local_acqu/NaloxoneFA_D20H20_90_10_2472023/30/lists/pp/ref_inadequate.jjt"

1u

5 d20

(p3 pl12 ph0):f2 ;(p1 pl11 ph0):f1

lo to 5 times l20

d1

(p3 pl12 ph11):f2

(p15 pl1 ph2):f1 (p15:sp0 ph12):f2

d10 cpds2:f2

(p2 pl11 ph4):f1

d11

(p1 ph5):f1

d0

(p1 ph6):f1

d11

(p2 ph7):f1

d10

go=2 ph31

1m do:f2

# 1 "mc_line 68 file /root/.topspin-
BladeEpu/local_acqu/NaloxoneFA_D20H20_90_10_2472023/30/lists/pp/ref_inadequate.jjt
exp. mc cmd. in line"

MCWRK wr #0 if #0 zd ip2 MCWRK ip4 MCWRK ip5

```

lo to LBLSTS1 times 2

MCWRK id0

lo to LBLF1 times ST1CNT

MCWRK rf #0

lo to LBLAV times tdav

```
#69 "/root/.topspin-  
BladeEpu/local_acqu/NaloxoneFA_D20H20_90_10_2472023/30/lists/pp/ref_inadequate.jjt"
```

HaltAcqu, 1m

exit

```
#72 "/root/.topspin-  
BladeEpu/local_acqu/NaloxoneFA_D20H20_90_10_2472023/30/lists/pp/ref_inadequate.jjt"
```

ph0= 0

ph11= 1 3

ph2= (8) 2 2 4 4 6 6 0 0

ph4= (8) 0 0 2 2 4 4 6 6 2 2 4 4 6 6 0 0

4 4 6 6 0 0 2 2 6 6 0 0 2 2 4 4

ph5=(8) 0 0 2 2 4 4 6 6

ph6= 0

ph7= 1

ph12= 0

ph31= 0 2 2 0 0 2 2 0 2 0 0 2 2 0 0 2

Appendix 5 SC212 Pulse Program

```
# 1 "/root/.topspin-BladeEpu/local_acqu/ppDirs/ROCSA_SC212"
```

```
# 1 "<built-in>"
```

```
# 1 "<command-line>"
```

```
# 1 "/root/.topspin-BladeEpu/local_acqu/ppDirs/ROCSA_SC212"
```

```
;avance-version (12/01/11)
```

```
;parameters:
```

```
;ns :
```

```
;d1 : recycle delay
```

```

;p1 : power level for 1H 90
;l23 : R-Sequence counter
;p1 : 1H 90 pulse
;p4 : 1H 360 pulse length for R-sequece
;p6 : 1H 540 pulse length for R-sequece

# 1 "/root/.topspin-BladeEpu/local_acqu/ppDirs/Avance.incl" 1
;Avance4.incl
; for AV 4
;
;avance-version (16/08/18)
;
;$CLASS=HighRes Incl
;$COMMENT=
# 19 "/root/.topspin-BladeEpu/local_acqu/ppDirs/Avance.incl"
;setrt0 denotes TimingController

# 50 "/root/.topspin-BladeEpu/local_acqu/ppDirs/Avance.incl"
# 51 "/root/.topspin-BladeEpu/local_acqu/ppDirs/Avance.incl"

# 63 "/root/.topspin-BladeEpu/local_acqu/ppDirs/Avance.incl"
# 89 "/root/.topspin-BladeEpu/local_acqu/ppDirs/Avance.incl"
# 90 "/root/.topspin-BladeEpu/local_acqu/ppDirs/Avance.incl"

# 123 "/root/.topspin-BladeEpu/local_acqu/ppDirs/Avance.incl"
;#define LOWQ
;#define HIGHQ

```



```

;#define MIX_UP
;#define MIX_DOWN
# 136 "/root/.topspin-BladeEpu/local_acqu/ppDirs/Avance.incl"
;$Id: Avance4.incl,v 1.11 2016/11/11 13:43:39 ber Exp $
# 12 "/root/.topspin-BladeEpu/local_acqu/ppDirs/ROCSA_SC212" 2

;$COMMENT=
;$CLASS = Solids
;$DIM = 2D
;$TYPE= half interger
;$SUBTYPE= simple 2D

;cnst11 : to adjust t=0 for aquisition, if digmod = baseopt
;cnst31 : set spinning frequency
# 22 "/root/.topspin-BladeEpu/local_acqu/ppDirs/ROCSA_SC212"
;"p4=p1*4"
;"p6=p1*6"
"acqt0=1u*cnst11"
"|23=0"
;"cnst31=1.e6/(4*p4)"
"cnst31=46296"
"|1=td1*0.5"

"d2=(d1/2)+cnst31-cnst31"
"in0=8*p1+8*p4+4*p6"
"d0=in0"

# 30 "/root/.topspin-BladeEpu/local_acqu/ppDirs/ROCSA_SC212"
# 30 "/root/.topspin-BladeEpu/local_acqu/ppDirs/ROCSA_SC212"

```

1 ze

d0

2 d2

3 d2

4 30m

(p1 ph10 pl1):f1

38 "/root/.topspin-BladeEpu/local_acqu/ppDirs/ROCSA_SC212"

5 (p1 ph1):f1

(p4 ph2):f1

(p6 ph1):f1

(p4 ph2):f1

(p1 ph1):f1

(p1 ph1):f1

(p4 ph2):f1

(p6 ph1):f1

(p4 ph2):f1

(p1 ph1):f1

(p1 ph1):f1

(p4 ph2):f1

(p6 ph1):f1

(p4 ph2):f1

(p1 ph1):f1

(p1 ph1):f1

(p4 ph2):f1

(p6 ph1):f1

(p4 ph2):f1

(p1 ph1):f1

lo to 5 times l23

(p1 ph22):f1

```
(p1 ph23):f1
go=2 ph31
d2 wr #0 if #0 zd ip22
lo to 3 times 2
d2 rp22
30m iu23
lo to 4 times l1
HaltAcqu, 1m
exit
# 72 "/root/.topspin-BladeEpu/local_acqu/ppDirs/ROCSA_SC212"
ph1=0
ph2=2
ph10=0 0 0 0 2 2 2 2
ph22={0}*8;{2}*8
ph23=0 1 2 3
ph31=0 1 2 3 2 3 0 1 ;2 3 0 1 0 1 2 3
```

Appendix 6 – Calculated vs experimental table.

<i>naloxone</i>	<i>HCl dihydrate</i>		<i>Freebase monohydrate</i>		<i>Freebase anhydrous</i>	
	<i>Experimental</i> <i>ppm</i>	<i>Calculated</i> <i>ppm</i>	<i>Experimental</i> <i>ppm</i>	<i>Calculated</i> <i>ppm</i>	<i>Experimental</i> <i>ppm</i>	<i>Calculated</i> <i>ppm</i>
1	119.4	119.77	125.5	115.88	122.2	115.24
2	122.2	116.55	122.5	117.63	119.3	113.46
3	139	138.99	141.9	138.94	138.4	140.39
4	144.6	145.07	146.8	144.52	143.5	143.8
5	90.2	89.65	94.1	91.83	90.5	92.77
6	213.3	224.08	216.6	225.58	213	218.86
7	37	34.2	40.1	32.07	36.7	31.35
8	33.3	30.19	33.2	32.48	31.2	34.09
9	62.8	61.65	68.7	67.27	65.4	65.37
10	26	22.28	27.1	21.2	23.9	19.95
11	125.4	124.14	130	122.81	126.5	120.9
12	129.9	128.8	133.3	129.77	129.8	128.9
13	49.9	49.63	53.8	50.8	50.5	53.99
14	71.6	72.58	75.6	73.77	72.2	76.11
15	28.38	23.29	34.6	25.36	30.1	26.23
16	47.8	43.65	44.1	37.07	76.8	38.41
17	53.7	50.05	57.1	51.8	53.9	56.17
18	134.19	131.97	138.3	138.17	135.1	141.1
19	133.82	130.97	115.3	109.48	112	114.92

Comparison of the experimental data and the CASTEP calculated data of ^{13}C for the three naloxone forms. In this case calculated ppm is δ_{iso} from the equation 2.18.

Appendix 7 – BABA pulse program

```
# 1 "/root/.topspin-BladeEpu/local_acqu/ppDirs/nbaba.jg"
# 1 "<built-in>"
# 1 "<command-line>"
# 1 "/root/.topspin-BladeEpu/local_acqu/ppDirs/nbaba.jg"
;baba1 (TopSpin 2.0)

;2D SQ-DQ correlation experiment for 1 rotor period recoupling using BABA
;standard experiment for 1H DQ spectra
;M. Feike, D.E. Demco, R. Graf, J. Gottwald, S. Hafner, and H.W. Spiess JMR A 122, 214-221
(1996)
;written by JOS, 11/12/03 (modified from baba1 system file by Steven Brown 5-1-07)

;Avance II+ version
;parameters:
;d1 : recycle delay
;p11 : for 90 degree BABA pulses
;p1 : 90 degree pulse (in BABA sequence)
;cnst31 : rotation rate in Hz
;ns : n*16
;l5 : number of BABA cycles
;FnMode: States-TPPI or STATES
# 18 "/root/.topspin-BladeEpu/local_acqu/ppDirs/nbaba.jg"
;$COMMENT=SQ-DQ experiment with BABA for 1 rotor period
;$CLASS=Solids
;$DIM=2D
;$TYPE=direct excitation
```

```

; $SUBTYPE=homonuclear correlation

; $OWNER=griffin

define delay tau
"tau=0.5s/cnst31-p1*2"
"d0=1u"
"in0=1s/cnst31"
; cnst11 : to adjust t=0 for acquisition, if digmod = baseopt
"acqt0=1u*cnst11"

# 1 "mc_line 32 file /root/.topspin-BladeEpu/local_acqu/ppDirs/nbaba.jg exp. def. part of mc
cmd. before ze"
; dimension 2D; AQ_mode (F1) States
define delay MCWRK
define delay MCREST
define loopcounter ST1CNT
"ST1CNT = trunc(td1 / 2)"
"MCREST = 10m - 10m"
"MCWRK = 0.111111*10m"
# 32 "/root/.topspin-BladeEpu/local_acqu/ppDirs/nbaba.jg"
1 ze
# 1 "mc_line 32 file /root/.topspin-BladeEpu/local_acqu/ppDirs/nbaba.jg exp. def. of mc cmd.
after ze"
LBLAV, MCWRK
# 33 "/root/.topspin-BladeEpu/local_acqu/ppDirs/nbaba.jg"
# 1 "mc_line 33 file /root/.topspin-BladeEpu/local_acqu/ppDirs/nbaba.jg exp. start label for
mc cmd."
2 MCWRK * 4
LBLSTS1, MCWRK * 4
LBLF1, MCWRK
MCREST
# 34 "/root/.topspin-BladeEpu/local_acqu/ppDirs/nbaba.jg"

```

```

d1
3 (p1 pl1 ph1):f1
tau
(p1 ph10):f1
(p1 ph11):f1
tau
(p1 ph12):f1
lo to 3 times l5
# 43 "/root/.topspin-BladeEpu/local_acqu/ppDirs/nbaba.jg"
d0

4 (p1 ph2):f1
tau
(p1 ph20):f1
(p1 ph21):f1
tau
(p1 ph22):f1
lo to 4 times l5

(p1 ph3):f1

go=2 ph31
1m
# 1 "mc_line 58 file /root/.topspin-BladeEpu/local_acqu/ppDirs/nbaba.jg exp. mc cmd. in
line"
MCWRK wr #0 if #0 zd ip1 MCWRK ip10 MCWRK ip11 MCWRK ip12
lo to LBLSTS1 times 2
MCWRK rp1 MCWRK rp10 MCWRK rp11 MCWRK rp12 id0
lo to LBLF1 times ST1CNT
MCWRK rf #0

```

```
lo to LBLAV times tdav
# 59 "/root/.topspin-BladeEpu/local_acqu/ppDirs/nbaba.jg"
exit
# 61 "/root/.topspin-BladeEpu/local_acqu/ppDirs/nbaba.jg"
ph1=(8) 0 2 4 6
ph10=(8) 4 6 0 2
ph11=(8) 2 4 6 0
ph12=(8) 6 0 2 4
ph2=0
ph20=2
ph21=1
ph22=3
ph3=0 0 0 0 1 1 1 1 2 2 2 2 3 3 3 3
ph31=0 2 0 2 1 3 1 3 2 0 2 0 3 1 3 1
```


Appendix 8 – NOESY pulse program

```
# 1 "/root/.topspin-BladeEpu/local_acqu/ppDirs/fmp.HH_NOE"
# 1 "<built-in>"
# 1 "<command-line>"
# 1 "/root/.topspin-BladeEpu/local_acqu/ppDirs/fmp.HH_NOE"
;HH NOE experiment (TopSpin 2.3)

#####
;#                #
;# HN NOESY for solids          #
;#                #
#####
;
; $COMMENT= HH NOESY Transfer Experiment
; $CLASS=Solids
; $DIM=2D
; $TYPE= 1H detect Hetero
; $SUBTYPE=Dipolar Transfer
; $OWNER=guest
;

# 1 "/root/.topspin-BladeEpu/local_acqu/ppDirs/HCN_defs.incl" 1
;Define Frequencies, Rotor Timings, and other common variables
;Use with Carbon (X-channel) Detection
;by W.Trent Franks (TopSpin 2.3)
;    adapted from an example on Bax website
# 6 "/root/.topspin-BladeEpu/local_acqu/ppDirs/HCN_defs.incl"
; $COMMENT=Frequency and Timing definitions
; $CLASS=Solids INCL
; $TYPE=Definitions
```

```

;$SUBTYPE=Carbon Detect
;$OWNER=franks

# 16 "/root/.topspin-BladeEpu/local_acqu/ppDirs/HCN_defs.incl"
define delay TauR
  "TauR=1s/cnst31"
define delay TauRm2
  "TauRm2=1s/cnst31 - 2u"
define delay TauRm4
  "TauRm4=1s/cnst31 - 4u"
# 17 "/root/.topspin-BladeEpu/local_acqu/ppDirs/fmp.HH_NOE" 2

#####
;#          Define Mixing          #
;# NOESY is Default, add Selective 90 w/ option #
#####

"in0=inf1"          ;#####
# 28 "/root/.topspin-BladeEpu/local_acqu/ppDirs/fmp.HH_NOE"
      ;# Compound pulses #
"d0=in0/2-2u-p3*4/3.14159" ;# t1_init => 90,-180 #

      ;#          #
"in30=inf1"          ;#          #
define loopcounter go_t1 ;# No increment if 1D #
"go_t1=td1"          ;#####

define delay ONTIME      ;#####
define loopcounter T1evo ;# Power Deposition Calcs #
"T1evo=larger(td1,cnst30)" ;# Constant Duty Cycle #

```

```

"d30=T1evo*in30"      ;#####
# 41 "/root/.topspin-BladeEpu/local_acqu/ppDirs/fmp.HH_NOE"
      ;#####
;$EXTERN      ;# python insertion point #
      ;#####

# 1 "mc_line 45 file /root/.topspin-BladeEpu/local_acqu/ppDirs/fmp.HH_NOE exp. def. part
of mc cmd. before ze"

; dimension 2D; AQ_mode (F1) States

define delay MCWRK

define delay MCREST

define delay d0orig

"d0orig=d0"

define loopcounter t1loop

"t1loop=0"

define loopcounter ph1loop

"ph1loop=0"

define loopcounter F1CNT

"F1CNT = min( 2 , td1)"

define loopcounter ST1CNT

"ST1CNT = max( 1 , trunc(td1 / 2))"

"MCREST = d1 - 30m"

"MCWRK = 0.142857*30m"

# 45 "/root/.topspin-BladeEpu/local_acqu/ppDirs/fmp.HH_NOE"

Prepare, ze

# 1 "mc_line 45 file /root/.topspin-BladeEpu/local_acqu/ppDirs/fmp.HH_NOE exp. def. of mc
cmd. after ze"

LBLAV, MCWRK

    "d0=d0orig + t1loop * in0 "

    "phval0 = (ph1loop % 2) * 90"

    MCWRK ip0 + phval0

```

```

"phval1 = (ph1loop % 2) * 90"
MCWRK ip1 + phval1
# 46 "/root/.topspin-BladeEpu/local_acqu/ppDirs/fmp.HH_NOE"

"d30=d30/2"          ;#divide by 2 for mc macro#
# 49 "/root/.topspin-BladeEpu/local_acqu/ppDirs/fmp.HH_NOE"
"ONTIME=aq+d0+d30+p10+p8+l3* $\tau$ R" ;# DARR left out #

#####
;#      Protections: Pre-Check      #
#####

# 1 "/root/.topspin-BladeEpu/local_acqu/ppDirs/1H_ON_prot.incl" 1
;1H_ON_prot.incl

; Check the total RF on-time
; 50ms is maximum

;$COMMENT=Protection against long decoupling time
;$CLASS=Solids PROT
;$OWNER=nmr su
# 10 "/root/.topspin-BladeEpu/local_acqu/ppDirs/1H_ON_prot.incl"
if "ONTIME<250m" goto PassONTIME
1m
print "The total ON-time exceeds 250ms"
goto HaltAcqu
PassONTIME, 1m

# 56 "/root/.topspin-BladeEpu/local_acqu/ppDirs/fmp.HH_NOE" 2
;total RF deposition restriction

```

```

#####
;#      Start of Active Pulse Program      #
#####

# 1 "mc_line 62 file /root/.topspin-BladeEpu/local_acqu/ppDirs/fmp.HH_NOE exp. start label
for mc cmd."

Start, MCWRK * 3 do:f2 do:f3

LBLF1, MCWRK * 3

LBLST1, MCWRK

MCREST

# 63 "/root/.topspin-BladeEpu/local_acqu/ppDirs/fmp.HH_NOE"
# 64 "/root/.topspin-BladeEpu/local_acqu/ppDirs/fmp.HH_NOE"
#####
;#  PRESAT      #
#####

# 82 "/root/.topspin-BladeEpu/local_acqu/ppDirs/fmp.HH_NOE"
(p3 pl2 ph1):f1
3u

#####
;#  t1 evolution  #
#####

if "go_t1>1"
{
# 96 "/root/.topspin-BladeEpu/local_acqu/ppDirs/fmp.HH_NOE"
(center
(d0):f1

```

```
(p1 pl1 ph20 p2 ph21 p1 ph20):f2
(p21 pl21 ph20 p22 ph21 p21 ph20):f3
)
}
```

```
#####
```

```
## Homonuclear NOESY Mixing #
```

```
#####
```

```
# 108 "/root/.topspin-BladeEpu/local_acqu/ppDirs/fmp.HH_NOE"
```

```
3u
```

```
(p3 pl2 ph2):f1
```

```
2u
```

```
TauRm2
```

```
d8
```

```
# 117 "/root/.topspin-BladeEpu/local_acqu/ppDirs/fmp.HH_NOE"
```

```
TauRm2
```

```
2u
```

```
(p3 pl2 ph3):f1
```

```
#####
```

```
## Acquisition #
```

```
#####
```

```
0.5u pl3:f3 pl4:f2 ; GARP power on 15f3
```

```
1u cpd3:f3 cpd4:f2
```

```
# 129 "/root/.topspin-BladeEpu/local_acqu/ppDirs/fmp.HH_NOE"
```

```
gosc ph31
```

```
# 134 "/root/.topspin-BladeEpu/local_acqu/ppDirs/fmp.HH_NOE"
```

```
1m do:f3 do:f2
```

```
lo to Start times ns
```

```
# 1 "mc_line 138 file /root/.topspin-BladeEpu/local_acqu/ppDirs/fmp.HH_NOE exp. mc cmd.  
in line"
```

```
MCWRK wr #0 if #0 zd
```

```
"ph1loop+=1 * (1 - kronecker_delta(1 , td1) )"
```

```
"d0=d0orig + t1loop * in0 "
```

```
"phval0 = (ph1loop % 2) * 90"
```

```
MCWRK ip0 + phval0
```

```
"phval1 = (ph1loop % 2) * 90"
```

```
MCWRK ip1 + phval1
```

```
lo to LBLF1 times F1CNT
```

```
MCWRK
```

```
"t1loop+=1 * (1 - kronecker_delta(1 , td1) )"
```

```
"d0=d0orig + t1loop * in0 "
```

```
"phval0 = (ph1loop % 2) * 90"
```

```
MCWRK ip0 + phval0
```

```
"phval1 = (ph1loop % 2) * 90"
```

```
MCWRK ip1 + phval1
```

```
lo to LBLST1 times ST1CNT
```

```
MCWRK
```

```
"t1loop=0"
```

```
"ph1loop=0"
```

```
MCWRK rf #0
```

```

lo to LBLAV times tdav
# 140 "/root/.topspin-BladeEpu/local_acqu/ppDirs/fmp.HH_NOE"

HaltAcqu, 1m
exit
# 144 "/root/.topspin-BladeEpu/local_acqu/ppDirs/fmp.HH_NOE"
#####
;#      Phase Cycle (min=4, full=16)      #
#####

ph0= 2 2 0 0
ph1= 0 2
ph2= 0 0 2 2
ph3= {0}*4 {2}*4
ph4= 2

ph20= 0
ph21= 1
# 157 "/root/.topspin-BladeEpu/local_acqu/ppDirs/fmp.HH_NOE"
ph31= 0 2 2 0 2 0 0 2

;PARAMETERS:
;p1   : f2 90 (pl1)
;p2   : f2 180 (pl1)
;p3   : f1 90 (pl2)
;p8   : f2 Presat (-DCpre)
;p6   : f2 soft 90 (pl26)
;p10  : HC CP contact pl10 (f2) and sp0 (f1)
;sp0  : f1 CP pwr
;p11  : f2 HP pwr
;p12  : f1 HP pwr

```


;pl3 : f3 dec pwr
;pl4 : f2 dec pwr
;pl10 : f2 CP pwr
;pl12 : f1 dec pwr
;pl13 : f1 alt dec pwr (Spinlock and CW)
;pl16 : f1 DARR pwr (DARR = MAS freq; PDS =120)
;pl26 : f2 soft 90 pwr
;d1 : recycle delay
;d8 : PDS/DARR mix time
;pcpd2 : pulse length in decoupling sequence
;cpdprg2 : cw, tppm (at pl12), or lgs, cwlg. cwlg (LG-decoupling)
;spnam0 : use e.g. ramp.100 for variable amplitude CP
;spnam6 : f2 soft 90 purge pulse (e.g. eSNOB)
;cnst30 : expected td1 for use in constant Duty (-DCDC)
;cnst31 : MAS Rate
;FnMode : TPPI, States or States-TPPI
;zgoptns : (-D) PRE, PURGE, CPD, CDC